

Counting metamaterials Kwakernaak, L.J.

Citation

Kwakernaak, L. J. (2025, May 28). *Counting metamaterials*. Retrieved from https://hdl.handle.net/1887/4247265

Version: Publisher's Version

Licence agreement concerning inclusion of doctoral

License: thesis in the Institutional Repository of the University of

Leiden

Downloaded from: https://hdl.handle.net/1887/4247265

Note: To cite this publication please use the final published version (if applicable).

Counting Metamaterials

Proefschrift

ter verkrijging van de graad van doctor aan de Universiteit Leiden, op gezag van rector magnificus prof.dr.ir. H. Bijl, volgens besluit van het college voor promoties te verdedigen op woensdag 28 mei 2025 klokke 11:30 uur

door

Lennard Jurian Kwakernaak geboren te Gouda, Nederland in 1996

Promotor:

Prof.dr. M.L. van Hecke

Co-promotor

Dr. M. Serra Garcia (Amolf, Amsterdam)

Promotiecommissie:

Dr. P.T. Brun (Princeton University) Dr D.P. Holmes (Boston University) Prof.dr. D.J. Kraft Prof.dr.ir S.J. van der Molen Prof.dr.ir W. van Saarloos

The cover depicts a scene that is a parody of the famous work "The Persistence of Memory" by Salvador Dalí, featuring elements from this dissertation such as the beam counter and twistbuckler metamaterial.

Contents

1	Inti	roduction	5		
	1.1	Memory in Materials	7		
	1.2	Stability of memory	10		
	1.3	Mechanical Metamaterials - Designing Material properties	11		
	1.4	Materials as Computers	12		
	1.5	This Thesis	14		
2	Counting Beams 15				
	2.1	Unit cell and cyclic driving	16		
	2.2	Counting and controllable transients	18		
	2.3	Sequential Processing	21		
	2.4	Outlook	23		
3	Bui	mping Buckled Beams	25		
	3.1	Introduction	26		
	3.2	Phenomenology	27		
	3.3	Simplified models and theory	33		
	3.4	Conclusion and discussion	38		
4	Hysteresis in Slitted Beams 39				
	4.1	Introduction	40		
	4.2	Phenomenology	41		
	4.3	Methods	42		
	4.4	Experimental and Numerical Results	44		
	4.5	Slitted Bellini Truss	47		
	4.6	Conclusion and Outlook	52		
5	Twistbucklers 53				
	5.1	Introduction	53		
	5.2	Twistbucklers	54		
	5.3	Interacting Twistbucklers	61		
	5.4	Parity Machine	71		
	5.5	Rule 15 and the Hexcycle Machine	74		

CONTENTS

	5.6 Conclusion and Outlook	77	
\mathbf{A}	Counting Beams Details	7 9	
В	Bellini Truss	89	
\mathbf{C}	Twistbuckler Details	91	
Bibliography			
Summary		113	
Samenvatting		117	
Publications		121	
Ac	Acknowledgements		

Chapter 1

Introduction

Everywhere we look, we find traces of the past. Footprints in the sand, photographs of long ago, and kind letters we read to reminisce, all allow us to infer information from the past. Just as we are able to dig to uncover archeological remains of long gone civilizations, Nature itself keeps a record; tree rings track the years (Fig. 1.1a) and allow us to discern historical weather, and the deposited CO₂ content in layers of arctic ice (Fig. 1.1b) allow us to track the legacy of global warming[1].

But not all traces remain and or are readily recognised. Exactly what information is retained, and what is not, is difficult to define. Here we will focus on a type of trace that allows us to infer back exactly what information is stored. An everyday example of this is a clicky pen. As it came out of the packaging in one specific state, depending on whether the tip is out or in, we can figure out whether it has been depressed an *even* or *odd* number of times. Another example is a mechanical lap counter (Fig. 1.1c). A simple device with two levers, one of which is used to 'add' a lap, and the other to reset the device to zero. Both devices store a *memory* of the past. More akin to the layers in trees and ice, is the process of forming layers in atomic and molecular layer deposition ¹. These techniques allow for the deposition of an exact number of layers on a substrate by repeatedly applying two different processes, akin to the two processes of pressing and depressing the plunger on a clicky pen or lap counter. However for some cases where we might not necessarily expect to find such

 $^{^1}$ In typical layer deposition two reactants A and B are sequentially deposited on to a substrate. First molecules of type A are deposited on to the substrate, terminating in a surface. Then, a concentration of a compound we will refer to as B is deposited. This compound crucially only attaches to A molecules, forming a closed surface of B molecules, of a single molecule thickness. Next, in a second process, all B molecules are replaced by A molecules, which allows for a repetition of the cycle.

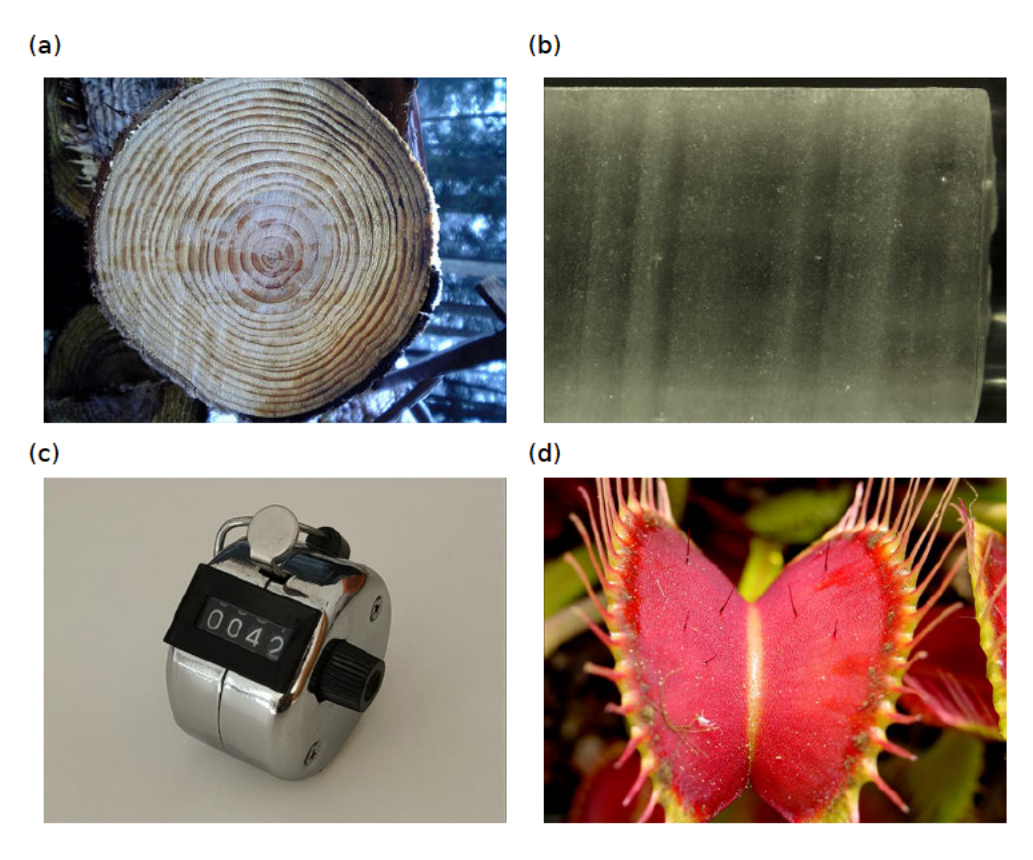


Figure 1.1: A number of objects showing memories of the past. (a) Tree rings which can be used to determine the age of a tree and to infer the growing conditions of the tree; a scientific field known as *Dendrochronology* (photograph taken by *aurorabreakup* on *panoramio.com*) (b) Layers of ice inside an ice core sample taken in Greenland as part of the GISP2 project. The visibility of the layers is caused by differently sized air bubbles formed through the deposit of differently sized snow during the winter and summer months. (c) A mechanical lap counter. (d) Photograph of the Venus Flytrap, showing the feeler hairs (photograph taken by *Noah Elhardt* and shared under a *Creative Commons Attribution-Share Alike 2.5 Generic* license)

an easily quantifiable memory. Famously, a cylindrical rod inserted in a container of granular matter is able to memorize in what direction the rod was previously rotated [2], and the plant known as the venus flytrap (Fig. 1.1d), despite not having a brain, is able to count[3].

1.1 Memory in Materials

Memories are naturally formed in a wide range of materials in response to variety of external driving protocols. Whether through mechanical deformation or externally applied magnetic fields, traces of the past remain and show up in a multitude of ways[4].

A classic example of memory in materials is found in systems of magnetic spins as modeled by the so-called Preisach model. In this model, the response of a material is modeled by "independent elementary hysteresis domains" [5, 6]. Each hysteresis domain has its two fields at which it flips, thus each state provides a single bit of information – which state it was flipped to last. When combined, these domains provide a more complex form of memory called "return-point memory" (RPM), characterised by the "tendency of a material to return to the same microstate upon cyclic driving" [7].

Contrary to its (unfortunate) name, RPM is not merely the ability for a material to recreate some feature when returning to some remembered driving(point). A linear (Hookean) spring does not have a form of memory, but would equally fit that description. In a purely linear system, there is no procedure to make a trace which can be recovered at a later time. In contrast, RPM is the memory of previous turning points in driving. When driven towards and past a turning point (a previous local extremum in driving), the measured output of the material will match the previous output at the turning point, after which the rate of change in the output jumps to a different value [8] (see figure 1.2). Once crossed, a turning point is removed. Turning points can thus only be added within the bounds of previous turning point, which puts a strict hierarchy on the remembered values encoded with the turning points².

Notably, RPM is observed in a vast number of systems, not only in idealised spin systems but in many complex systems as well after a break-in-period of an initial number of training cycles. In crumpled sheets for example, a system that features internal rearrangements and plasticity, the response of the foil develops as it is pushed and pulled between set bounds until it reaches a final response curve [9]. When driving

²Perhaps "hierarchical memory", or "pyramidal memory" (due to the requirement that new memories have to be within the bounds of the previous notches) would be a better fitting term.

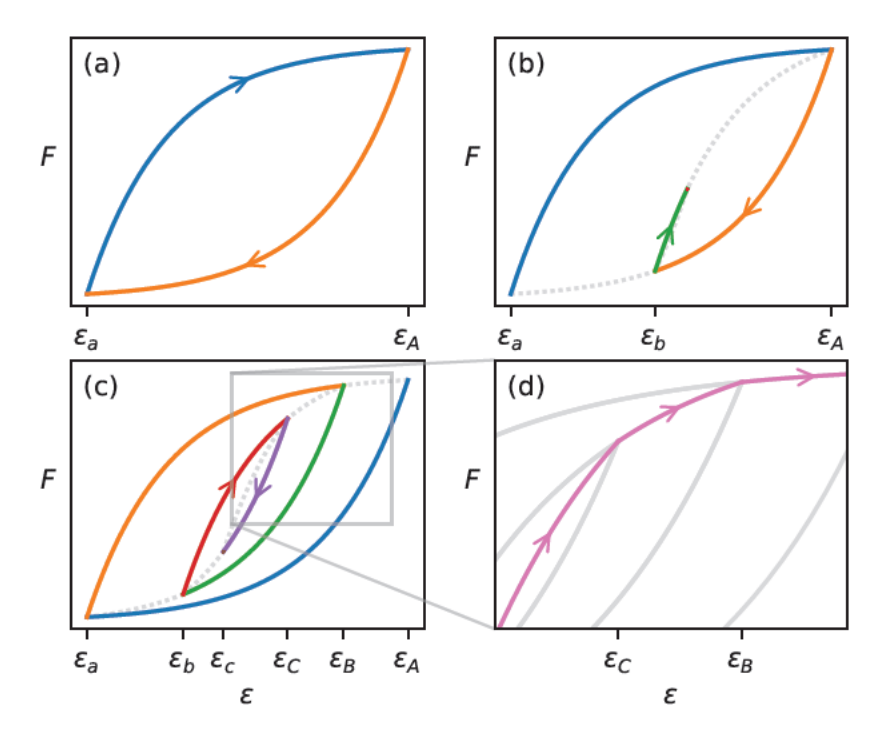


Figure 1.2: An illustration of the phenomenology of return point memory. Differently colored curves indicate continuous sections of monotonic driving. (a) In response to fixed-amplitude cyclic driving between ε_a and ε_A , the resulting force F forms a hysteresis curve as a function of ε . (b) When the driving direction changes, the response curve follows a trajectory that intersects the second to last turning point. (c) Information can be stored in the system by inputting turning points; by nesting hysteresis loops through changing driving direction at specific strains. (d) Information is extracted by moving past a turning point. As this point is crossed, the slope of the curve undergoes a measurable jump due to the trajectory shifting toward the next turning point. Driving past a turning point removes it.

the crumple, it continues to snap and pop, even when displaying RPM, demonstrating the non-linear nature of these mechanisms.

Some materials which display RPM, display a second form of memory during the training period[4, 9]. First discussed in the context of charge-density waves[10], these "multiple transient memories" encode an arbitrary number of values that correspond to input in arbitrary order, given a significant system size [11, 4]. In contrast to RPM however, this form of memory is fleeting, or transient, unless noise is introduced [11]. Specifically, after many driving cycles the memories of intermediate driving extrema fades, and only RPM, the memory of extremal driving, remains [11].

Such transient memories can be described by the park-bench model of memory introduced by S. Nagel[12]. This toy model model effectively captures the main features of transient memories, including its fleeting nature, by the results of a simple game. It works as follows: Imagine a number of benches in a line, between which a peculiar type of grass has grown which gets trimmed by a fixed amount every time a person walks over it. If this person walks to the first bench and back, only the first patch of grass is trimmed. If this person walks to the N'th bench and back, the grass of the first N benches is trimmed. Upon inspection of the grass, the length of each section can be used to infer how often each bench has been passed. Note that this does not allow us to infer in which order the person visited the benches. The park bench model allows us to store memories, as long as there is still grass left to be trimmed. As soon as the grass is completely removed, further trips do not leave a complete trace of memory.

Although of academic interest, this form of memory as it occurs in materials is difficult to make practical use of. The practical read-out protocols of such memories do not extract all stored information exactly and the writing and subsequent read out of signals seems to be limited to about three distinct memories [13]. Note that this is after multiple training cycles, and the protocol yields only the resulting information that specific memories occurred, not how often they occurred. This seems to indicate that these read-out cycles do not yield all information stored according to the (idealized) park-bench model. From the framework of the park-bench model, neither the original length of the grass, nor the finite trimming length of the grass can be inferred from these measurements. In practice, materials that allow for a direct measurement possibility of the entire trace as proposed by the park bench model are beneficial. In chapter 2, we will discuss a system with memory that can be made equivalent to the park-bench model, and beyond, by additionally recording the order of applied inputs. In this system, the internal memory can be directly read out by a visual inspection.

1.2 Stability of memory

One crucial feature of traces is that they remain stable over time. This time could be relatively short, as in charge density waves[10] and the Venus flytrap[3], or in very long, as in disordered systems[11] such as spin systems [6], granular matter[2, 13], and crumpled foils[9]. In all these cases, the configuration of these systems encodes the stored information.

In many mechanical systems, the emergent stable states stem from local buckling events. Consider holding a playing card between your index finger and thumb; when pressed gently the card remains flat, but with enough force, the card buckles and bends either left or right. Past the critical buckling point, bending allows the card to reach a lower potential energy compared to staying straight, thus any small perturbation will cause the card to deflect to the left or the right instead of remaining straight. Note that, in perfectly symmetric systems, the direction in which the card initially buckles — left or right — is essentially random. However, in practice, this direction is completely determined by the broken symmetries present in the boundaries and the card itself. In comparison, pulling on the card does not have this effect, it will merely stretch a possibly imperceptible amount before possibly tearing. The material of the card, whether it is made of paper, plastic or even metal, does in general not influence this behaviour but merely the force required to buckle the card: buckling is a geometric feature. Once buckled, the effective stiffness of the card in response to compression drops dramatically. In structures like columns and walls, similar buckling events are to be avoided as they correspond to catastrophic failures, but in the context of mechanical memory, buckling provides functionality – after buckling, the playing card is bistable. This can by demonstrated by using a second hand. By pushing on the arch that is formed by the card, we can snap the card back and forth between two stable configurations without changing our hold with the first hand.

In the case of crumpled sheets for example, Shohat et al. [9] demonstrated through 3d-scanning that the mechanical stability of the sheet could be decomposed into many localized bistable elements. These bistable elements emerge from the process of crumpling and subsequently flattening of the sheet which subsequently allows for the encoding of memories. Every crease and fold that occurs when crumpling influences the formation of new creases and folds, thus forming a complex structure of bistable elements with equally complex emergent coupling. Such complexity is not necessary however. As shown by Bense et al. [14], a pre-curved rubber corrugated sheet features similar bistable elements that emerge when compressed. When cyclically compressed, this system shares some of the phenomenology of disordered systems and is able to "count to two" [14]. Here the curvature of the sheet localizes the formation of the bistable elements. Due to small defects and depending on how the system is

driven, different functionalities emerge which indicates that despite the comparative simplicity of this system, the coupling and behaviour of this system in a response to driving is anything but. Thus localised multi-stability appears as a key feature for memory in mechanical systems.

1.3 Mechanical Metamaterials - Designing Material properties

Mechanical metamaterials are artificial materials that obtain their unique and exceptional mechanical properties due to their structure. Here 'meta' means 'beyond', and indicates that the properties go beyond that of ordinary materials, similar to how 'metaphysics' goes beyond the study of the real world. ³. Mechanical metamaterials are a class of materials inspired by the previously studied optical metamaterials that have unusual properties such as a negative index of refraction[16]. Mechanical metamaterials instead focus on novel properties when deformed or stressed[17, 18]. Some of the earliest mechanical metamaterials have negative poisson ratio's making them so-called *auxetics*, which widen when pulled and narrow when compressed[19, 20], contrary to most ordinary materials. When pulling on a rubber band for example, it becomes thinner in the middle. For small deformations, it has been shown that materials with arbitrary linear responses (that obey thermodynamics) can be formed with just elastic materials and specific structures [21]. These elastic structures often feature slender elements, which can exhibit large reversible deformations, allowing for the creation of complicated mechanisms. Within the context of this thesis, elastic slender structures are ideal for designed memory effects as well. Elastic materials such as rubber are a "clean slate" when it comes to memory: when released these materials deform back to their initial unconstrained configuration. Furthermore, slender structures are exactly the types of structures that buckle when compressed along their length. Thus the creation of a mechanical metamaterial with designed memory functionality is a natural continuation of the earlier buckling-driven developments of mechanical metamaterials.

Consequently, memory has recently garnered interest in the field of mechanical metamaterials through the inclusion of elements that are themselves multistable[22, 23]. While such multistability of elements is likely necessary for the emergence of memory, it is in and of itself not the defining feature that allows for memory properties. Crucially, how the elements are coupled together is paramount. Elements that are

³This is different from the popular meaning of 'meta' in words as metadata (data about data) or metahumor (humor about humor). This second meaning of meta was popularised by Douglas Hofstadter in the book *Gödel*, *Escher*, *Bach* [15].

'weakly coupled' allow for the existence of many independent local multistabilities, whereas a 'strong' coupling causes avalanches, transition waves and otherwise global emergent stable states[24, 25]. Only when the stable states of a metamaterial remain local, does the capacity for memory in a mechanical metamaterial grow with the number of multistable elements inside of the material.

Furthermore, the coupling between the multistabilities inside a material needs to effectively encode the driving enacted on the material. Achieving this through a rational design such coupling appears to be a non-trivial task, yet (as discussed before) readily occurs in many disordered systems and 'natural' materials. Separate from the ability to recall a single previous event, is the ability for a material to distinguish the numeracy of repeated inputs. This requires a notion of response that not only depends on a previous driving input, but on the previous inputs as well. In other words, it depends on the outside influence and on the current state of the material. In this thesis we will discuss a recurring pattern specific to such counting like pathways. Furthermore, by designing metamaterials that feature specific pathways, we make these features practical. As discussed in the context of "transient memories" and the park bench model (Sec. 1.1), only a known structure with a known response can be used to effectively count and record driving cycles. An emergent counting response in a natural material can merely be categorised by supervised measurements.

1.4 Materials as Computers

Multistable materials bear a striking resemblance to computers. As discussed, the specific microstate of a multistable material can be used to infer information from the past. Whereas in the framework of computing, the internal state of a system is equivalent to all possible histories that led to that state, as described by M. Minsky [26]. To bridge these two concepts of state, we need a notion of how the material can be manipulated, and how each stable state would transition in response to the allowed manipulations; a state transition graph. This leads us to study such multistable materials as though they are computers. Specifically, in the language of computation, as though they are finite state machines (FSMs).

In recent research, mechanical metamaterials have been explored as 'computational' systems, designed to perform mathematical operations. The focus of many of these computational metamaterials is on implementing basic Boolean logic operations to achieve universal combinatorial logic [27, 28, 29]. While such materials are inherently valuable for certain tasks, the types of computations this class of metamaterials can perform, is limited by their lack of a *preserved state*. Furthermore, to perform arbitrary computation such as which can be performed by a Turing machine, a FSM,

would further need to be coupled to an infinite reservoir of states $(tape)^4$.

We note in passing that RPM - which readily occurs in many materials - could be used as a source of such basins of stable states. In collaboration with P. Baconnier, we demonstrated the memory storage capability of RPM. We managed to store and read out six recognizable states in a NiTinol alloy wire (similar to the work of Perković et al.[8], and the readout technique found in Keim [4]). The limit to the amount of states such basins can store are mostly determined by the measurement equipment, as the model used to describe the memory therein [5, 31], suggests a near-limitless reservoir of memory in this system.

In this thesis we will focus primarily on the development of mechanical metamaterials that mimic a specific type of FSMs – cellular automata (CA), a variant of FSMs that best mimic the spatial cellular nature of many solids. We propose to build mechanical materials made out of 'cells', each a small simple FSM with a single state, that remains mechanically local, and which interacts with its neighbours in a clocked fashion.

⁴In fact, as demonstrated by M. Minsky [26], a machine consisting of a relatively small FSM and infinite basin with which the FMS interacts with through a read and write tape, is shown to be Turing complete. Moreover, as a result of Shannon [30], the finite state machine needs only a single bit of information (two states), connected to an infinite tape, to compute anything. In the words of Minsky: "the demonstration by Shannon (1956) that, allowed enough symbols, one can replace any Turing machine by a two-state machine, shows that the structure of the state diagram can be hidden in the details of operation and not clearly represented in the topology of the interstate connections." [26].

1.5 This Thesis

Chapter 2 explores the beam counter mechanical metamaterial. This is a mechanical metamaterial consisting of slender beams that buckle and bump to interact, yielding a cellular automata that is able to count compressive driving cycles. Further, we combine multiple of these counters together to realize a metamaterial with memory properties akin to "multiple transient memories". We further develop this metamaterial to realize an order dependent response and demonstrate a 'lock-and-key' metamaterial.

Chapter 3 delves into the bumping buckled beams. The cornerstone of the interaction occurring in the beam counter metamaterial. In this chapter we uncover the mechanism behind the apparent linear scaling of the critical distance in the bumping buckled beams.

Chapter 4 discusses the slitted beams. These are a crucial ingredient of the beam counter metamaterial. This chapter further explores the mechanics of slitted beams and reveals the origins of their hysteretic behaviour and the observed triple stability in response to compression.

Chapter 5 discusses the twistbuckler mechanical metamaterial. This is a successor to the beam counter metamaterial that offers novel functionality such as cyclic responses to driving cycles. Instead of utilizing beams, these mechanical metamaterials feature elements that twist as they buckle and interact through rigid contact. This interaction simplifies the interaction between elements as compared to the interaction between bumping buckled beams and offers to opportunity to elegantly couple bistable elements in two dimensions instead of one.

Chapter 2

Counting Beams

Materials with an irreversible response to cyclic driving exhibit an evolving internal state which, in principle, encodes information on the driving history. Here we realize irreversible metamaterials that count mechanical driving cycles and store the result into easily interpretable internal states. We extend these designs to aperiodic metamaterials which are sensitive to the order of different driving magnitudes, and realize 'lock and key' metamaterials that only reach a specific state for a given target driving sequence. Our strategy is robust, scalable and extendable, and opens new routes towards smart sensing, soft robotics and mechanical information processing.

This chapter is based on previously published work [32]

Counting a series of signals is an elementary process that can be materialized in simple electronic or neural networks [33]. Even the Venus flytrap can count, as it only snaps shut when touched twice, despite not having a brain [3]. While the ability to count is not commonly associated with materials, certain complex materials, from crumpled sheets to amorphous media, can exhibit memory effects where the state depends on the driving history [34, 4]. Under cyclic driving, their response then may feature subharmonic behavior [35, 36, 37, 38, 39, 40, 41, 42] or, as was recently shown, a transient where the system only settles in a periodic response after $\tau > 0$ driving cycles [43, 14, 9]. The latter response thus counts the number of driving cycles in principle, but in practice, the link between this number and the internal state is highly convoluted. Materials that would feature controlled counting could simplify the design of soft robotics and intelligent sensors, and more widely, open a route towards sequential information processing. However, we have no rational strategies to control the link between state and count or to realize in-material counting.

Here we introduce a general platform for metamaterials [44] that count mechanical compression cycles. Our metamaterials consist of unit cells that each feature a memory-beam (m-beam) that is either buckled left or right, which we represent with a binary value $s_i = 0$ or 1 [45] (Fig. 2.1a). The unit cells are designed to interact with their neighbors such that under cyclic compression any unit cell in the '1' state copies this state to its right neighbor (Fig. 2.1b-c). This leads to a mechanically clocked wave where the '1' state advances rightward, one unit cell per compression cycle. Hence, the collective state, $S := \{s_1, s_2, \dots\}$, evolves like in a cellular automaton [46], with repeated cyclical compression yielding simple predictable pathways.

We combine such beam counters to realize metamaterials which exhibit more complex forms of sequential information processing than counting, including the detection of compression cycles of multiple amplitudes, as well as their sequential order. Together, these establish a general platform for realizing targeted multi-step pathways in metamaterials and open a route towards sequential information processing *in materia* [47, 27, 48].

2.1 Unit cell and cyclic driving

We aim to realize metamaterials where state '1' spreads to the right when the compressive strain ε is cycled between ε_m and ε_M (Fig. 2.1). We note that in contrast to recent metamaterials which exhibit sequential shape changes under monotonic driving [49, 50, 51, 52, 53], we require a sequential response under cyclic driving. This necessitates unit cells that memorize their previous state, interact with their neighbors, and break left-right symmetry. We satisfy these requirements with unit cells i containing

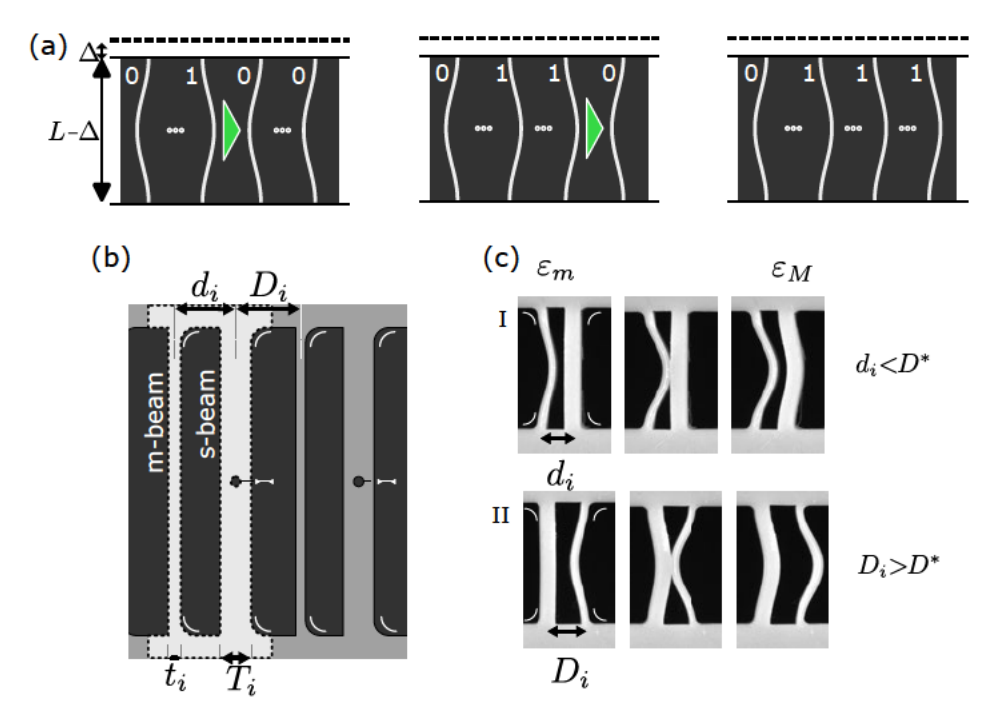


Figure 2.1: (a) Schematic representation of the evolution of a 'beam counter' metamaterial with n=4 unit cells under two compression cycles. Each unit cell contains a buckled m-beam (memory beam) which encodes a single bit. When the strain $\varepsilon := \Delta/L$ is cycled between ε_m and ε_M , the m-beams interact (grey symbols), so that the '1' state is copied to the right (triangle), leading to the step wise advancing of the '1' state to the right. (b) Geometry of a unit cell i (highlighted), containing a slender m-beam and a thicker, asymmetric s-beam (slitted beam) — lengths are non-dimensionalized by setting the beams rest-lengths to 1. (c) Evolution of beam pairs under increased compression from ε_m (left) to ε_M (right): when the spacing d_i is smaller than a critical distance D^* , the buckled state of the slender beam is copied to the slender beam (bottom).

two beams (Fig. 2.1b). The slender m-beams encode states $s_i = 0$ or 1 in their left or right buckled configurations. We choose ε_m larger than their buckling strain so they retain their state. The thicker and non-trivially shaped s-beams facilitate interactions between the m-beams, and buckle at a strain larger than ε_m but smaller than ε_M .

The detailed design involves a careful choice of the symmetry breaking beam shapes and their spacings. First, weakly symmetry breaking rounded corners at the ends of the m-beams controls their buckling into a desired initial configuration $S = \{100...\}$ — this does not appreciably modify the evolution of the sample during compression cycles, yet allows resetting the beam counter by momentarily cycling the strain towards zero. Second, the s-beams feature similarly rounded corners that makes them buckle left, and a slit which extends their reach when they snap to the right and the slit opens up (see chapter 4). As we show below, these symmetry breaking enhancements are crucial for their role in right-copying the '1'-state of the m-beams. Third, we use the beam spacings d and D to control the interactions between s- and m-beams. We found that when two buckled beams of unequal thickness are brought in contact, upon further compression they either both snap left or snap right — the direction depends on whether their distance is smaller or larger than a critical distance D^* . We choose $d_i < D^*$ and $D_i > D^*$ so that contact interactions between neighboring m- and s-beams favor rightward snapping of the beams (Fig. 2.1c).

2.2 Counting and controllable transients

We combine our unit cells to construct a 'beam counter' with n=11 unit cells, using standard 3D printing and molding techniques. We cycle the compression in a custom built setup that allows accurate parallel compression of wide samples, and track the center locations of the middle of the m-beams (Fig. 2.2b). Ramping up the strain from zero to ε_m , the system reaches the initial state {10000000000} (Fig. 2.2b). Repeated compression cycles show the step-by-step copying of the '1'state of the m-beams to the right, which involves rightward snapping of the appropriate m-beam just after ε has peaked (Fig. 2.2b). Hence, the state evolves as $\{100\dots 0\} \to \{110\dots 0\} \to \cdots \to \{111\dots 1\}$ (Fig. 2.2b). We characterize such 'domain wall' states consisting of a string of 1's followed by 0's by the number of 0's, σ . The evolution of our beam counter under cyclic compression can thus be seen as as counting down from $\sigma = 10$ to $\sigma = 0$. Our design is robust, can be scaled down, and can be operated in a hand-held device.

The evolution from the natural initial state {100...} only features a limited set of states, which do not contain substrings like 010 or 001. To demonstrate that our metamaterial correctly copies 1-bits to the right, we use manual manipulation to program the metamaterial in the initial state {01000111010} — this state contains

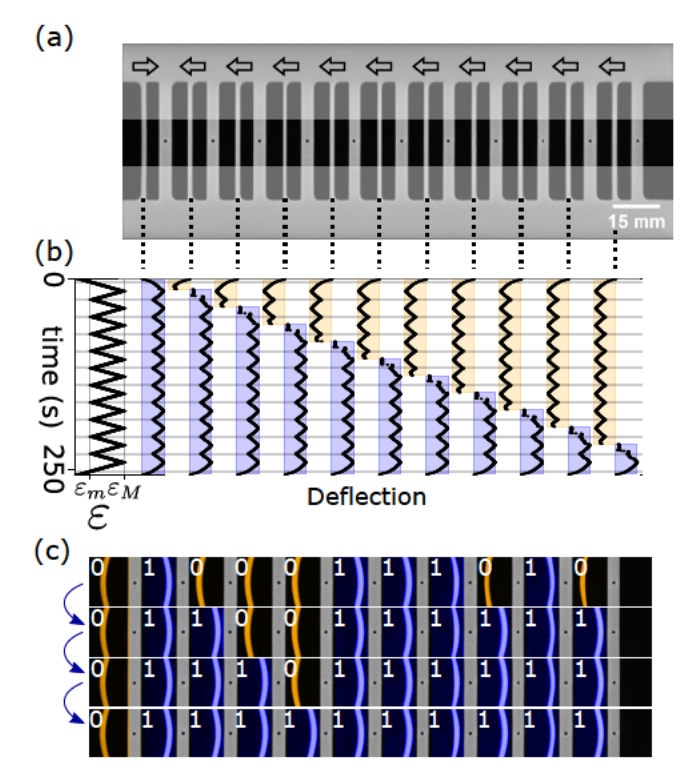


Figure 2.2: (a) Beam counting metamaterial with 11 units, with center region high-lighted ($t_i = 0.040$, $T_i = 0.10$, $d_i = 0.13$ and $D_i = 0.15$). Arrows indicate weak symmetry breaking of the m-beams that makes the system reach state {10000000000} when ε is increased from zero. (b) Space-time plot, tracing the center positions of each m-beam as a function of time under cyclic compression $\varepsilon_m \nearrow \varepsilon_M \searrow \varepsilon_m$ ($\varepsilon_m = 0.026$, $\varepsilon_M = 0.099$). Beams in state 0 (1) are highlighted in yellow (blue). (c) Evolution of the beam counter prepared in the initial state {01000111010} (central parts shown only; beam state colored as above).

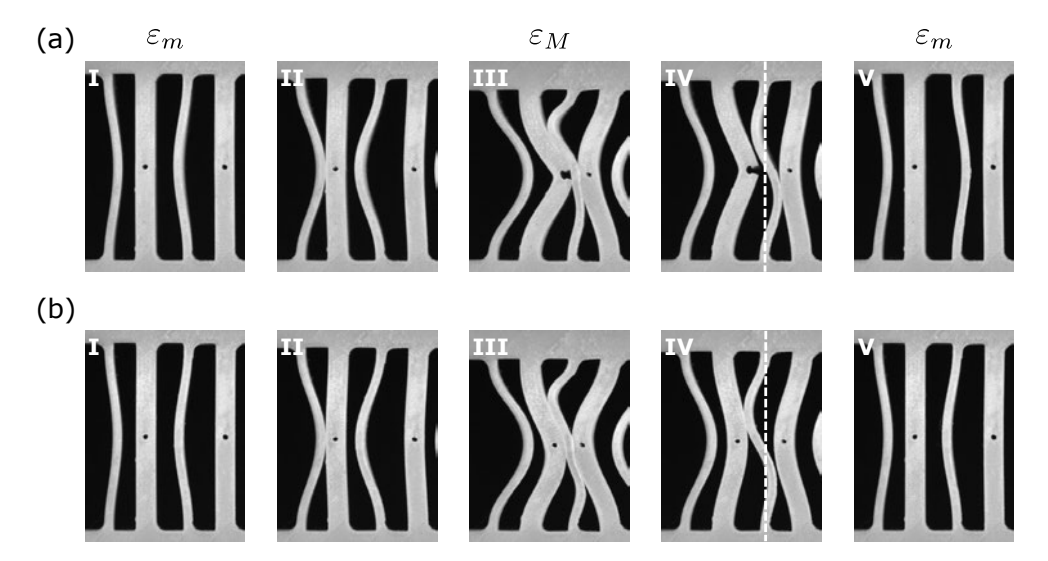


Figure 2.3: Comparison of the evolution of two unit cells during a compression cycle. (a) Original design. (b) Design without slits, which does not copy the '1' state. Frames (aIV) and (bIV) are not at the same strain, but compare the states where the second m-beam just loses contact with one of its neighboring s-beams; note that the m-beam is then, respectively, to the right (a) and left (b) of the neutral line (dashed).

all possible three-bit substrings. Its evolution shows that our metamaterial faithfully executes our target evolution (Fig. 2.2c). Moreover, we note that this initial state evolves to the absorbing state $\{11...\}$ after only $\tau = 3$ cycles, as the largest numbers of 0's to the right of a 1 is equal to three. Here, the transient τ is not a material property but a simple function of the state [43, 14].

A detailed inspection of the evolution of adjacent unit cells during their evolution illustrates that bit-evolution takes place in a two phases (Fig. 2.3). First, when ε is increased beyond a unit-cell dependent critical strain ε^{\dagger} , the '1' state of m_i is copied to s_i (Fig. 2.3aI-aIII). During this first phase, the left s-beam snaps open to the right, and the m-beam becomes sandwiched between two s-beams (Fig. 2.3aIII). In the second phase, ε is lowered to ε_m , and the sandwiched m-beam snaps right, after which all beams relax to their new configuration (Fig. 2.3aIII-aV). To illustrate how the slits facilitate the copying of the right-buckled state, we compare the sandwiched states for s-beams with and without slits (Fig. 2.3). Without slits, the sandwiched m-beam is pushed left and first loses contact with the right beam; with slits, the m-beam is pushed right, first loses contact with the left beam, and eventually moves right (Fig. 2.3a-b). We stress that although the slits are essential in the current design, we also realized beam counting in an alternative design that does not feature slitted beams.

2.3 Sequential Processing

To demonstrate process information beyond simple counting, we combine multiple beam counters into aggregate metamaterials (Fig. 2.4). Our first goal is to realize metamaterials which discriminate and count driving cycles of different peak compressions ε_M . Specifically, we combine three n=4 beam counters labeled aaa, bbb, and ccc which have respective critical thresholds $(\varepsilon_a^{\dagger}, \varepsilon_b^{\dagger}, \varepsilon_c^{\dagger}) \approx (0.073(4), 0.085(3), 0.092(2))$, which are all controlled by the same global strain ε (Fig. 2.4a-b). We label the resulting metamaterial as aaa|bbb|ccc, and characterize its state by the number of '0' beams in each counter, $\{\sigma_i\}$. We define driving cycles of different magnitude, A, B, C, as compression sweeps $\varepsilon_m \nearrow \varepsilon_M^{A,B,C} \searrow \varepsilon_m$, with $(\varepsilon_M^A, \varepsilon_M^B, \varepsilon_M^C) \approx (0.078, 0.089, 0.099)$, such that $\varepsilon_a^{\dagger} < \varepsilon_M^A < \varepsilon_b^{\dagger} < \varepsilon_M^B < \varepsilon_c^{\dagger} < \varepsilon_M^C$. Starting out in the initial state $\{\sigma_i\} = \{3,3,3\}$, a single driving cycle (A, B or C) then advances one, two or all three counters, yielding three distinct states $\{2,3,3\}$, $\{2,2,3\}$, or $\{2,2,2\}$ respectively. Hence, from the state we can uniquely infer the applied driving cycle.

Crucially, longer driving sequences are also encoded in the internal state We denote sequential driving cycles as, e.g., BAC, for which $\{\sigma_i\}$ evolves as $\{3,3,3\} \xrightarrow{B} \{2,2,3\} \xrightarrow{A} \{1,2,3\} \xrightarrow{C} \{0,1,2\}$ (Fig. 2.4b). These states all encode specific information, e.g., state $\{1,2,3\}$ encodes one A and one B pulse, whereas $\{0,1,2\}$ encodes a memory of one B, one C and an arbitrary number of A pulses. We note that while the capacity of our metamaterial is limited by one or more counters reaching zero, it can be enlarged by increasing the length n of the counters. Furthermore, we note that our metamaterial precisely materializes the Park Bench model that has been introduced as a toy model to understand Multiple Transient Memories [54, 12]. Regardless, our strategy combining multiple beam counters allows to distinguish and count different signals.

So far, our metamaterials are insensitive to the order of input signals, which limits their functionality to counting. However, combining unit cells with different thresholds in a single 'strip' realizes heterogeneous metamaterials whose response is sequence dependent and, e.g., discriminates driving cycles ABC from BAC. We realize the heterogeneous metamaterial bac. (Fig. 2.4c-e). Starting from state $\sigma=3$, we can use the same logic as before to infer its evolution and we subsequently collect all possible pathways in a transition graph (Fig. 2.4c). In particular we find that input BAC yields $\sigma=0$ while all other three-character permutations of A, B and C yield $\sigma=1$ (Fig. 2.4d-e). This illustrates that the response of heterogenous counters is sequence dependent.

Finally, by combining heterogeneous and homogeneous counters we realize an aggregate metamaterial that unambiguously detect a specific input 'key' string and thus

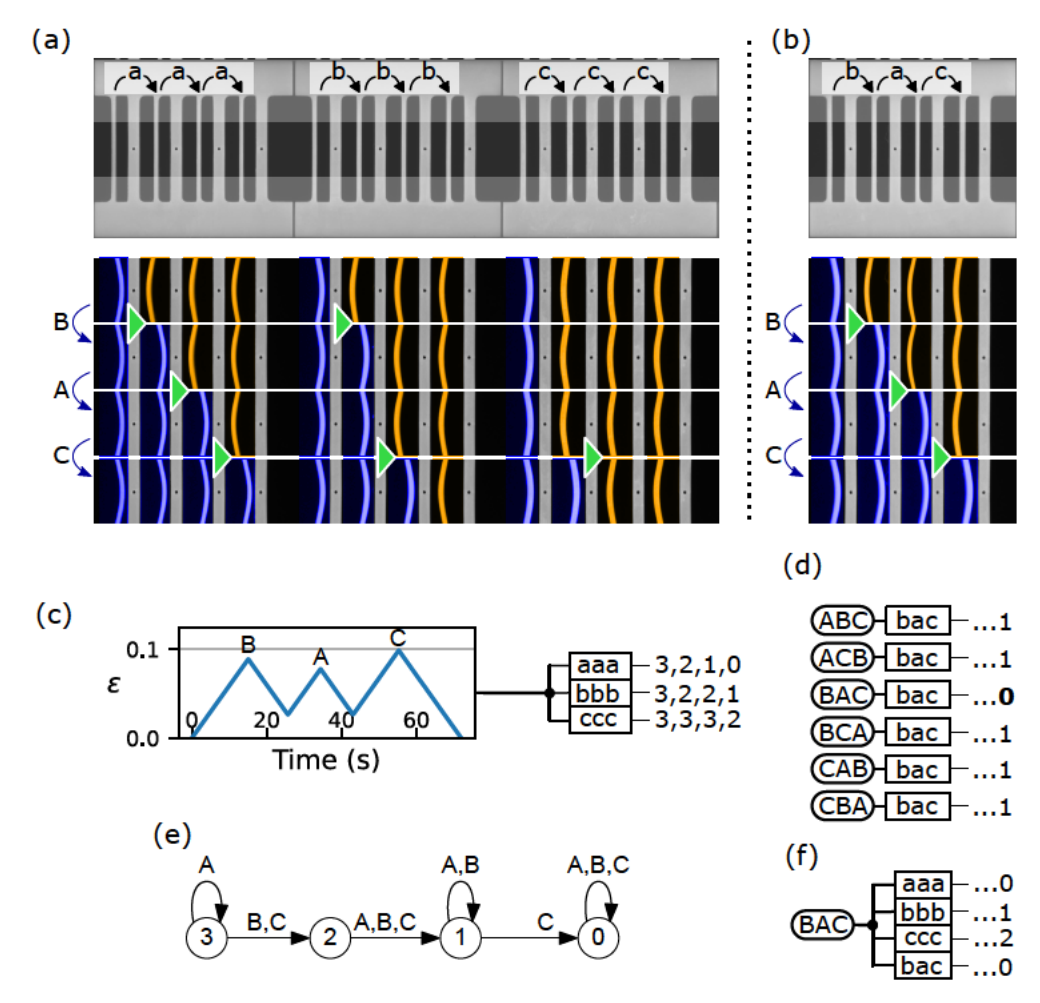


Figure 2.4: Response of aggregate metamaterials containing multiple homogeneous and heterogeneous beam counters. (a) Experimental realization of the aaa|bbb|ccc aggregate metamaterial, and snapshots of its pathway in response to input driving BAC (triangles highlight the right copying of a 1-bit). Note that t_i , d_i and D_i subtly vary along the counters while T_i remains constant (see appendix Sec A.1). (b) Experimental realization and evolution of bac counter during input string BAC (panel (b) and (d) are snapshots of the same experiment). (c) Complex driving cycles can be encoded as an input string (here BAC) and produce different sequential response in counters aaa, bbb and ccc (boxes represent individual counters and numbers represent the sequence of states σ_i). (d) The output of the bac counter to all input sequences which are permutations of ABC (rounded boxes). (e) Transition graph of the heterogeneous counter bac. (f) The four counters aaa, bbb, ccc and bac operated in parallel reach the unique state $\{0120\}$ only for input sequence BAC. The homogeneous counters store the count of each signal, while the heterogeneous counter is sensitive to the specific permutation.

act as a sequential 'lock'. We note that state $\sigma=0$ for counter bac is not unique to input BAC, but can also be reached with input sequences such as BBC and CCC (Fig. 2.4c). Hence, to uniquely recognize a string BAC, we combine the counting metamaterial aaa|bbb|ccc with the heterogeneous counter bac (Fig. 2.4b,d). Out of all three-character strings, BAC is the only one that yields the collective state $\{\sigma\} = \{0,1,2,0\}$ (Fig. 2.4f). The experimental demonstration of the response of he aaa|bbb|ccc|bac machine to input BAC is shown in Fig. 2.4b,d, which correspond to a single experimental run where all four counters were actuated in parallel. We note that our strategy can trivially be extended to longer sequences or larger alphabets.

While the design above cannot distinguish input BAC from longer sequences such as ABAC, we can detect such longer strings by extending the counter for the weakest signal: out of all possible input sequences, the metamaterial aaaa|bbb|ccc|bac only reaches state $\{0,1,2,0\}$ for input BAC, thus allowing to uniquely filter and detect such a string. Finally we note that designs featuring one heterogenous with multiple homogeneous counters are not optimal. Unique detection of, e.g., three symbol sequences with less than four counters can be achieved; in addition, many machines recognize multiple distinct input sequences (see appendix Sec A.4).

2.4 Outlook

Our platform allows to realize metamaterials with predictable counting-like pathways and easily readable internal states under cyclical driving. These metamaterials act as a sequential thresholding devices, and can be generalized to detect more driving magnitudes and longer sequences. Moreover, similar sequential behavior can be realized in other designs, e.g., without slits. In contrast to recent mechanical platforms that store mechanical bits [45] and perform Boolean logic [27, 48], our metamaterials perform sequential computations, which are much more powerful than combinational logic. Extending our update rules to more complex cases, including those where the new state depends on multiple neighbors, including in higher dimensions, opens routes to create systems that are Turing-complete, such as 'rule 110' or Conway's game of life [46, 55]. Such 'cellular automata materials' would allow massively parallel computations in materia.

Chapter 3

Bumping Buckled Beams

When a pair of parallel buckling beams of unequal width make lateral contact under increasing compression, eventually either the thin or the thick beam will snap, leading to collective motion of the beam pair. Using experiments and FEM simulations, we find that the distance D between the beams selects which beam snaps first, and that the critical distance D^* scales linear with the combined width of the two beams. To understand this behavior, we show that the collective motion of the beams is governed by a pitchfork bifurcation that occurs at strains just below snapping. Specifically, we use a model of two coupled Bellini trusses to find a closed form expression for the location of this pitchfork bifurcation that captures the linear scaling of D^* with beam width. Our work uncovers a novel elastic instability that combines buckling, snapping and contact nonlinearities. This instability underlies the packing of parallel confined beams, and can be leveraged in advanced metamaterials.

This chapter is based on previously published work [56]

3.1 Introduction

Elastic instabilities govern many of the exotic properties of mechanical metamaterials [24, 44, 57, 58, 59]. Typically, these metamaterials consist of slender elements that go through collective buckling or snapping instabilities, causing the material to switch between two states [59]. However, more advanced functionalities require a sequence of reconfigurations of the material, controlled by carefully designed instabilities and nonlinearities [60, 61, 59, 62]. The development of such materials thus requires an investigation into the complex instabilities mediated by interactions between multistable elements.

While constrained elastica have been thoroughly studied, comparatively less is known for systems of compressible beams in contact. First, constrained elastica have proven to be a rich platform of multi-stability with strong interactions between elements. Both elastica in a potential field [63], and elastica in contact with walls [64, 65, 66, 67] have been known to display multiple branches of stable solutions. Moreover, in systems with two elastica, the constraint between elements mediated by mutual contacts can be used as a source of interaction [68, 69]. Second, for compressible beams, additional complications arise as such beams buckle at finite strains [70]. In addition, for thick beams, the buckling transition changes from supercritical to subcritical [71, 57].

We recently introduced a beam counter metamaterial which evolves sequentially, and for which contacts between compressible beams of various widths are crucial (see chapter 2). Because contacts in such systems are highly nonlinear, their analysis is divided into subcases based on the quantity and types of contact between elements. As the number of elements in contact at any time remains small, such an approach allows for the analysis of larger systems of many elements.

Here, we investigate the symmetry-breaking of two unlike beams that buckle, make contact, and eventually snap. Crucially, we consider two beams with different thicknesses leading to an asymmetry in the system; the beams buckle at different strains, and have different rigidities. As the beam pairs are compressed, they traverse a sequence of reconfigurations. After buckling, the beams come into contact and interact through a reciprocal constraint. The resulting system is initially stable, but at some critical compression loses stability, causing one of the beams to snap through. Depending on whether the distance D between the beams is smaller or larger than a characteristic distance D^* , either beam can be selected to snap. To study the emergence of this characteristic distance, we perform both experiments and numerical simulations for a range of beam thicknesses and distances. Moreover, we derive an analytical framework that yields a closed-form solution for the scaling of D^* that

occurs in the experimental and numerical results. Our work captures the behavior of a pair of bumping buckled beams, and can be extended to a wide variety of scenarios where two unlike bistable elements are strongly coupled.

3.2 Phenomenology

We start by discussing the qualitative nature of the evolution of two buckling beams that come in contact under increased compression (Fig. 3.1a,b). The beams have rectangular cross sections and equal lengths L; we non-dimensionalize all length scales with the beam length and thus set L=1. They are compressed by a distance Δ , leading to a strain $\varepsilon = \Delta/L$. Their out-of-plane non-dimensional thicknesses d are assumed to be large and equal, so that the buckling strains are governed by the inplane dimensionless thicknesses t and T, where t < T; for definiteness, we assume that the thin beam is to the left of the thick beam (Fig. 3.1c).

In Fig. 3.1a,b we show the beam's evolution under quasistatic increase of the strain ε . The thin beam buckles at ε_t after which the thicker beam buckles at ε_T . We assume that the beams buckle towards each other (Fig. 3.1aII,bII). The distance between the centrelines of the beams, D, plays a crucial role, and we assume that D is small enough so that the two beams eventually get into contact at some strain $\varepsilon_c > \varepsilon_t$ — for now we will assume that $\varepsilon_c > \varepsilon_T$ also. When the strain is increased further, the contact forces between the beams increase, possibly leading to complex higher order mode. This configuration becomes unstable for a critical strain ε_c . Two distinct scenario's are then observed: either the thick beam snaps to the right (Fig. 3.1aIV) or the thin beam snaps to the left (Fig. 3.1bIV). As we will show below, the distance D selects which of these two scenario's occurs, and there is a critical distance D^* that separates these — for $D < D^*$, the thick beam snaps, whereas for $D > D^*$, the thin beam snaps. Hence, post-snapping there are two distinct states where both beams are buckled, either to the right (Fig. 3.1aIV) or to the left (Fig. 3.1bIV).

We note that in this example, the thick beam snapping for $D < D^*$ remains top-down symmetric (Fig.3.1a), while the thin beam snapping for $D > D^*$ develops an asymmetric shape (Fig. 3.1b). This is consistent with the condition for the development of asymmetric beam shapes for transversely loaded buckled beams: for a beam of thickness τ , such that asymmetric shapes develop when $\varepsilon \gtrsim 6.73\tau^2$ [72]. Hence, symmetric and asymmetric snapping is determined by comparing ε_s to $6.73t^2$ and $6.73T^2$ respectively (Fig. 3.2). Consistent with this, here we typically observe symmetric snapping when $D < D^*$ and asymmetric snapping when $D > D^*$, although deviations of this can occur for $T \approx t$. We note that the beam shape does not influence the left or right snapping of the beams, i.e., the value of D^* .

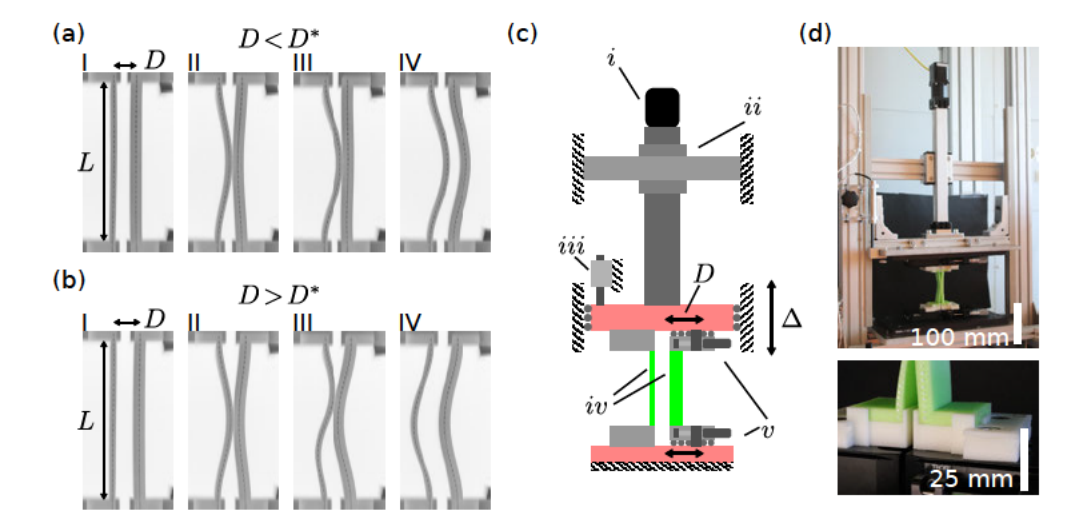


Figure 3.1: Phenomenology of two competing buckled beams. (a, b) Snapshots of beams separated by a distance of $D < D^*$ (a) and $D > D^*$ (b) as the compressive strain ε is increased: (I) beams at zero strain with D and L indicated, (II) initial contact at ε_c , (III) beam configuration just before the beams lose contact at ε^* , (IV) beam configuration just after the beams have lost contact through the snapping of the thick (a) or thin (b) beam. (c) Diagram of the setup showing: (i) stepper motor, (ii) linear actuator, (iii) inductive position sensor, (iv) samples, (v) micrometer stabes (d) Setup used to perform experiments. Top: Overview of the setup. Bottom: Zoom in showing the beam fixture attached to the linear stage.

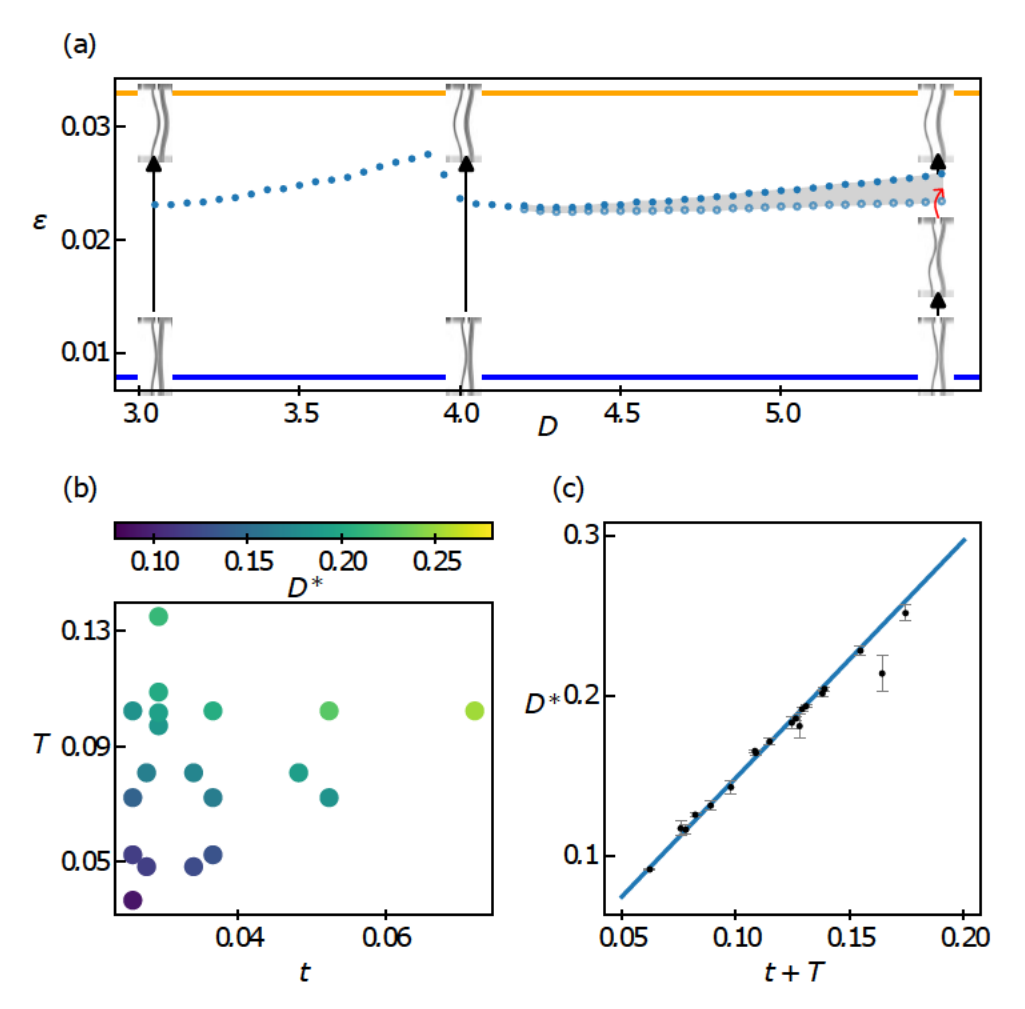


Figure 3.2: Experimental results. (a) Snapping strains of a two-beam pair with $t=0.026\pm0.0006$ and $T=0.072\pm0.0006$ (filled circles). Shown are results for multiple experiments where ε is increased at fixed D. Insets show pictures of different stable configurations of the system. Note that at large D there is an intermediary range where the thin beam becomes asymmetric before snapping. The region where the beams are stable in the asymmetric mode is indicated in gray. The horizontal lines correspond to $\varepsilon=6.73t^2$ and $\varepsilon=6.73T^2$ which are the thresholds for asymmetric snapping of the thin (blue) and thick (orange) beam respectively[72]. (b) Scatter plot of D^* for 19 combinations of t and t. (c) t0 plotted as a function of t1 shows a simple proportional relation with a slope t1.484 t2.006.

Intuitively, the emergence of the two distinct scenario's can be understood by considering the lateral stiffnesses of the two beams as ε increases. We define the lateral stiffness as the resistance of a beam to a vanishingly small point load applied at the middle of a beam perpendicular to the axis of compression. This lateral stiffness varies non-monotonically as the beam buckles: First the stiffness decreases down to zero at the buckling point, after which it increases again in the buckled configuration. By taking a small enough D, ε_c approaches ε_T , so that upon contact the thick beam is barely buckled and its lateral stiffness is near zero, whereas the thin beam is deeper in the post-buckling regime and significantly stiffer. Upon further compression, the thin beam induces a snapping of the thick beam. For even smaller D, ε_c becomes smaller than ε_T . Then, as the thick beam is not yet buckled when the beams make contact, the left-right symmetry of the thicker beam is broken, determining its buckling direction rightward. In contrast, for large enough D, when the beams come into contact when both beams are significantly curved, the thicknesses of the beams dominate their lateral stiffness, and the thick beam induces snapping of the thin beam. While intuitive, this picture does not produce a quantitative insight into what controls D^* , which is the focus of the remainder of this paper.

Experimental observations

To systematically explore the evolution of two post-buckled beams in contact, we designed and built a custom compression device which is stiff in all rotational and shear directions and ensures high parallelity between top and bottom plates (Fig. 3.1c,d). The compressive strain ε is applied through a linear stage, controlled by a stepper motor and monitored with an inductive probe, yielding repeatable positioning with an accuracy of 0.05 mm under typical loads. The distance D between adjacent beams is controlled by four Thorlabs XRN25 manual micrometer stages housing the fixtures which hold the beams in place with an accuracy of 0.01 mm. We track the deformation of the beams indicated by white protrusions on the front of the beams with a grayscale CMOS camera at a resolution of 3088x2064, reaching a pixel density at the objective plane higher than 10 pixels/mm.

We studied the evolution of pairs of beams of length $L=79.8~\mathrm{mm}\pm0.05~\mathrm{mm}$ and various thicknesses t and T. The samples studied are made out of VPS (Zhermack Elite Double 32, Young's modulus $E\approx 1~\mathrm{MPa}$, poisson ratio $\nu\approx0.5$) using molds made with FDM 3d printing on commercial UltiMaker S3 and S5 printers. After curing, the samples were allowed to rest for at least one week to allow the material properties to settle, after which the samples are demolded. Following this, the dimensions of the final samples were measured using an Instron universal measurement device equipped with 10N load cell and a touch probe to measure the thickness of

the relatively soft beams at various locations. The standard deviation in T along the surface of the samples is 0.1 mm. Experiments were only conducted with beams from the same batch of rubber.

To measure D^* , we performed multiple measurements for each beam pair at various D. At the start of each measurement, each beam is manually manipulated such that its buckled state is towards the adjacent beam. We then slowly increase ε at a rate of 4.2×10^{-4} s⁻¹ until the beams snap. For a typical beam pair with $t = 0.026 \pm$ 0.0006 and $T = 0.072 \pm 0.0006$ (the same pair as in Fig. 3.1a), as we incrementally increase D between measurements, we observe that the strain at which the beams snap, ε_s , varies smoothly up until $D \approx 0.153$, as can be seen in (Fig. 3.2a). Here ε_s sharply decreases as the system both transitions from displaying the below- D^* to above- D^* phenomenology, as well as shifting from a symmetric snap-through mode to an asymmetric snap-through mode. We note that the transition between left and right snapping, and the transition between symmetric and asymmetric beam shapes, are independent. The transition from symmetric to asymmetric beam shapes is determined solely by the values of ε/t^2 and ε/T^2 — for the example here, $6.73t^2$ $\varepsilon_s < 6.73T^2$ [72], so that the thick beam remains symmetric while the thin beam takes on an asymmetric shape (Fig. 3.2a). Finally, we observe that as D is increased above D^* , a small strain range opens up where the asymmetric beam shape is stable, before snapping at a larger strain (Fig. 3.2a).

Monotonously increasing D such as in Fig. 3.2 a, unintentionally trains the samples, such that the apparent value for D^* differs for increasing and decreasing sweeps of D. To minimize this hysteresis and accurately measure D^* , we performed iterative measurements with a specific protocol that reduces the number of subsequent measurements above and below D^* . We chose initial large steps of $D_{i+1} - D_i = 1$ mm to find bounds on D^* , and then refined the bounds with decreasing stepsizes: 0.5 mm, 0.25 mm, 0.1 mm and finally 0.05 mm. We then repeated every measurement set with exchanged left and right beams to correct for small asymmetries in the setup. We finally estimate D^* and calculate an error through the average and RMS of the four measured bounds.

Our experiments yield D^* for nineteen pairs of beams (Fig. 3.2b). We note that D^* grows with both t and T, and surprisingly, the data for D^* can be collapsed on a single axis by plotting it as a linear function: $D^* = \lambda^{exp}(t+T)$ (Fig. 3.2c), with a least squares fit slope of $\lambda^{exp} = 1.484 \pm 0.006$. We note that this data collapse does not significantly improve by adding an empirical fit parameter ℓ , i.e. plotting D^* as a function of $t + \ell T$. We discuss the validity and underlying physics that leads to this collapse in section 3.3.

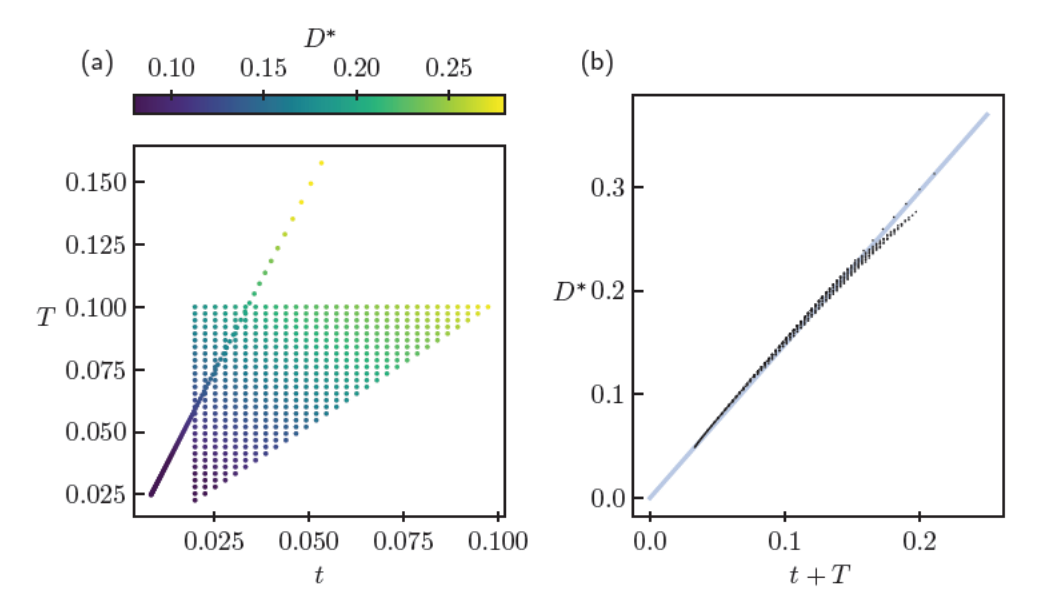


Figure 3.3: Finite element data for D^* as a function of t and T. (a) Raw data, showing the range of parameters of our two sets of simulations. (b) The data for D^* collapses as a function of t+T. The line corresponds to a linear fit of the data for $0 < t+T < \frac{1}{4}$, where $\lambda^{fem} = 1.478 \pm 0.002$. Note that the density of points is not uniform along the t+T axis.

Finite Element Simulations

To eliminate the role of plasticity and to test the validity of our observations for a wide variety of beam parameters, we performed FEM simulations of the co-buckling beams using ABAQUS with explicit time-stepping, CPS4 elements, Neo-Hookean material properties with a Poisson ratio of 0.49, uniform element sizes and sufficient damping to prevent oscillations. To ensure the beams buckle towards each other, a small temporary load is applied before the beams buckle and removed before the beams make contact. We performed two sets of simulations. In the first set we varied both t and T between 0.01 and 0.1, while in the second we varied the length of the beams at constant ratio $T/t \approx 2.95$. For every parameter t and T, we performed multiple simulations using a bisective approach to determine D^* , until the error in D^* was less than 10^{-4} . The results of these simulations are shown in (Fig. 3.3).

Similar to our experiments, we found both symmetric and asymmetric snapping. Consistent with our experimental observations, we find that D^* is essentially proportional to t+T for t+T<0.15. The fit of the numerical data yielded the slope: $\lambda^{fem}=1.478\pm0.002$, which is consistent with the results of the experimental data

where $\lambda^{exp} = 1.484 \pm 0.006$. We conclude that the critical distance D^* is linear in t + T.

3.3 Simplified models and theory

The phenomenology of the joint snapping of buckled beam pairs hints at the existence of a pitchfork bifurcation that occurs when the beams are in contact, i.e., before the beams snap through. Here we ask what the minimal ingredients are to observe such a pitchfork scenario. First, we investigate joint snapping for a slender beam model consisting of spherical beads connected with N bars that are modeled as linear and torsional springs, as proposed by Guerra et. al. [73]. We find that for large N, this simplified model captures the full phenomenology, including the existence of D^* and both symmetric and asymmetric snapping. For decreasing values of N, the model becomes more crude, but the existence and linear relation of D^* with t+T remains valid down to N=2. Such N=2 beams, which we call Bellini trusses [74], clearly cannot have asymmetric shapes, again indicating that asymmetry is not essential for the understanding of the scaling of D^* . Second, inspired by these empirical observations, we study the joint buckling and snapping of pairs of Bellini trusses in section 3.3. We show that their left or rightward snapping does not require the beams to lose contact, allowing us to focus on pairs of connected Bellini trusses. Finally, we show that the joint buckling and snapping is an example of a general scenario involving pairs of interacting elements that undergo pitchfork bifurcations at different values of the control parameter ε . We expand the Bellini truss system to analytically solve for D^* and find that it is linear in t+T (in lowest order). Together, this shows that joint snapping and the emergence of D^* is a robust and universal phenomena.

Elastic Bead-Chains in Contact

We model the contact dynamics of post-buckled beams with a simplified model of hard beads connected by Hookean and torsional springs. For a large number of links N, this model has been shown to accurately and computationally effectively model the dynamics of collections of buckled beams in contact [75, 73]. In addition, in the limit of small N (N=2), the model converges to an initially straight Bellini truss [74]. In the beam-chain model we space our nodes equidistantly along the beam length and choose the spring constants to match the stretching and bending energy of realistic beams [75]. We implement the contact dynamics between the beams with a stiff Hertzian contact model. The ends of the beams are controlled through the top and bottom particles, which control ε and D and which enforce the "fixed-fixed" boundary

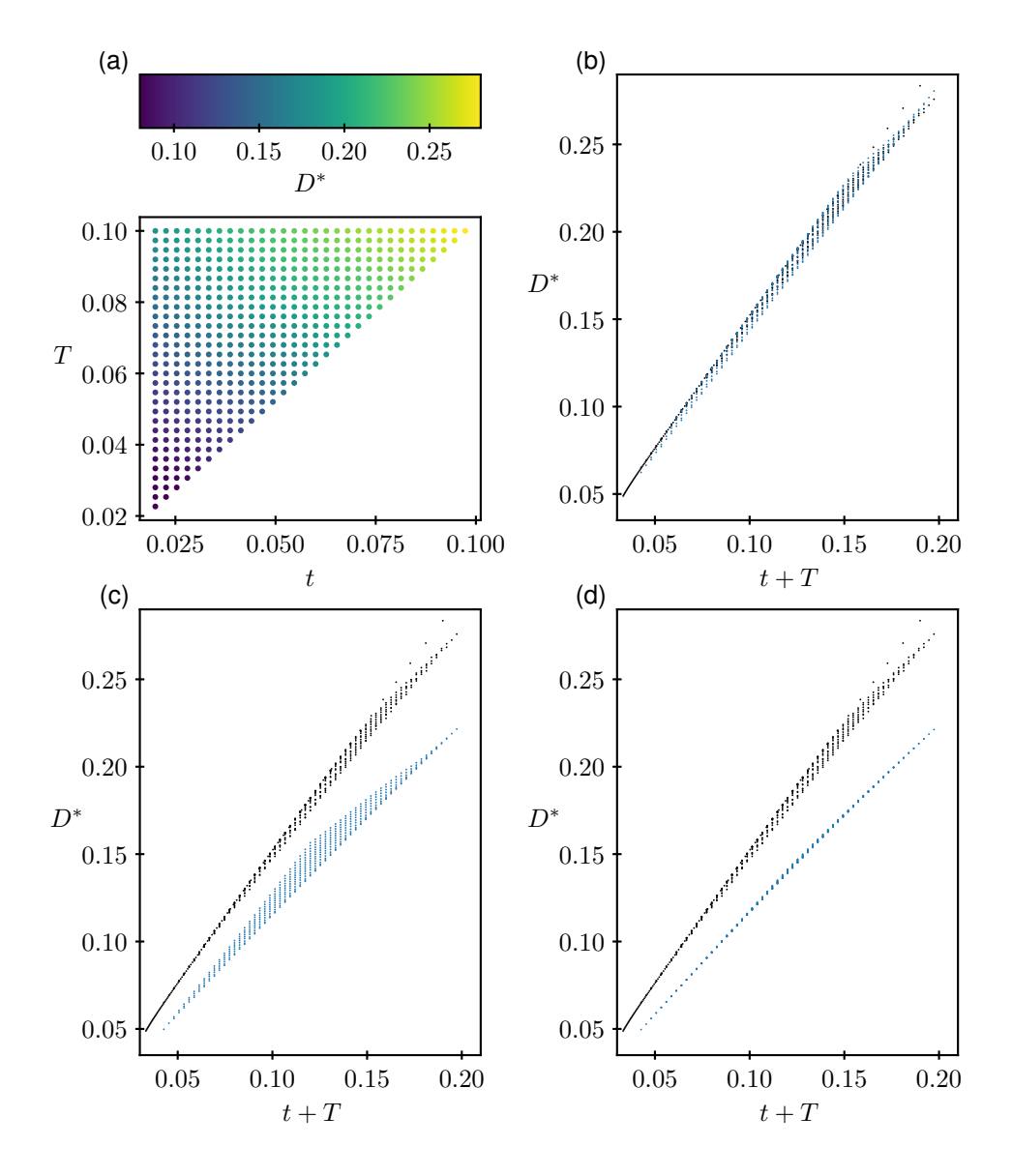


Figure 3.4: The critical distance D^* obtained in the elastic bead-chain model. (a) Scatter plot of the calculated D^* for N=62. (b-d) D^* collapses when plotted as a function of t+T. Data for the bead-chains and FEM simulations in blue and black respectively ((b) N=62; (c) N=4 and (d) N=2.).

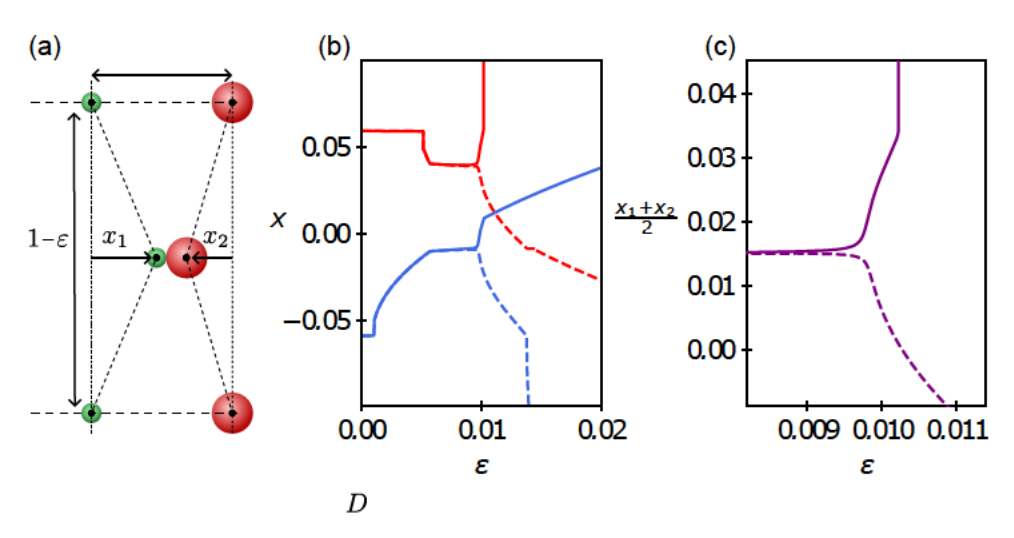


Figure 3.5: Pitchfork bifurcation for a pair of Bellini trusses. (a) The geometry for the N=2 system indicating the transverse displacements x_1 and x_2 for at a strain ε . (b) The horizontal positions x_1, x_2 (red and blue respectively) of the middle nodes of the two trusses for N=2 as function of strain ε , for two values of D just below (dotted) and just above (full) D^* ($t \approx 0.0031$, $T \approx 0.0071$, $|D-D^*| \approx 10^{-6}$). (c) The mean horizontal position $\langle x \rangle := (x_1 + x_2)/2$ near the pitchfork bifurcation point of these two cases track each other closely until they branch of at $\varepsilon \approx 0.0095$.

conditions of the beams (for details, see appendix B). We implemented the model beams using damped explicit time-stepping with the Large-scale Atomic/Molecular Massively Parallel Simulator (LAMMPS) [76, 73].

We performed simulations of pairs of beams for: $N=62,\ N=4$ and N=2, using the same bisective protocol to determine D^* (Fig. 3.4). For large N, where the model accurately captures continuous beam dynamics, the characteristic linear scaling $D^*=\lambda_{N=62}^{md}(t+T)$ emerges with $\lambda_{N=62}^{md}=1.472\pm0.002$, consistent with both the experimental and finite element simulation data (Fig. 3.4b). We note that these simulations also capture the symmetric and asymmetric beam shapes. Strikingly, for N=4 and N=2 (where the shape is purely symmetric) a comparable linear scaling of $D^*\propto t+T$ occurs ($\lambda_{N=4}^{md}=1.182\pm0.002$ and $\lambda_{N=2}^{md}=1.1542\pm0.0007$) (Fig. 3.4(c-d)).

For all three cases, we note that the beams first collectively move left or right, and then snap at a higher value of ε . This is illustrated in Fig. 3.5 for the simplified N=2 case, where we compare the evolution of the lateral motion of the center nodes as function of the strain for two values of D just above and below D^* . Our data strongly suggest that the $D=D^*$ case correspond to a pitchfork bifurcation, with

the evolution for $D \neq D^*$ given by unfolding of this pitchfork bifurcation. At larger strain, the discontinuous snapping transition occurs, but to determine D^* , it suffices to determine the location of the pitchfork bifurcation.

Instabilities in a pair of Bellini trusses

To understand the mechanisms that govern the critical distance and its scaling with t+T, we analytically determine the critical values (D^*, ε^*) of the pitchfork bifurcation in the model based on a pair of initially straight Bellini trusses. First, we connect their center nodes to model the persistent contact near the bifurcation, and separate the end nodes to capture D and ε (See Fig. 3.5a). Specifically, we place the end points of the thin and thick beams at $x = \alpha$ and $x = \beta$, and require that

$$D = \beta - \alpha + \frac{t}{2} + \frac{T}{2},\tag{3.1}$$

where we account for the thickness of the beams.

Second, we expand the elastic energy of both Bellini trusses up to quartic order in x and linear order in ε , and and find at leading order (see appendix B):

$$U_t = (\xi t^2 - \varepsilon)tx^2 + tx^4, \tag{3.2}$$

where ξt^2 is the buckling strain with $\xi = \frac{4B}{K}$. Hence, the buckling strain scales as the ratio of the constants B and K which parametrizes the compressive stiffness Kt and bending stiffness Bt^3 in the truss. Here, ξ can be considered the inhibition to buckling due to the applied boundary conditions and degrees of freedom of the beam model (see appendix B).

Satisfying Eq. 3.1, we obtain the total potential energy:

$$U = t \left[(\xi t^2 - \varepsilon)(x - \alpha)^2 + (x - \alpha)^4 \right] + T \left[(\xi T^2 - \varepsilon)(x - \beta)^2 + (x - \beta)^4 \right]. \tag{3.3}$$

We now obtain a closed form expression for (D^*, ε^*) by locating the pitchfork bifurcation in this quartic energy expansion. We first, without loss of generality, choose $\alpha t + \beta T = 0 \to \alpha = -\beta \frac{T}{t}$ to eliminate the cubic terms in the expansion. Hence, $D = \beta(1 + \frac{T}{t}) + \frac{t}{2} + \frac{T}{2}$ and we then write the potential in the form:

$$U = U_0 + ax + bx^2 + cx^4. (3.4)$$

The stable and unstable equilibria of the system are found at the roots of $F = \frac{\partial}{\partial x}U$,

3

where:

$$F = a + 2bx + 4cx^3 \tag{3.5}$$

$$= c \cdot (q + px + x^3) , \qquad (3.6)$$

with:

$$q = q(\beta) = \frac{2T^3\beta^3 - 2T\beta^3t^2 - T^3\beta\xi t^2 + T\beta\xi t^4}{2Tt^2 + 2t^3},$$
(3.7)

$$p = p(\varepsilon, \beta) = \frac{6T^2\beta^2 + 6T\beta^2t - T\varepsilon t + T^3\xi t - \varepsilon t^2 + \xi t^4}{2Tt + 2t^2}.$$
 (3.8)

Crucially, we do not need to solve for the roots of F explicitly; to find the bifurcation point, we only need to detect a change in the number of roots. The multiplicity of the roots of F can be determined from the discriminant $\Delta\{F/c\} = 4p^3 + 27q^2$. We note that this strategy is generally applicable for polynomials of arbitrary degree, whereas finding the solutions to such polynomials is generally not possible. As ε increases, the system changes from monostability to bistability. For $D = D^*$, this happens through a pitchfork bifurcation at $\varepsilon = \varepsilon^*$. For $D \neq D^*$ this happens through a saddle node bifurcation. This change of stability corresponds to $\Delta\{F/c\}$ crossing 0, where the pitchfork bifurcation occurs for q = 0 and the saddle node bifurcation occurs otherwise; in the latter case, the location of the saddle node determines whether the beams move left or right. As p depends only on β and not ε (Eq. 3.8), we can solve for β^* :

$$\beta^* = t\sqrt{\frac{\xi}{2}},\tag{3.9}$$

which can be substituted into Eq. 3.1 to obtain D^* :

$$D^* = (t+T)\left(\sqrt{\frac{\xi}{2}} + \frac{1}{2}\right). \tag{3.10}$$

In addition, we obtain the critical strain by solving q = 0 at $\beta = \beta^*$ and obtain

$$\varepsilon^* = \xi(t+T)^2. \tag{3.11}$$

We thus find that D^* scales linearly with t+T, consistent with our experimental and numerical results. In addition, we find a testable relation between the slope λ and the strain at which the beams buckle, as both depend on ξ : $\lambda = \frac{1}{2} + \sqrt{\frac{\xi}{2}}$, while $\varepsilon_t = \xi t^2$. Thus we predict that the boundary conditions of the beams influence D^* , e.g. pinned-pinned beams will have a smaller D^* than fixed-fixed beams. Comparing the Bellini truss model to the N=2 simulations with $\xi = \frac{3}{4}$ (see appendix B), we find a predicted $\lambda = \frac{1}{2} + \frac{9}{16} = 1.0625$, which is comparable to the value obtained from

simulations: $\lambda_{N=2}^{md} = 1.1542 \pm 0.0007$.

3.4 Conclusion and discussion

We studied the collective snapping of two buckled beams in contact by means of experiment, numerics and theory. Using experiments and FEM simulations, we found a linear relation between the critical distance and the combined width of the two beams: $D^* = \lambda(t+T)$. We studied a simplified model consisting of N compressive rods connected by torsional springs [73]. We find that at large N, this model accurately captured the collective snapping and critical distance, while at small N = 2, the model allows to identify the essential mechanism that controls the eventual direction of snapping: a pitchfork bifurcation that occurs at critical strain ε^* and distance D^* . Furthermore, this model allows to obtain a closed form solution for ε^* and D^* which captures the linear relation between D^* and t + T.

Our approach can be extended to a wide variety of scenarios where two bistable elements are strongly coupled, e.g., where the collective state can be described by a single coordinate. These include Bellini trusses that are precurved, and more generally, any buckling elements. The essential physics is that when two systems that undergo symmetric or asymmetric pitchfork bifurcations are coupled, the collective behavior is governed by a new pitchfork bifurcation.

Acknowledgements

Gratitude is extended to Douglas Holmes for insightful discussions, Arman Guerra for his expertise with LAMMPS simulations, and Jeroen Mesman for constructing the experimental setup.

Chapter 4

Hysteresis in Slitted Beams

Buckling and snapping instabilities form the backbone of many mechanical metamaterials. Here we show that slitted beams show both buckling and hysteretic snapping under axial load, resulting in a post-buckling regime with triple stability. We envestigate the hystersis loop under compression as a function of geometric parameters using both experiments and simulations, and introduce a minimal model based on the Bellini truss that captures the multistable behaviour of the slit beam.

The results in this chapter are the product of the collaborative work of the author of this thesis and fellow PhD candidate Bernat Durà Faulí. The initial concept was developed and used by the author in the framework of the counting beams (Chap 2). After some initial experiments showing promising results, Durà Faulí took over the main experimental and numerical work. The setup was built by the author, and the mounting was enhanced by- and the indenter was implemented by Durà Faulí. The Slitted Bellini Truss model shared in Sec. 4.5 was developed in collaboration, and is the product of many fruitful discussions.

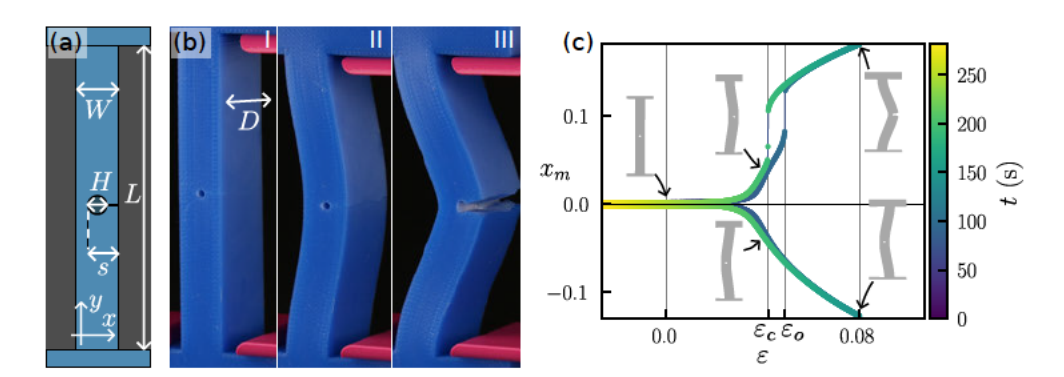


Figure 4.1: The slitted beam. (a) Geometry of a beam with a slit, characterized by its length L=80 mm, width W=10 mm, slit size S=6 mm and hole diameter H=1 mm. Beams have depth D=25 mm to prevent out of plane buckling. (b) Slitted beam configurations at various levels of compression. (c) The bifurcation diagram of a typical slitted beam $(t:=W/L=0.125,\ s:=S/W=0.6,\ H=1\,\mathrm{mm})$ as it is compressed. Shown is the mid beam displacement x_m as a function of the applied strain ε . The insets show the corresponding beam configurations. The beam is tristable in the range of strains $\varepsilon_c < \varepsilon < \varepsilon_o$, and can be either in the closed or open state. Note that, due to small visco-plastic effects, both branches display additional minor differences between the response under increasing and decreasing ε , which is most apparent near the buckling point.

4.1 Introduction

Elastic instabilities and geometrical non-linearities can often be harvested to produce exotic mechanical responses that lead to functionality. Such examples can be found in Nature, in the rapid closing of the Venus flytrap snap-trap [77, 78] and the jumping mechanism of various animals such as locust and grasshoppers [79, 80]. In all these examples, a slow build-up of elastic potential energy is followed by a rapid release and motion in the form of snapping. Recently, such instabilities have inspired soft robotics, where they allow for rapid actuation exceeding many-fold the speed of driving [81, 49], and mechanical metamaterials [59, 58, 61, 82, 24, 83] in which instabilities are used to harvest energy, change shape and process information.

One such metamaterial covered in chapter 2, features beams endowed with a slit. These beams are used in the framework of the "beam counter metamaterial" because of the observed large asymmetry of their configurations at large compression. While these structures exhibit useful mechanical behavior in the context of this metamaterial, the precise nature of the snapping instabilities and the origin of the hysteretic region warrant further investigations. In this chapter, we will demonstrate that these structures feature not only a tunable hysteretic response to axial compression but also

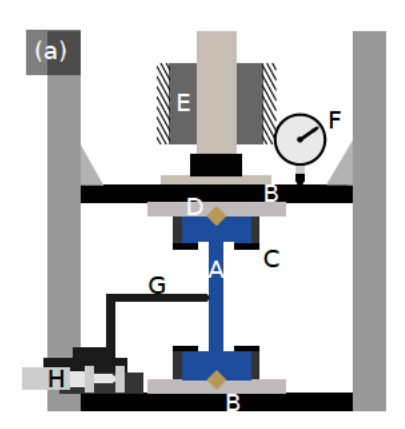
a region of triple stability – a rare phenomenon for such simple compressed structures.

4.2 Phenomenology

We start by discussing the qualitative features of the buckling and snapping of a slitted beam. We consider vertical rectangular beams (height L, width T, and depth D), enhanced with a single horizontal slit (length S) that is terminated with a small hole with a diameter of H=1 mm to prevent tearing (Fig. 4.1a). We fix the hole size at a diameter of 1 mm, which is large enough to prevent tearing, is readily manufacturable and is small enough to not influence the data significantly (as verified by numerics). For convenience, we will assume the slit is made on the right side of the beam, and we will further non-dimensionalize the dimensions of the beam by defining t=W/L and s=S/W. The beam is fixed at both ends under clamped-clamped boundary conditions and compressed uniaxially to a strain ε . The beam is made from a VPS rubber (discussed in Sec. 4.3), which in simulations is described as hyperelastic.

As we cycle the strain ε , we measure the mid-beam deflection x_m , via tracking of fiducial markers on the beams with a camera. The graph in Fig. 4.1c shows the evolution of the system as a function of strain. We distinguish four qualitatively different beam configurations: unbuckled, left-buckled, right-buckled and the opened slit configuration. Starting from the initial unbuckled configuration at $\varepsilon = 0$, as ε is increased the beam buckles, yielding either a left-buckled or right-buckled state. Note that these branches are mirror-symmetric in x_m (Fig. 4.1c), indicating that the slit has a negligible effect on the initial post-buckling mechanics, and that in both conditions the slit remains closed. Further compression results in an initial smooth evolution of the absolute mid-beam deflection $|x_m|$, until at a critical strain $\varepsilon = \varepsilon_o$ we observe a snap of the right-buckled configuration. This snap corresponds to a sharp increases in the mid-beam deflection and the opening of the slit. Note, that in the resulting open configuration, the mid-beam deflection is much greater than that of the left-buckled state at the same strain ε , which is precisely the functionality used in chapter 2. From this open state, as we subsequently lower the strain, we observe a snapping transition where the slit closes at ε_c (Fig. 4.1) ¹. As $\varepsilon_c < \varepsilon_o$, the slitted beam features a hysteretic response to driving. Moreover, in this hysteretic regime, we observe three stable states, both the left and right buckled states, as well as the open state. Thus here the slitted beam is tri-stable.

¹We do not observe transitions from the open to left-buckled state when the slit closes, although these might occur in cases with strong inertia.



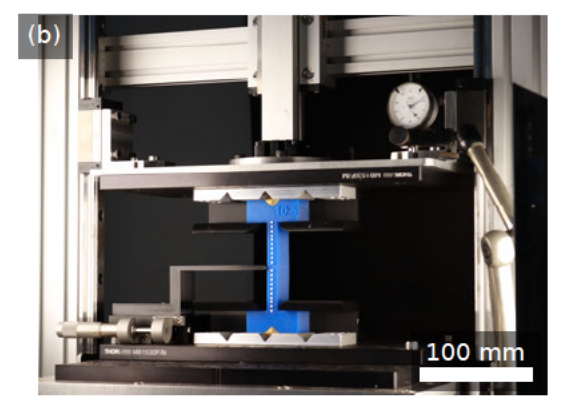


Figure 4.2: The experimental setup. (a) A diagram indicating all individual components. A beam (A) is clamped between two parallel plates (B) using 3D printed clamps (C). Rectangular brass bar (D) fit with a triangular dent on the beam's support and the metallic base to align both ends in the x-direction. A stepper motor (not featured) drives the position of the central bearing block (E), which controls the vertical position of the vertical top plate. A height gauge dial (F) is used to check for drift in the neutral position during and in between experiments. A 3D printed indenter (G) is mounted on a micrometer stage (H). (b) A photograph taken of the setup.

4.3 Methods

Here we discuss the experimental and numerical methods used to study slitted beam dynamics as a function of the geometry.

Experimental setup

To track the opening and closing of the beams as a function of ε , we perform experiments in a custom compression set-up consisting of two parallel horizontal plates with controllable relative vertical distance. The bottom plate is fixed, while the top plate is moved using a stepper motor with an accuracy of ± 0.01 mm to control ε with an accuracy of $\pm 1.3 \cdot 10^{-4}$. The plates are mounted on rails that ensure they remain parallel within 0.6 mm/m. Such a degree of parallelism is required not to prevent left-right symmetry breaking, and is significantly higher than the parallelism offered by commercial uniaxial test-setups². We calibrate the vertical distance between the

²Many commercial uniaxial testers are primarily intended to be measure an applied load in tension, by slowly extending samples until they fracture. These machines are built to not break or jam at fracture, but instead for the connections between the clamps and the load frames to loosen. In tension, this is usually favorable as well, as the loosening of these connections lead to universal joints

plates using a brass beam of a known calibrated length of 140 ± 0.03 mm. Furthermore, a dial indicator with an accuracy of ± 0.01 mm is used to check for drift in the position of the top plate between measurements.

The beam samples are cast in 3D printed molds using Smooth-On Mold Star[™]30 VPS rubber. A roughly incompressible rubber with a shore hardness of 30A and a Youngs Modulus of ≈ 0.7 MPa[84]. The beams feature small 2 mm protruding dots along their center line that are painted white to facilitate tracking. The deformation of the beam is recorded with a single channel CMOS camera at a resolution of 3088 × 2064, reaching a pixel density at the objective plane at 5 pixels/mm, and a framerate of 3 Hz. This set-up yields a tracking accuracy of ± 0.02 mm using a custom script based on OpenCV [85]. The beams are mounted with fixed-fixed boundary conditions to the plates with accurately aligned clamps (Fig. 4.2).

To repeatably enforce the buckling direction of the beams, we use an indenter. The indenter pushes the beam laterally at height L/2 by a manually adjusted amount mid-beam deflection x_{in} . To verify that the indenter has a negligible effect once the sample is buckled, we performed multiple experiments where we tracked the mid-beam displacement x, as a function of the indenter position x_{in} . As shown in figure Fig. 4.3, the indenter does not significantly influence the trajectory of the slit beam when not in contact. In practice we use x_{in} of 1 mm to determine the buckling direction.

Finally, we apply talc powder between the top and bottom parts of the slit of the beam, as well as between the indenter and the beam. This reduces the effect of stickiness which impedes the opening and closing of slit, and improves the reproducibility of the mounting of the sample.

Abaqus simulations

The experiments are influenced by material related viscous and plastic effects and and are sensitive to misalagnment of slender beams. To overcome these, we perform finite element (FEM) simulations on 2D slitted beams using the software package Abaqus/Explicit [86] in which we eliminate alignment problems, viscous and plastic effects, and speed up the exploration of the beam parameters. Abaqus/Explicit per-

and the elimination of applied bending due to misalignment in the setup. In tension, such loose connections are detrimental as they result in enhancing the misalignment, requiring the operator to continuously check the rigidity and alignment of the setup. Furthermore, the load cells used to measure the induced load are not conducive to a high degree of parallelism either. Often load cells are constructed as cantilever element that bending as they deflect, which skews parallelism. As a side effect, such load cells and are not insensitive to off-center loading either, i.e. an off-center sample or a sample that enacts a torsion on the load cell yields a skewed force reading. Thus, a measured load of a buckling beam would shift when the sample is moved off-center and would depend on the buckling direction of the beam with respect to the orientation of the load cell.

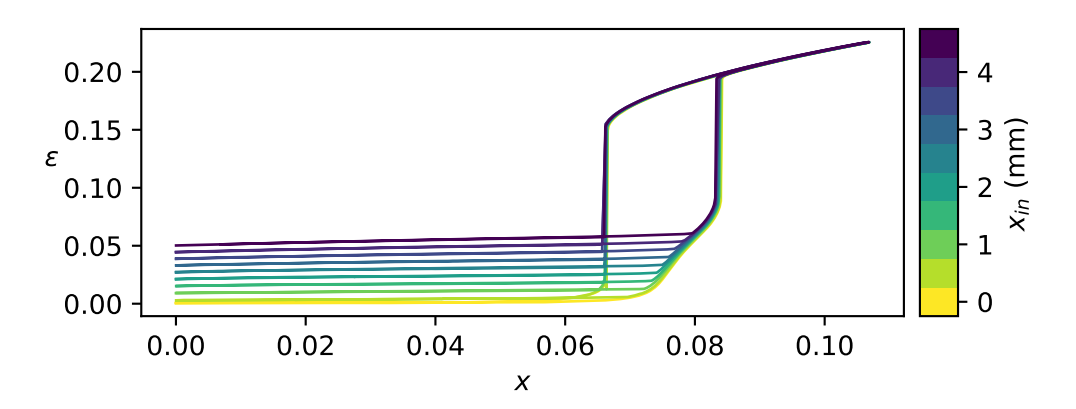


Figure 4.3: Effect of the indenter. Experimental response of a slitted beam (t = 0.150, s = 0.8) to consecutive driving cycles where the indenter position is increased by 0.5 mm after each cycle. The effect of the indenter on the relevant parts of the curves is negligible.

forms dynamic simulations to accurately handle non-linear behavior such as: buckling, snapping, and contact.

We model the 2D geometry of a slitted beam in the range of parameters s = [0.2, 0.8], t = [0.05, 0.175] using plain stress and fixed-fixed boundary conditions. We use CPS4 elements [86], a Neo-Hookean material with a Poisson ratio $\nu = 0.49$, a Young's modulus E = 0.78 (MPa) and sufficient damping to avoid oscillations. Furthermore, similar to the experiments, we use an indenter to control the buckling direction. However, instead of using a fixed indenter as in the experiments, in the simulations it slowly moves horizontally towards the beam while vertically moving down to remain at the virtual centre of the deformed beam as it is compressed. This eliminates tractional forces between the indenter and the beam structure, and does not require an initial relaxation period which would be required if the indenter were to intersect the structure at the start of a simulation. Post simulation, we find ε_o and ε_c by determining the strain at which the kinetic energy of the system is at a local maximum.

4.4 Experimental and Numerical Results

Here we discuss and compare the experimental and numerical results. To explore the dependence of the hysteresis on the geometry of the beams, we use beams of a constant length L=80 mm at various t and s.

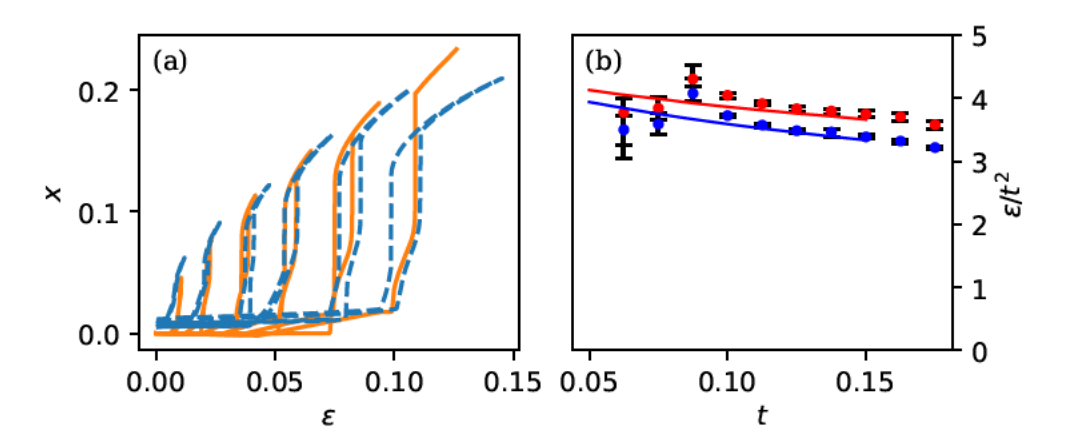


Figure 4.4: (a) The deformation as a function of ε for beams with t=[0.050,0.075,0.100,0.125,0.150,0.175] and s=0.6. As expected, beams with a larger thickness buckle at a later strain and have a larger hysteretic region. (b) Rescaled opening strain ε_o/t^2 (red) and closing strain ε_c^2 (blue) as a function of beam width for $s=0.6,\,H=1$ mm. Dots are experiments and lines are numerical data obtained by FEM simulations using Abaqus. The rescaled opening and closing strains show a nearly flat behavior. At small t, the opening and closing of the slit become difficult to experimentally discern from the initial buckling of the beam. This results in the increased errorbars.

t dependence

We measured and simulated the deformation of the beams at both increasing and decreasing ε for beams of various thicknesses and with a constant slit of s=0.6 (Fig. 4.4a). We find that, in good approximation, the opening and closing strains of slit beams scale as t^2 (note that the buckling strain of ordinary beams scales as t^2) (Fig. 4.4b). We note that in experiments, as $t \to 0$, the buckling transition becomes hard to distinguish from the snapping transition. This is likely related to the experimental errors accumulating for small beams, as well as that the hole terminating the slit remains of a constant size.

s dependence

To study the effect of the slit size on the opening and closing strains of the slitted beam, we performed simulations at various thicknesses t = [0.100, 0.125, 0.150], and with slits of sizes [0.60, 0.80, 0.90] (Fig. 4.5). We find that for all t the size of the hysteresis loop increases monotonically with s. Strikingly, the opening strain ε_o does

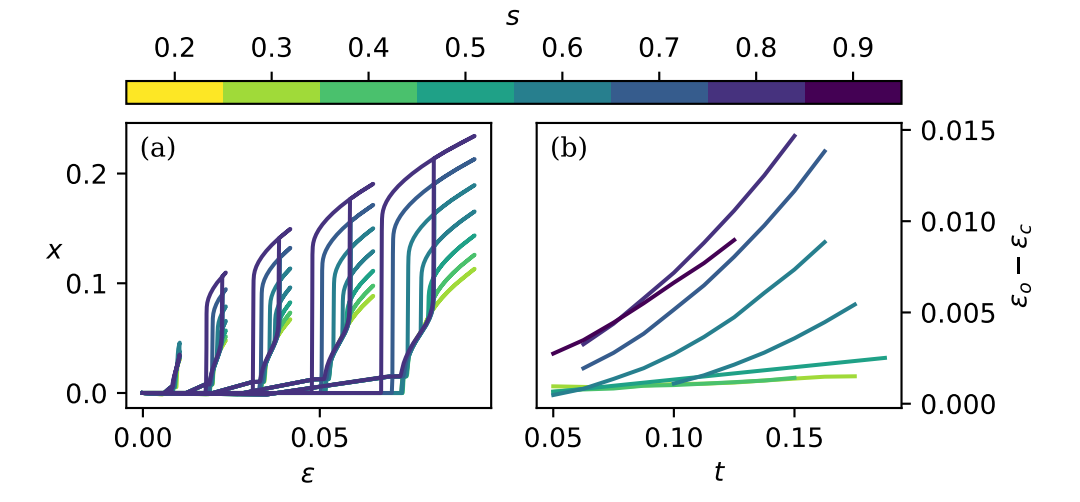


Figure 4.5: Effect of the slit size s on the observed hysteresis in simulations. Simulations for beams with with various thicknesses (left to right) t = (0.050, 0.075, 0.100, 0.125, 0.150), and slit sizes (at a constant hole size of H = 1 mm). (a) The measured deflection x as a function ε . (b) The measured hysteretic span $\varepsilon_o - \varepsilon_c$ for various t and s. Note that at larger slit sizes, the initial slope in x is not flat. This is due to the terminating hole making up a large part of the remaining midsection of the beam.

not vary strongly with slit size s, while the closing strain ε_c decreases as s is increased (Fig. 4.5b). Hence, the size of the slit widens the hysteresis loop by increasing the stability of the open state. For small slits (e.g., at s=0.3), the opening and closing of the slit becomes nearly Indiscernible. For large slits (e.g., s=0.8), the slit closes at a strain before buckling, leading to a direct snapping transition from the open state to a straight beam.

Discussion

Our simulations align well with our experimental results (Fig. 4.4). In particular, the simulations reproduce the mid-beam deflection magnitude as function of strain. Notable, the scaling of the snapping strains ε_o and ε_c with t are in close agreement between experiments and simulations, reinforcing the accuracy and validity of the simulations. We find that t increases both the buckling strain ε_b as well as ε_o and ε_c in proportion to t^2 . In contrast, the slit size s affects only the mid-point deflection in the open state and the corresponding closing strain ε_c .

4.5 Slitted Bellini Truss

Despite the accuracy of the Abaqus simulations in evaluating the effect of geometry on the opening and closing strains, they do not provide insight into the origins of these transitions. We thus introduce a simple spring-based model that captures the behavior of both the closed and open configurations separately. We show how these give rise to a perfect and an imperfect pitchfork bifurcation respectively, and show how the right combination of these two behaviors reveals the mechanisms of the opening and closing transitions.

The spring based model we will introduce here is based on two observations. First, when the slit is closed, a slitted beam behaves similar to an ordinary beam under fixed-fixed boundary conditions. Such a beam can be modeled by a Bellini-Truss [74]³ loaded along its ends. The Bellini truss is one of the simplest models of a structure that buckles at a *finite* strain. Second, once the slit is open, the top and bottom part of the beam each are still beams, yet under different boundary conditions.

Based on these observations, we introduce the slitted Bellini Truss model. We start from an ordinary Bellini truss of length 1, with spring constant k, internal angles α , and torsional spring constant κ_{α} (See Bellini Truss in appendix Sec B). We then

³the classical "von Mises truss" [70] stiffened by a torsional spring

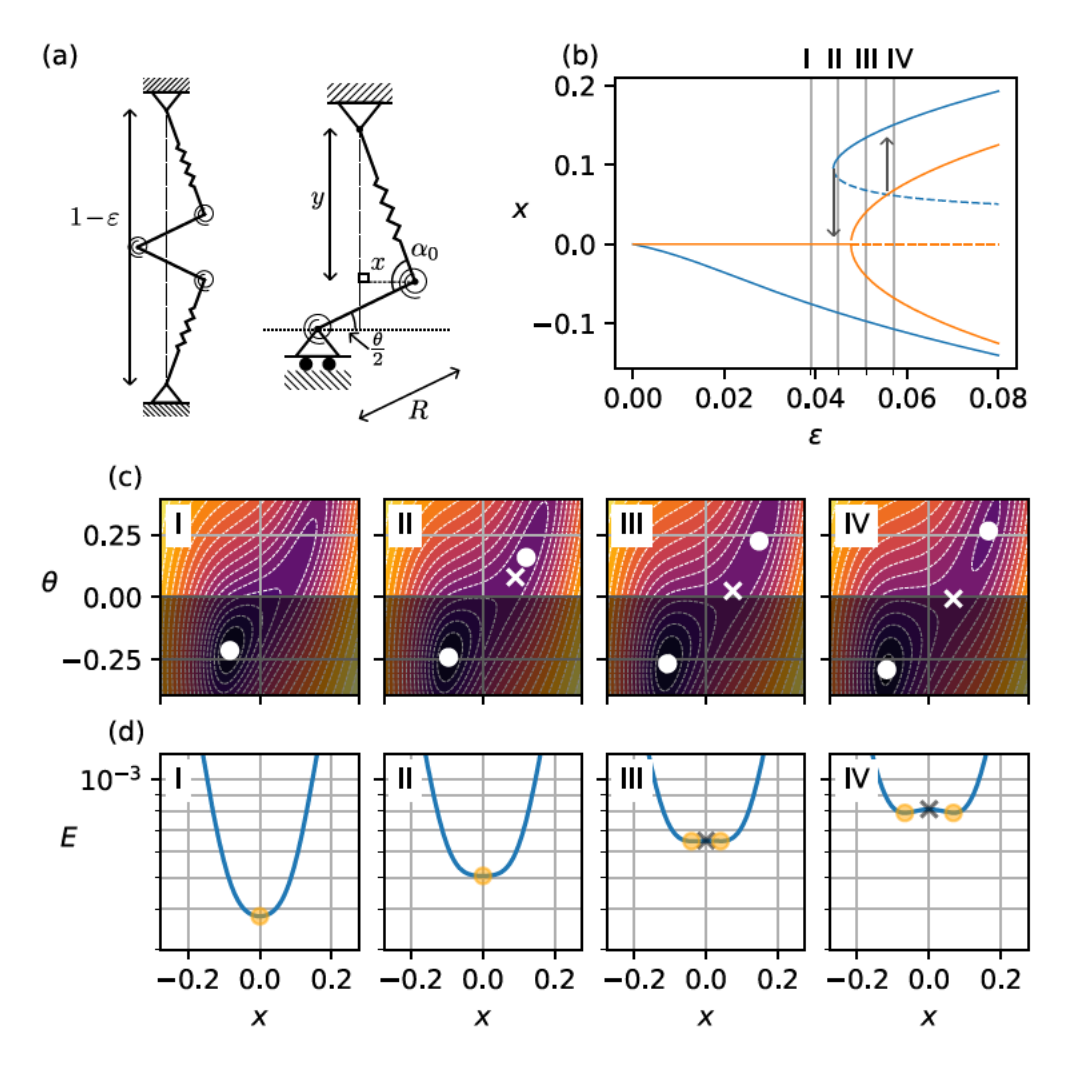


Figure 4.6: The slitted Bellini Truss model. (a) The Bellini truss modified with a hinge representing the slit (left). Due to symmetry, we can equivalently study the top half of the system with appropriate boundary conditions. (b) The two separate systems S_u and S_f allow us to find the stable points of the slitted Truss system S_0 , by solving the local extrema of E for free θ (blue), and for fixed θ (orange), as a function of ε . (c) The potential energy of the system as a function of θ and x for four values of $\varepsilon = [0.039, 0.045, 0.051, 0.057]$ (gridlines in b). The white dots represent local minima, and the crosses represent saddle points. The lower half $\theta < 0$ is shaded darker to represent regions of self-contact. The white contour lines correspond to lines of equipotential. (d) The potential energy of the system as a function of x at constant $\theta = 0$, and at aforementioned ε . The orange dots represent local minima, and the crosses represent maxima.

replace the center node of the Bellini truss with an off-center hinge which represents the slit. This hinge is composed of two rigid trusses of length R at an opening angle $\theta \geq 0$, joined with a torsional spring with stiffness κ_{θ} (Fig. 4.6a).

The truss is loaded in compression by moving the end-nodes such that their distance is at $1 - \varepsilon$. Due to top-down symmetry, we can (to simplify the computations) split the system in two equivalent sub systems, and consider a 'half beam' where the middle node is attached to a constraint that is free to move along the x-axis (Fig. 4.6a).

The potential energy of this system equals the sum of the potential energies of the springs. We choose the resting angles and lengths of all springs to form a desired initial "straight" configuration, and write the potential energy of the system as:

$$E = ku^2 + \kappa_\alpha \alpha^2 + \kappa_\theta \theta^2 , \qquad (4.1)$$

where

$$u = \frac{1}{2} - \sqrt{x^2 + y^2} \;, \tag{4.2}$$

$$y = \frac{1-\varepsilon}{2} - R\sin\frac{\theta}{2} , \qquad (4.3)$$

and

$$\alpha = \alpha_0 - \frac{\pi}{2} = \frac{\theta - \pi}{2} + \operatorname{atan2}(y, x) . \tag{4.4}$$

Thus, the energy of the system at each ε can be expressed as a function of x and θ (through substitution), with the geometric parameter R and energetic parameters k, κ_{α} , κ_{θ} . We can further reduce the number of free parameters by non-dimensionalizing the potential energy:

$$\hat{E} = u^2 + \hat{\kappa}_{\alpha} \alpha^2 + \hat{\kappa}_{\theta} \theta^2, \tag{4.5}$$

where $\hat{E} = E/k$, $\hat{\kappa}_{\theta} = \kappa_{\theta}/k$ and $\hat{\kappa}_{\alpha} = \kappa_{\alpha}/k$. This leaves the following three parameters of interest: R, $\hat{\kappa}_{\theta}$ and $\hat{\kappa}_{\alpha}$.

Determining the Slitted Bellini Pathway

The pathway of this system in response to driving can by found by tracing the local extrema of the potential as a function of ε . This requires to take into account the linear constraint imposed by the slit: $\theta \geq 0$. We solve the stability of the complete system: S_0 , by considering two related systems, the unconstrained system S_u where in which θ is free and thus the slit can open and even self-intersect, and the system S_f where $\theta = 0$ remains fixed on the boundary, and the slit remains closed. The stable states of the slitted beam are then determined by the stable nodes of S_u where $\theta > 0$,

and S_f where $\theta = 0$.

To solve the stable and unstable states of S_u , we calculate the potential energy E on a sufficiently dense grid in x and θ , and find the local minima and saddle points by intersecting the numerical contour curves ⁴ at $\partial E/\partial x$ and $\partial E/\partial \theta$ at each ε . For system S_f , we find the roots of the numerically determined $\partial E/\partial x$ at each ε . After linking together the solutions the critical points for a judicious choice of parameters ($\hat{\kappa}_{\alpha} \approx 0.0114$, $\hat{\kappa}_{\theta} \approx 0.0023$ and $R \approx 0.063$), we observe two separate bifurcation diagrams for S_u and S_f (Fig.4.6b). For system S_u , we observe a clearly asymmetric bifurcation diagram characterized by a saddle node bifurcation, whereas system S_f features a symmetric pitchfork bifurcation (Fig. 4.6b).

To find the trajectory of S_0 , we combine the stable branches of S_u where $\theta \geq 0$, with the stable branches of S_f where $\partial E/\partial \theta > 0$. Let us consider the same system (at parameters ($\hat{\kappa}_{\alpha} \approx 0.0114$, $\hat{\kappa}_{\theta} \approx 0.0023$ and $R \approx 0.063$)), at four illustrative strains $\varepsilon = [0.039, 0.045, 0.051, 0.057]$, as it is driven in ε . At each strain, we can visually infer the sign of $\partial E/\partial \theta$ by the contour lines and critical points E in Fig. 4.6c. Starting a low $\varepsilon = 0.039$, the stable state of the system is governed by S_f , as the stable state of S_u does not satisfy $\theta \geq 0$ (I). As ε is increased, a stable point and a saddle point of S_u emerge (II). While this results in an extra stability of the system it does not influence the sign of $\partial E/\partial \theta$. As ε is increased further, S_f symmetrically bifurcates to $(x,\theta)=(\pm\delta,0)$, corresponding to the buckling transition of the truss (III). If the system selects the x < 0 branch, the system remains stable for larger strains. However, when the system selects the x>0 branch, the system eventually snaps when $\partial E/\partial\theta$ crosses 0. As can be seen in figures Fig. 4.6cIII-IV, this corresponds to the strain where the saddle point of S_u crosses $\theta = 0$, at which point the system snaps to the "open" state given by S_f (IV). For further increases in ε , the system continues along the same stable branch. At decreasing ε , we follow a different trajectory. We find that the state of the system follows a smooth trajectory until the system reaches the saddle node bifurcation of S_u . At this point, the system flips the only remaining stable state (I). In summary, the opening and closing of this system are governed by the crossing of the saddle point of S_u past $\theta = 0$, and the saddle node bifurcation of S_u respectively. Note that here we have chosen an example configuration in which $\varepsilon_c < \varepsilon_b$.

Model Parameters

The proposed slit Bellini Truss matches the qualitative behavior of the slitted beam. However, it features three individual parameters; one more than the physical system

⁴The numerical contours are obtained with ContourPy; the Python library used to calculate contour curves in Matplotlib.

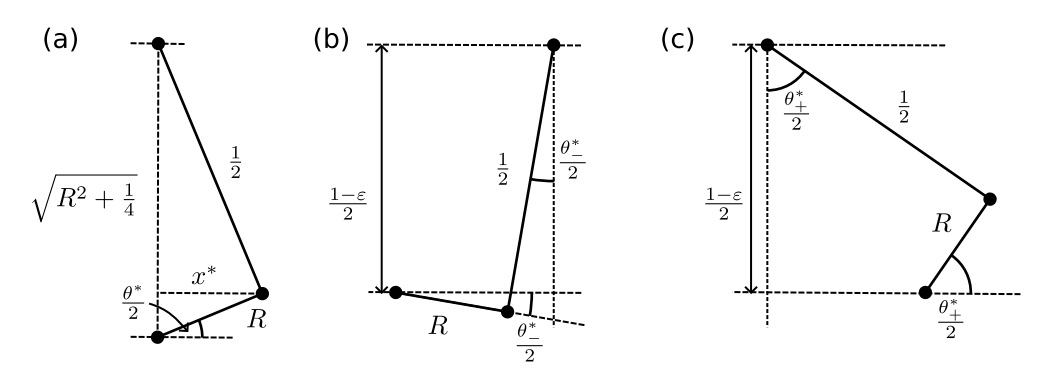


Figure 4.7: Stable configurations of S_u at $\hat{\kappa}_{\theta} = 0$ and E = 0. (a) The symmetric configuration at $\varepsilon = 1 - 2\sqrt{R^2 + \frac{1}{4}}$. (b) A configuration in the self-intersecting left branch. (c) A configuration in the open right branch.

we intend to describe. We will demonstrate that R and $\hat{\kappa}_{\alpha}$ can be chosen to match the geometry of the uncut beam given by t, and that $\hat{\kappa}_{\theta}$ models the slit length s. Specifically, we choose R = t/2, which matches the intuitive picture of a beam that hinges at its edge.

We determine appropriate values of the remaining two parameters $\hat{\kappa}_{\alpha}$ and $\hat{\kappa}_{\theta}$ by considering the limits of $\hat{\kappa}_{\theta}$. In the limit where $\hat{\kappa}_{\theta} \to \infty$, opening the slit is unfeasible, thus we are left with S_f , a system insensitive to R, which can be readily mapped to the buckling problem of a regular beam (appendix Sec B) where $\hat{\kappa}_{\alpha}$ determines the buckling strain ε_b . In the limit where $\hat{\kappa}_{\theta} = 0$, the structure has a mechanism⁵ when $\left|\frac{1-\varepsilon}{2}\right| \leq \sqrt{R^2+1/4}$, i.e. as long as the truss is not pulled into tension. Here, the springs remain of length 1/2, and at right angles to the trusses. Within this regime, the stable configurations can be solved by geometric construction (Fig. 4.7). At $\varepsilon = \varepsilon^* = 1-2\sqrt{R^2+\frac{1}{4}}$, there is a single stable state, and for $\varepsilon > 1-2\sqrt{R^2+\frac{1}{4}}$ the system has two stable configurations, thus this system has a pitchfork bifurcation at ε^* . This bifurcation however, is not symmetric along $\theta = 0$, but instead at $\theta_0^* = 2 \arctan{(2R)}$ and $x_0^* = \frac{R}{2\sqrt{R^2+\frac{1}{4}}}$. At increasing ε , the stable branches follow the equations:

$$\theta_{\pm}^*(\varepsilon) = 2 \arctan(2R) \pm 2 \arccos \frac{1-\varepsilon}{2\sqrt{R^2 + \frac{1}{4}}},$$
 (4.6)

$$x_{\pm}^{*}(\varepsilon) = \frac{1}{2}\sin\theta_{\pm}^{*}(\varepsilon) . \tag{4.7}$$

The unstable branch can not be solved geometrically as it requires a notion of energy, but x_0^* and θ^* yield an estimate for $x_{\rm unstable}(\varepsilon)$ and $\theta_{\rm unstable}(\varepsilon)$ as this branch should

⁵A deformation pathway in which E=0, and the stiffness matrix $\nabla_{x,\theta}E$ becomes singular.

cross through x_0^*, θ^* .

Thus, a slitted beam can be modeled with such a split Bellini truss, by using a constant R and varying only $\hat{\kappa}_{\theta}$ and $\hat{\kappa}_{\alpha}$ to mimic the buckling strain ε_{b} and stiffness of the slit-induced hinge. At $\hat{\kappa}_{\theta} = 0$, we find a system analogous to a fully slitted beam where $s \uparrow 1$, and in the limit where $\hat{\kappa}_{\theta} \to \infty$, we find a system analogous to an uncut beam where s = 0. Note that we find symmetric pitchfork bifurcations in both systems but along different axes of symmetry. This disparity could be used to find a better candidate parameter of R, as it shows up uniquely in the bifurcation point of the $\hat{\kappa}_{\theta} \to 0$ limit.

4.6 Conclusion and Outlook

In this work, we presented both experimental and numerical investigations of the slitted beam under compression. Our study reveals a region of triple stability and observed hysteresis in the response to compressive driving. By adjusting the geometric parameters s and t, we demonstrated the ability to modulate the range of hysteresis, providing a mechanism for tuning the system response. Specifically, controlling the parameter t enables scaling of both switching fields with a quadratic dependence ($\propto t^2$), while fine-tuning s allows precise control over the snap-back closing transition. Thus, with control of both parameters, both switching fields can be tuned independently.

Moreover, we introduced the Slitted Bellini Truss, which effectively models the multistable behavior of the slitted beam. This model is a natural extension of the Bellini Truss [74], and allows to model the slit as due to an offset hinge and an internal rigid self-contact.

Looking ahead, this work lays the groundwork for exploring more complex geometries and materials, with the goal of enhancing control over multistable systems through self-contacts. These findings open up potential applications in fields such as energy absorption, soft robotics, and mechanical metamaterials, where tunable snap-through transitions offer a platform for novel functionality.

Chapter 5

Twistbucklers

A universal platform to construct (meta) materials with arbitrary memory is lacking. Here we realize a framework that allows to construct memory materials that have a multiperiodic response to driving cycles. Our metamaterial is scalable and extendable and gives insight into pathways in complex media. This work is foundational in the eventual goal creation of a Turing complete mechanical metamaterial.

5.1 Introduction

Many materials store information about the past through plasticity [4, 9, 43, 2, 87]. A bucket of sand in with an inserted cylindrical rod for example can store information of the rods motion. As the rod is rotated, the grains of sand rearrange. Initially, rotating the rod is easier but the force required quickly goes up until it reaches an equilibrium[2]. If we stop rotating the rod, the internal rearrangements stop as well. But what is now the information stored in this material? If we were to rotate the rod again, but now in the opposite direction, the force required starts off low again, after which it rapidly increases, but if we were to have rotated the rod in the original direction, the force required would immediately start high. Essentially, the bucket of sand has remembered the previous rotation direction, which we can measure by rotating the rod. [2, 87]. As long as we do not shake the system or otherwise disturb the arrangement of sand particles, this information persists. Although this effect offers a simple method of storing information, only a single bit of information can be recovered, even though the material has a much larger number of stable states.

But often, an easily distinguishable original structure allows us to extract a lot more information from a system. A wooden stick can be engraved to keep track of a tally, a paper movie ticket torn to indicate entry, and the plastic bumper of a car dented due driving in to an unobserved bollard. Because the initial structure of these materials is known, we can infer more complex information from its current state. Clearly, the amount of information stored in a material, and the amount of information that can be deduced from a material are not the same. We argue for the following distinction between information and memory in a material; memory corresponds to information that allows inference of the past.

Thus, an ideal memory material would have easily distinguishable states, that allow us to measure desired features of the past. An ideal platform for constructing memory materials would allow for the construction of many branching bifurcations of the internal state of the system at any desirable driving field (Fig. 5.1a). Additionally, the symmetry of each bifurcation would need to be controlled to allow for the determinism in the system required for reliable behavior (Fig. 5.1b) [50]. For the memory material to remember past events due to a single driving field, the bifurcations would also need to occur both at increasing and decreasing driving field (Fig. 5.1cd).

There is no straightforward method to achieve such a material. Instead, we draw inspiration from the elementary cellular automata[88], simple systems consisting of bistable cells whose next internal state as a response is defined by a rule; an instruction that determines each cells next state by their own and their nearest neighbors states. Although simple in nature, some of these rules demonstrate complex behaviour and specific examples have been shown to be Turing complete.

What we will show here is a continuation of the beam counter metamaterial that is based on elements that twist as they buckle. This twisting motion allows for contact interactions to occur in any rotation direction of each element. First, we will discuss our bistable twistbuckling elements elements. Second, we will elaborate the design of the contact interaction. Finally, we will demonstrate two different systems built upon the framework of interacting twistbucklers. One system with a multiperiodic orbit of length 2, and one with a cellular design and a multiperiodic orbit of length 6, which can be scaled up to achieve arbitrary lengths.

5.2 Twistbucklers

Our metamaterial consists of 'twistbuckler' elements that buckle and then twist under compression, and which interact with other elements through rigid contacts. Each element consists of a thin rubber corrugated shell, a thick base, and a rigid plastic

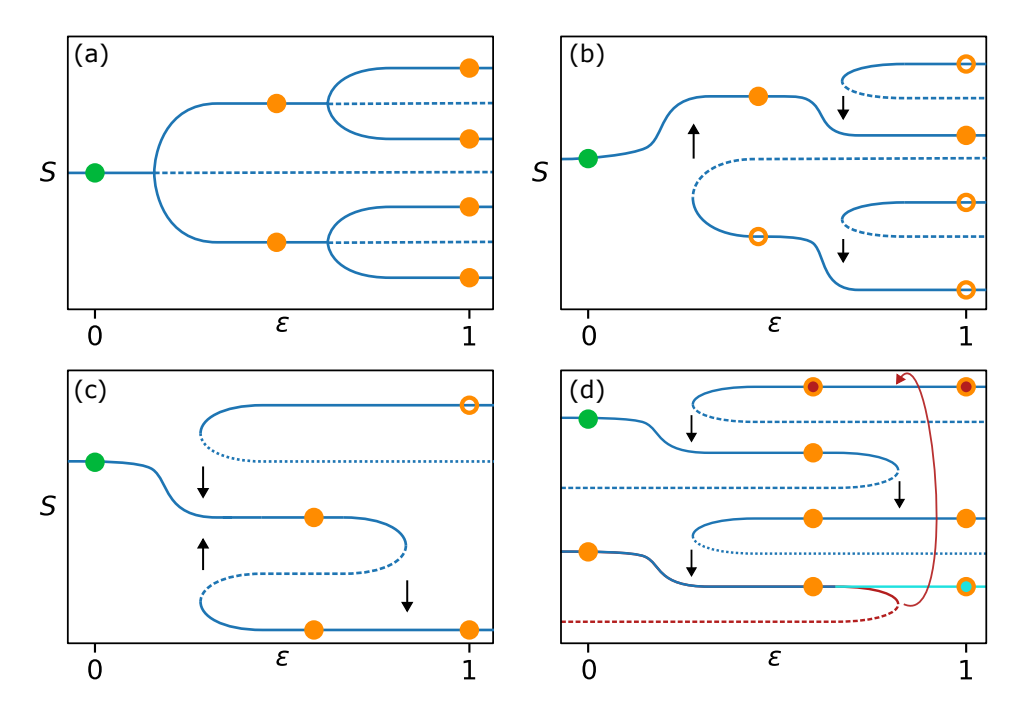


Figure 5.1: State-drive diagrams of various hypothetical systems. S represents the state of the system, while ε indicates the external drive applied to the system. Filled dots are accessible from an initial state at $\varepsilon = 0$ (green). The system follows a path along the solid blue lines, and is unstable along the dashed lines. We are concerned with the accessible through cyclic driving in ε . (a) A system with multiple subsequent symmetric buckling transitions. Due to the symmetry of the pitchfork bifurcations, the exact path taken at increasing ε is determined by imperfections or outside influences. (b) When introducing asymmetry at the bifurcations in the system of a, the path is controlled and it becomes deterministic. This introduces irreversible transitions that occur at decreasing ε indicated by the arrows (this system is similar to the sequential buckling system introduced by Coulais et al. [50] where the biased hinges and self-contact are used to bias muli-step folding). When starting in the initial configuration, some stable states are unreachable when just driven in ε . (c) A system with an irreversible transition that occurs under increasing ε (this system is similar to a slit beam that is biased to buckle right (see chapter 4)). (d) A system that features a transient path that ends in teal, and a cyclic path that loops back in red. The transient path is similar to the counting beams system from chapter 2, the cyclic path is similar to the clicker in a retractable pen. All these diagrams show loop-irreversible behavior for some states when starting at $\varepsilon = 1$ and driving to $\varepsilon = 0$ and back. Only the diagram of figure d shows loop-irreversible when driven from ε from $0 \to 1 \to 0$ as the final state at $\varepsilon = 0$ is different from the starting state. This blue path has transient behavior, after reaching the orange configuration at $\varepsilon = 0$, there are no accessible loop-irreversible paths.

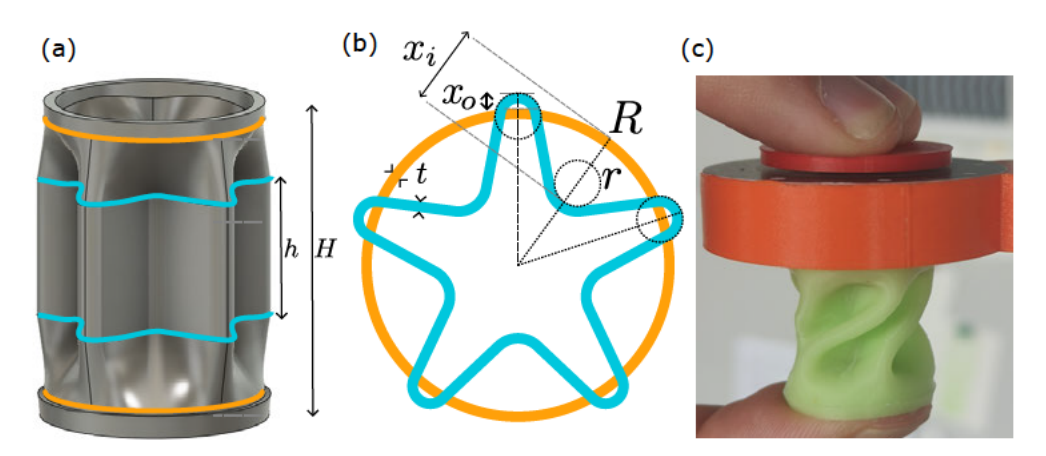


Figure 5.2: The twistbuckler. (a) The complete shape of the twistbuckler shell with highlighted hoops. (b) The curved geometry of the intersections of the ruled surfaces. (c) A full twistbuckler with cap, compressed by hand such that it buckles and twists. Note that the ruled surface defines the outside of the twistbuckler geometry. The final shape is determined by extruding this surface inward by the thickness t.

cap which houses a freely rotating (using a ball-bearing) plunger (Fig. 5.2a-c). These caps are interchangeable and are press-fit into the shells. When applying a sufficiently large compression Δ , the shell buckles and the entire assembly twists left or right, reaching an angle θ (Fig. 5.2c).

The rubber shell geometry governs the buckling behavior of the twistbucklers. Qualitatively, the design is based on the formation of folds and subsequent twisting observed for thin-walled ring-stiffened cylinders under external pressure [89, 90, 91, 92, 93], and on the dimples that occur under axial compression [94, 95, 96]. To model the surface, we took inspiration from origami bellows [97, 53]. The surface consists of a stack of three minimal area ruled surfaces that connect four circular and lobbed hoops that are modeled as rounded versions of the Miura-ori and Kresling fold patterns (Fig. 5.2b).

The samples are parametrized by the following parameters (Fig. 5.2b):

- *H*, the height the sample,
- h/H, the length of the folding section,
- R/H, the width of the sample,
- r/R, the radius of the folds,
- x_i/R , the distance by which the folds curve in,
- x_o/R , the distance by which the folds curve out,

• t/R, the effective wall thickness.

The Cauchy rigidity condition in essence states that instabilities require local concave regions [98]. This motivates taking x_i sufficiently large. We also explored the effect of the number of folds or lobes, which influences the higher order buckling modes, self-contact and stiffness. We focus on a single design that was easy to manufacture and which experimentally was found to function well, and applied this design in all our (meta)materials. We hence introduce heterogeneity via the design of the caps, as these offer a simple mechanism for controlled interactions and asymmetry.

Sample Homogeneity and Buckling

To probe the homogeneity of our samples and measure the range of observed angles, we tracked the buckling branches of a set of 13 isolated twistbucklers with parameters: H=25 mm, h=12.40 mm, R=10 mm, r=1.47 mm, $x_i=5$ mm, $x_o=1$ mm, and t=1 mm. To measure this rotational response, we built a setup that compresses the twistbucklers against a transparent acrylic plate. The caps of the twistbucklers are marked with a fiducial as shown in Fig. 5.3a, and tracked with a camera that is mounted normal to the acrylic plate. We used the same cap to eliminate the variation in manufactured cap dimensions and used a fixed location on the acrylic plate. Before starting our measurements, we fix the zero compression with an assembled sample by eye. This offset stays fixed for all samples and introduces a consistent systematic error of around ± 0.1 mm.

For every sample, we slowly compress at a rate of approximately 0.2 mm/s to $\Delta = 6.25$ mm, resulting in a maximal compressive strain $\varepsilon = \Delta/H = 0.25$. During compression, the cylinder exhibits twistbuckling. We manually adjust the rotation direction during this compression, after which we decompress at the same rate and track the rotation angle of the cap. We compress each sample twice, capturing both rotation branches. This results in 26 tracks of the rotation angle θ as a function of the applied strain (Fig. 5.3). The angle θ is measured relative to the final snapshot taken at $\varepsilon = 0$ at the end of the experiment.

To better interpret the homogeneity and symmetry of the samples near buckling, we compare the strains at a fixed rotation of $|\theta| = 0.5$ (Fig. 5.3c). We observe a minor left-right imbalance; most samples preferentially rotate left at a lower strain than right. Furthermore, the buckling strains between samples varies as well. To better judge the effect of this heterogeneity, we compare the tracked rotations, juxtaposing the various traces in θ for each combination of twistbuckler (Fig. 5.3d). We observe an initial dilation of the traces up to around $|\theta_i| = 0.25$ after which the traces converge.

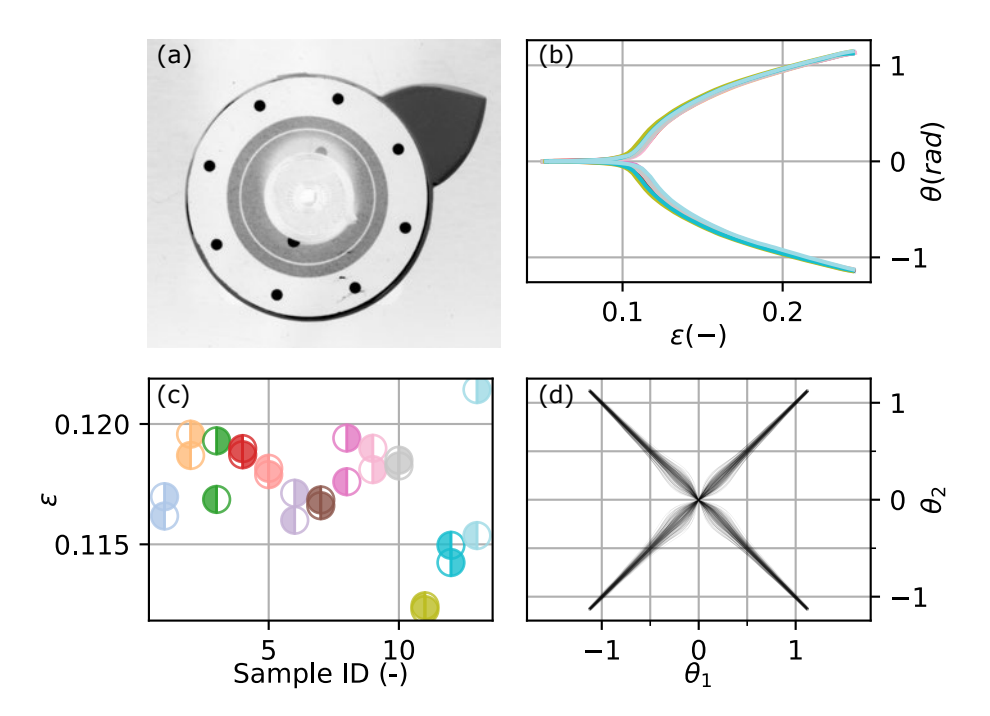


Figure 5.3: Tracked rotation trajectories of individual, free twistbucklers. (a) The cap with tracking markers taken through the transparent acrylic compression plate. (b) The tracked rotated angle θ as compared to the initial frame taken, as a function of the compressive strain ε for 13 near identical samples in both stable states measured during decompression. Every sample is represented by its own color. The major variations between the responses occurs near the buckling bifurcation. (c) The strain ε at $|\theta| = 0.5$ rad for the left and right branch of each sample. This indicates the variation in buckling strain for each sample, both between samples and within a sample between the left and right branches. The left-shaded disc corresponds to the left buckling branch and the right-shaded disc to the right buckling branch. (d) All possible trajectories for pairs of twistbucklers as a function of ε . Each trace corresponds to a combination of two branches highlighting the effect of small deviations in buckling strain. Ideal traces would lie along the diagonals $\theta_2 = \pm \theta_1$.

Our measurements evidence a high level of homogeneity between samples, as well as good symmetry of the individual samples. The largest spread between curves occurs near the bifurcation itself, as the actual bifurcation direction is highly sensitive to imperfections. Controlling the motion of interacting twistbucklers requires overcoming this unwanted heterogeneity, which we will accomplish by appropriate design of the caps.

Moment Strain and Twist

While the measurements of θ as a function of ε demonstrate the behavior of freely rotating twistbucklers, to characterize interactions between twistbucklers we also need to measure the moment T as a function of both ε and θ . To do so, we constructed a setup that allows us to constrain the rotation θ and ε in tandem. Our setup consists of an adjustable clamp, a bowdrill and an Instron universal testing machine as shown in Fig. 5.4a. The bowdrill consists of a tensioned bow and a string that is wrapped around a pulley by 1.5 turns. As the bow is moved, the pulley rotates without slipping¹. The Instron is used to move the bow, twisting the twistbucklers, and measure the corresponding force. The pulley is attached to the twistbuckler, and both the pulley and a nylon string are of a known diameter allowing us to calculate the twist θ and moment T from the Instron force displacement data. The clamp attaches to the pulley on the static side, and to a flat moveable stage side that allows the twistbuckler to slip. The moveable side is controlled with a micrometer stage.

As shown in Fig. 5.4, we observe a drastically changing response as a function of ε . We initially observe a linear relation between θ and T, but as ε increases the stiffness of the twistbuckler rapidly declines until around $\varepsilon = 0.12$, where locally at $\theta = 0$ the stiffness becomes negative indicating a buckling bifurcation of the free structure. As we continue, at around $\varepsilon = 0.34$ a second bifurcation occurs, now of a previously unstable state, which results in a third stable angle around $\theta = 0$; the system becomes tristable. This same mode can easily be observed by hand as well, by fixing the θ and compressing the structure well past the initial buckling point. When this configuration is decompressed (increasing ε), a snap to one of the two regular stable configurations is observed (Fig. 5.2c).

We find that the twistbucklers buckle symmetrically as intended and perform like a nearly ideal bistable element up to $\varepsilon = 0.26$ at which it has stable twisting angles of $\theta = \pm 1.2$ rad (Fig. 5.4c). We note that we observe some hysteresis in the $T(\theta)$ curves, leading to a spread in the stable θ configurations. This hysteresis is likely due

¹As a result from Euler and Eytelwein, the effective friction due to wrapping a flexible inextensible rope around a pulley is greatly increased [99, 100]. The effective friction coefficient is $\mu_{eff} = 1 - e^{-\mu\phi}$, where the rotion angle of ϕ in is radians.

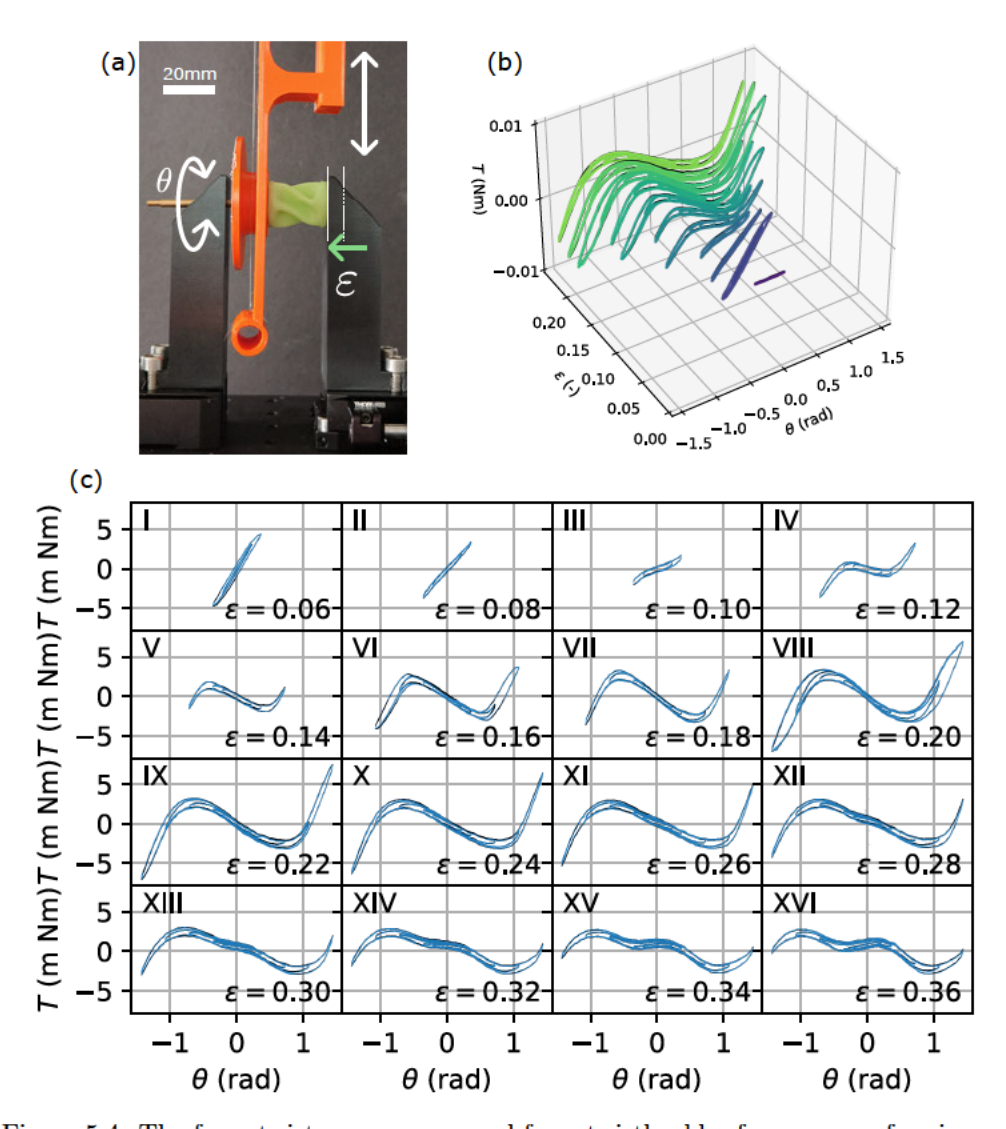


Figure 5.4: The force twist curves measured for a twistbuckler for a range of various ε . (a) Illustrated bowdrill system. (b) 3D Plot showing the measured moment T (torque) for a part of the data illustrating the transition from the linear behaviour to the bistable regime. The color corresponds to the applied strain ε . (c) Individual plots of T as a function of θ for various ε .

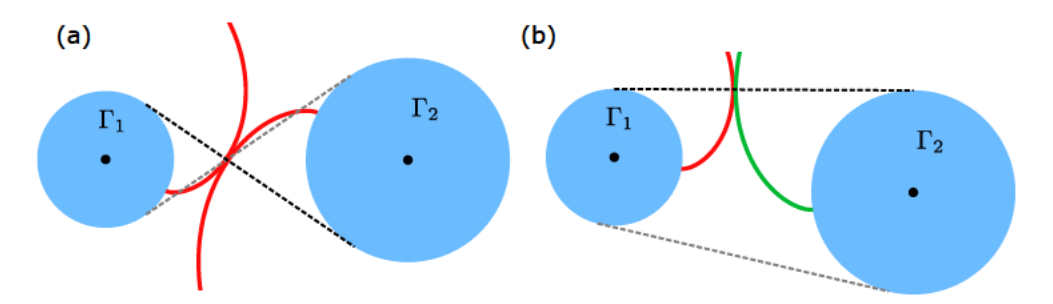


Figure 5.5: Illustration demonstrating the two types of flank-flank contact. Contact between the curves occurs along the contact spaces indicated with dashes lines. (a) Regular gear contact between two right-handed curves. (b) Mercier contact between curves of opposite handedness. Note that Mercier contact does not occur at a point on the line that connects the centers of rotation of the two curves.

to a combination of residual friction in the bearing and the material properties of the twistbuckler shell. The resulting spread in the equilibrium configurations is of the order of ± 0.2 rad, and has to be taken into account in order to obtain robust designs of interacting twistbucklers.

5.3 Interacting Twistbucklers

The configuration of a pair of twistbucklers is characterized by ε and their respective rotation angles θ_1 and θ_2 . The interaction between the twistbucklers occurs through rigid contact between spur-gear-like teeth, and takes the form of excluded volumes, or blockades, in the angular configuration space.

When the surfaces of the caps of two twistbucklers remain in contact, this leads to a geometric relation between the rotation of the twistbucklers: when twistbuckler one rotates by an angle $\Delta\theta_1$, twistbuckler two rotates by an angle

$$\Delta\theta_2 = \kappa \Delta\theta_1 \ , \tag{5.1}$$

where κ is determined by the shape of the surfaces in contact. We will consider contact surfaces that follow curves which are the involutes of circles (Fig. 5.5). An involute curve is constructed by tracing the end of a taut string as it is unwrapped from a shape (See appendix C). When such surfaces are in contact, κ is constant, and its absolute value depends on the radii of the circles from which the curves are developed. The sign depends entirely on the handedness of the curves. Equally handed curves form 'ordinary' gear contact (κ < 0), and oppositely handed curves

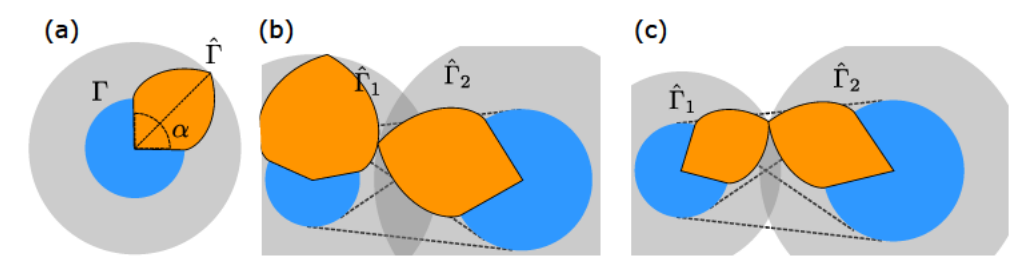


Figure 5.6: Tip contact for finite sized teeth with a tip radius $\hat{\Gamma}$. (a) The geometry of a single tooth, with a base radius of Γ and a splitting angle of α . The green circle indicates the base radius Γ and the light gray circle indicates maximal radius $\hat{\Gamma}$. The axis of rotation is at the center of these two circles. (b) Tip flank contact at the circular arcs of the lenticular patch determined by the overlap of the $\hat{\Gamma}_1$ and $\hat{\Gamma}_2$ base circles. The dashed lines correspond to the possible contact spaces of flank-flank contact such as in Fig. 5.5. (c) Tip-tip contact at one corner of the lenticular patch. Note that the Mercier-contact lines are outside of the lenticular patch.

form 'Mercier' contact($\kappa > 0$). Mercier gears, otherwise known as paradoxical gears rotate in the same direction as their neighbours.[101] For two flanks with base radii Γ_1 and Γ_2 ,

$$|\kappa| = \Gamma_1/\Gamma_2 \ . \tag{5.2}$$

The ratio κ can be thought of as the gear-ratio of the two contact-surfaces; note that this ratio does not require multiple teeth, but is well-defined for a pair of flanks as well. We can visualize this coupling as due to a taut string wrapped around pulleys with radii Γ_1 and Γ_2 (Fig. 5.5). Notice that the point of contact between the flanks lies on the lines corresponding to the strings. Due to the technique of constructing involute curves, all points of contact between such curves occurs along these lines. Depending on whether the strings cross, we obtain normal gears or Mercier gears [101, 102], where for ordinary gear contacts $\kappa < 0$, and for Mercier gear contacts $\kappa > 0$ (Fig. 5.5). The type of contact can be distinguish by the handedness of the flanks in contact (Fig. 5.5)². Equal handed curves are in regular contact, whereas oppositely handed curves are in Mercier contact.

We design our teeth by combining a left-handed flank based on a circle with radius Γ^L and a right-handed flank with base radius Γ^R , where the roots of both curves are separated by an angle α (Fig. 5.6a). The left and right flanks intersect in a tip, resulting in the maximal radius $\hat{\Gamma}$. For symmetric teeth where $\Gamma = \Gamma^R = \Gamma^L$, we can

²That κ is constant for circle involute curves is one of the reasons why involute curves are used in ordinary spur gears [103, 104, 105].

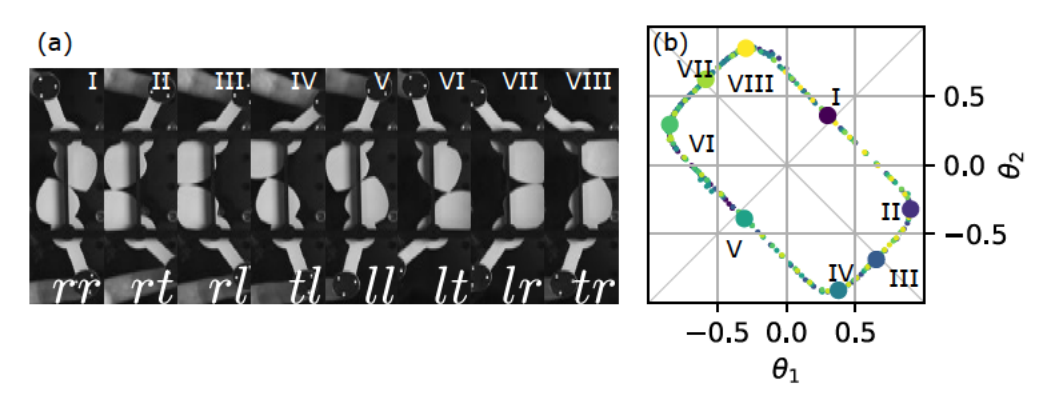


Figure 5.7: The measured interactions between caps due to teeth with a finite size. (a) Eight different contact conditions of homogeneous caps. (b) The manually explored phase space, and the modeled blockade, of two homogeneous symmetric twistbuckler caps. The marked dots in blue orange and green correspond to the frames in subfigure b respectively. The measured data is superimposed on the analytically derived blockade shape.

easily derive an analytical expression for α as a function of Γ and $\hat{\Gamma}$:

$$\alpha = \alpha(\Gamma, \hat{\Gamma}) = \sqrt{\frac{\hat{\Gamma}^2}{\Gamma} - 1} - \arctan\sqrt{\frac{\hat{\Gamma}^2}{\Gamma} - 1}$$
 (5.3)

The finite radius $\hat{\Gamma}_i$ makes the actual contact space where the teeth interact finite. For two teeth with contact radii $\hat{\Gamma}_1$ and $\hat{\Gamma}_2$ at a distance D, all contact has to occur within the lenticular shape defined by the circles with corresponding radii (Fig. 5.6b-c). Moreover, the presence of the tip requires to consider additional types of contact surface, so called tip-flank contacts and tip-tip contacts (Fig. 5.6b-c) as we will discuss in the next section.

Phenomenology of symmetric teeth pairs

To gain insight into the shape of the blockades, we experimentally investigate the blockades for pairs of teeth. Let us first discuss and elaborate the contact between a pair of equal teeth with parameters $\alpha = 92^{\circ}$, $\Gamma = 0.29$, $\hat{\Gamma} = 0.61$, at a fixed distance D = 69 mm. By manually rotating both caps while keeping their surfaces in contact, we observe three different types of contact over eight sections: between equal handed flanks (rr, ll), between oppositely-handed flanks (rl, lr), and between one tip and one flank (lt, tr, rt, tl) (Fig. 5.7a). We observe that as we rotate the caps while maintaining contact, the contact type smoothly transitions through interchanges of

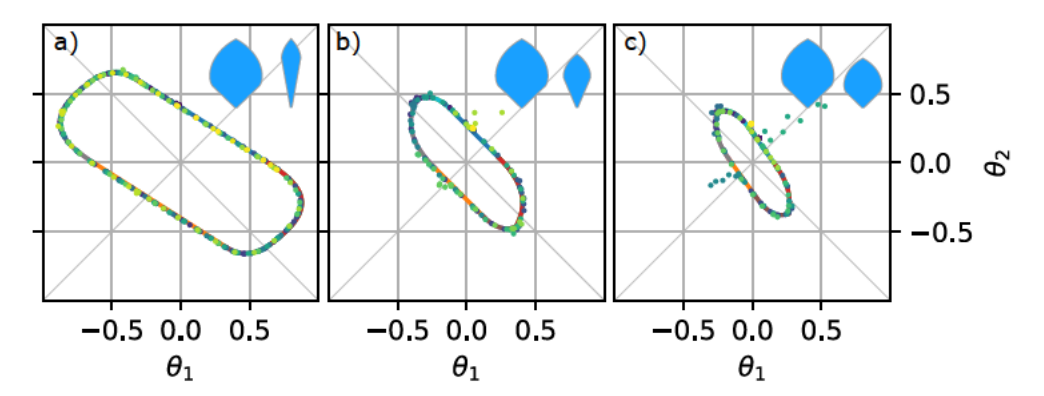


Figure 5.8: The measured interactions of caps with unequal teeth. (a) At equal $\hat{\Gamma}_1 = \hat{\Gamma}_2$, and unequal $\hat{\Gamma}_i$ and α_i . (b) At equal $\hat{\Gamma}_1 = \hat{\Gamma}_2$, and unequal $\hat{\Gamma}_i$ and α_i . (c) At equal $\alpha_1 = \alpha_2$, and unequal $\hat{\Gamma}_i$ and $\hat{\Gamma}_i$. The measured data is superimposed on the analytically derived blockade shape and an illustration of the shape of the teeth is inset in the top right corner of each plot.

one of the two surfaces. Starting in the rr contact space (Fig. 5.7I) where both right-handed flanks are in contact, the system transitions to the rt (Fig. 5.7II) contact space where the right-handed flank of cap one and the tip of cap two are in contact, or the tr (Fig. 5.7VIII) contact space where the tip of cap one and the right flank of cap two are in contact, depending on the direction of rotation. Moving in the former direction, the system transitions through contact types rr, rt, rl, tl, ll, lt, lr, tr, and through the opposite sequence for opposite rotations.

By tracking the rotation of both caps, we can plot the perimeter of the blockade (Fig. 5.7b). We note that for this example of teeth of equal parameters, the blockade appears approximately rectangular and features D_2 symmetry; both mirror symmetry along the $\theta_1 = \pm \theta_2$ axes as well as rotation symmetry by π radians (Fig. 5.7b). The slopes of the blockade are diagonal and correspond to the constant ratios $|\kappa| = \Gamma_1/\Gamma_2 = 1$. Specifically, we observe ordinary gear contacts that lead to negative slopes, Mercier gear contacts that correspond to positive slopes and tip-flank contacts which produce the rounded corners that form the connection between ordinary gear and Mercier contacts. We find that the measured blockade matches well with the model. The measured blockade in Fig. 5.7b is symmetric along the expected axes with the correct slopes.

As we assume that the twistbuckler shells are symmetric, their observed post-buckling rotation direction is not determined by their design. Furthermore, as the moment of the twistbuckler shells is antisymmetric in θ : $T(\theta) = -T(\theta)$, a coupling of $\kappa = 1$ will result in rotations of both twistbucklers of equal magnitude in two possible directions $\Delta\theta_1 > 0$ & $\Delta\theta_2 < 0$ or $\Delta\theta_1 > 0$ & $\Delta\theta_2 < 0$ and likewise for $\kappa = -1$, we observe both

the $\Delta\theta_1 > 0$ & $\Delta\theta_2 > 0$ and $\Delta\theta_1 < 0$ & $\Delta\theta_2 < 0$ directions of rotation. However, by controlling κ away from ± 1 , this symmetry can be broken and the rotation directions of a pair of coupled twistbucklers can be controlled.

Exploring blockades with broken parameter symmetry

We now consider three different pairs of unequal teeth to explore how asymmetries in the parameters Γ_i , $\hat{\Gamma}_i$ and α_i impact the shape of the blockade. As the teeth shapes are overdetermined, we choose three pairs of teeth where one of these parameters is equal for both teeth, and the other two are different.

First, we decrease α_2 and increase Γ_2 while we fix $\hat{\Gamma}_1 = \hat{\Gamma}_2$. This produces a change in the slopes of the blocked regions κ (Fig. 5.8a) and the blockade looks like a parallelogram with rotational symmetry C_2 . In particular, we find that $\pm |\kappa| = \pm \Gamma_1/\Gamma_2$ as expected. Moreover, the blockade has decreased in size and has become more narrow in the θ_2 direction. Hence, this modification changes the coupling constant κ .

Second, we decrease α_2 and increase Γ_2 while keeping $\Gamma_1 = \Gamma_2$. As expected, the regular contact slopes of the blockade are along the $\theta_1 = \pm \theta_2$ axes, but the tooth-flank contact spaces are no longer mirror-symmetric and the Mercier contact has disappeared (Fig. 5.8b). Instead, we now observe tip-tip contact and a transition from lt to tr, and rt to tl through the two tip-tip contact conditions. Moreover, the size of the blockade has dramatically gone down. This blockade again has C_2 symmetry.

Third, we decrease both Γ and $\hat{\Gamma}$ while we fix $\alpha_1 = \alpha_2$. We observe a combination of both effects; a decrease in κ as well as a change in the tip-flank contact. Furthermore, this blockade has drastically gone down in size, and we again observe tip-tip contact. Although the resulting blockade is approximately D_2 , it is not mirror-symmetric, as we will show in the following section.

Evidently, there are two distinct effects from breaking the symmetry between pairs of teeth: (i) modifying κ for flank-flank contacts for constant $\hat{\Gamma}$, and (ii) breaking point-flank contact symmetry for constant Γ , driven by differences of the base radii Γ_i and the splitting angle α_i .

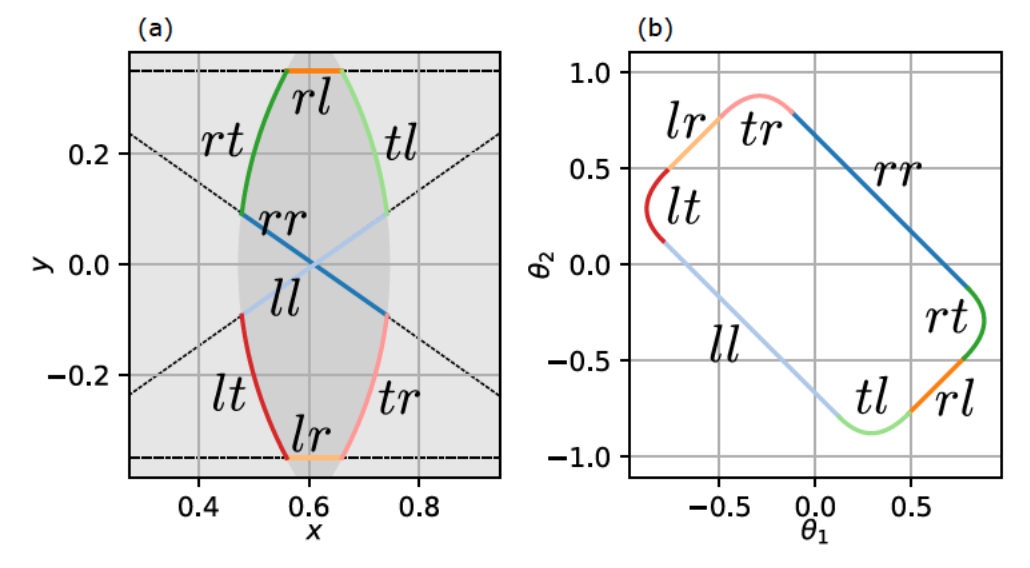


Figure 5.9: An illustration of the contact space in real-space and the corresponding blockade in configuration space 5.7. (a) Real space contact curves for $\Gamma_1/D = \Gamma_2/D \approx 0.287$ and $\alpha \approx 1.61$. Every point corresponds to a configuration of teeth in contact. The different types of contact are color coded and labeled. (b) Configuration space contact curves with labels matching the diagram from a. In transforming the real-space to configuration space, the transformation makes explicit use of the angles $\alpha_1 = \alpha_2 = 92^{\circ}$. Not pictured here is tip-tip contact which occurs when Mercier contact vanishes.

Analytical determination of the blockades

For the contact surfaces used here, the real-space contact space can be geometrically constructed and analytically transformed to find the blockade shape (see appendix C). For flank-flank contact, all points of contact occur along the regular and Mercier contact curves shown in Fig. 5.5, and are bounded by the maximal radii of both teeth which form a lenticular patch (Fig. 5.9a). All contacts involving a tip, occur at the maximal radius of at least one of the teeth. The tip-flank contact space corresponds the circular arcs of the lenticular patch that connect the sections in the order mentioned previously in Sec. 5.3.

To transform the real-space contact to the configuration space, we triangulate each point using the known distance D, the two points of rotation, and the angles from which the involute curves start. To study the effect of the parameters on the observed blockades in detail, we use a simple numerical code that performs these operations for arbitrary teeth pairs. This allows us to demonstrate the effect of teeth size on the observed blockade shape. For posterity we included a number of calculated blockade shapes in fig. 5.10 for unequal teeth similar to those shown in fig. 5.8

Let us first consider changing the effective size of the teeth, either through changes of the dimensions Γ and $\hat{\Gamma}$ of both teeth, or equivalently to changing D (Fig. 5.11a-b). We calculated the blockade shape, by evaluating the contact space for 15 discrete values of D between $D = \Gamma + \hat{\Gamma}$ (Fig. 5.11aI) and $D = \hat{\Gamma} + \hat{\Gamma}$ (Fig. 5.11aII) — see Fig. 5.11b. We observe that as we decrease D, the blockade increases in size. At large D, the blockade shape is governed by tip-flank and regular gear contacts. At small D we observe a large regular gear regime, and a smaller Mercier-gear regime. Hence, decreasing D or increasing the dimensions Γ and $\hat{\Gamma}$, increases the size of the blockades.

Another method of varying the size of the teeth, is trough changing the opening angles α_i . We calculated the shape of the blockades for angles between 10°(Fig. 5.11cI) and 230°(Fig. 5.11cI). Similar to decreasing D, increasing α leads to an increase in the size of the blockade. However, when increasing α , the Mercier-like regime grows more rapidly than the normal-gear regime. This can easily be demonstrated geometrically (see appendix C). We expect that when increasing $\alpha \to \phi \alpha$, the mercier regime grows by a factor $\sqrt{2}\phi$, whereas when scaling up the dimensions by ϕ or similarly decreasing $D \to D/\phi$, we expect the Mercier regime to grow by ϕ .

In this section, we studied the coupling between twist bucklers through contact using teeth with flanks which follow the involute of a circle. For such coupling we find that the magnitude of the coupling ration κ is constant and either positive or negative depending on whether the surfaces in contact are either opposite or equal handed

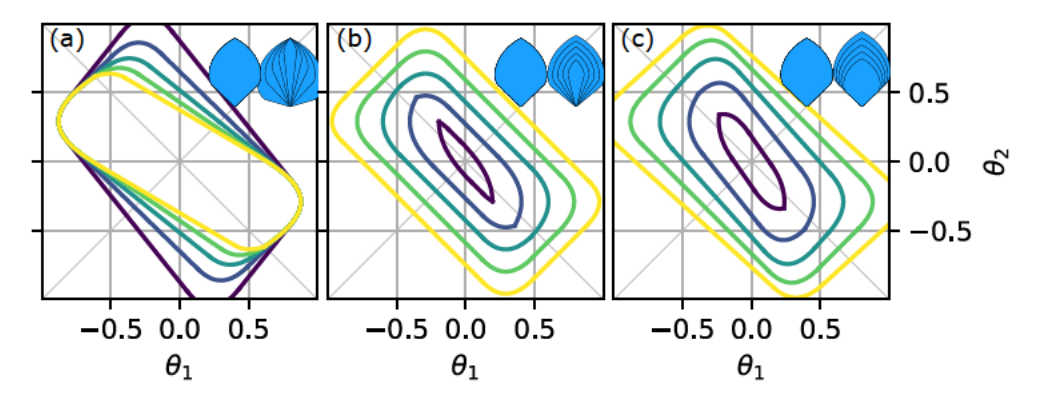


Figure 5.10: Calculated blockades for a range of different teeth with asymmetries comparable to those in fig. 5.8, for many different parameters. (a) At symmetric $\hat{\Gamma}_1 = \hat{\Gamma}_2$, and asymmetric Γ_i and α_i for five values of Γ in the range (0.28, 0.60). (b) At symmetric $\Gamma_1 = \Gamma_2$, and asymmetric $\hat{\Gamma}_i$ and α_i for five values of α in the range (0.48, 1.8). (c) At symmetric $\alpha_1 = \alpha_2$, and asymmetric $\hat{\Gamma}_i$ and Γ_i for Γ in the range (0.24, 0.39).

respectively. For contact that includes the tip of finite sized-teeth, the blockade boundary connects both regions with an intermediary smoothly evolving κ .

Through experimental and analytical investigations, we studied the resulting blockades; the parts of phase space blocked by contact. We first considered symmetric teeth with equal base radii Γ , opening angle of α , and a tip radius $\hat{\Gamma}$. For these teeth we found two distinct blockade size effects allowing us to tune the ratio of the regulargear and mercier-gear contact regimes. For asymmetric teeth we found two distinct chiral effects for asymmetric tooth modifications, influencing the coupling constant κ or influencing the tip-flank contact. Second, we showed how the exact shapes of blockades can be determined. We studied how the sizes of blockades correspond to homogeneous tooth size, and how the three variants of tooth-size asymmetry result in combinations of two distinct effects. As the shape of the blockades can be analytically determined as a function of the teeth parameters, we can thus determine κ along the blockades, for various tooth parameters and for various types of contact.

Our findings suggest that by carefully designing the teeth of twistbucklers, one can control the direction and magnitude of their rotational coupling, thus enabling the deterministic behavior of the system. This capability to manipulate the coupling characteristics opens new possibilities for designing mechanical systems with specific, predictable responses based on geometric configurations.

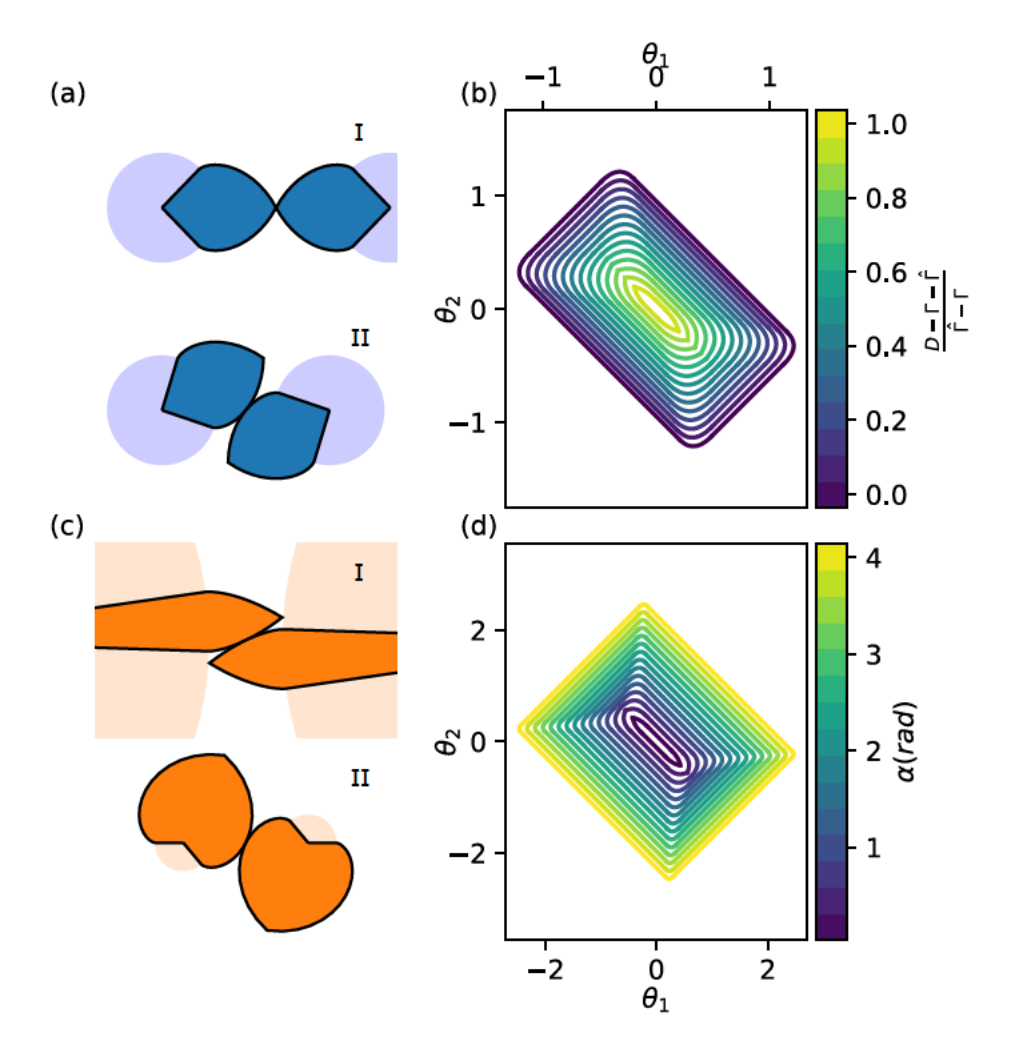


Figure 5.11: The effect on the blockade shape for two types of symmetric tooth modifications. (a) Moving in and out or equivalently scaling up and down teeth with a constant $\alpha = 92^{\circ}$. At the maximal distance, $D = 2\hat{\Gamma}$, (i) the caps are only touching at the tips, and at the minimal distance $D = \Gamma + \hat{\Gamma}$ (ii) the caps are spaced such that the tip of one tooth can touch the base circle of the other. (b) The calculated blockade shapes for 15 different D for the homogeneous teeth from (a). The Mercierlike contact for these gears appears at around $\frac{D-\Gamma-\hat{\Gamma}}{2\hat{\Gamma}} = 0.6$ (c) Contact between the right-flanks for α between 10° and 250° at a constant $D = \Gamma + \hat{\Gamma}$ and (d) the corresponding blockade shapes. When increasing α , the Mercier regime grows rapidly.

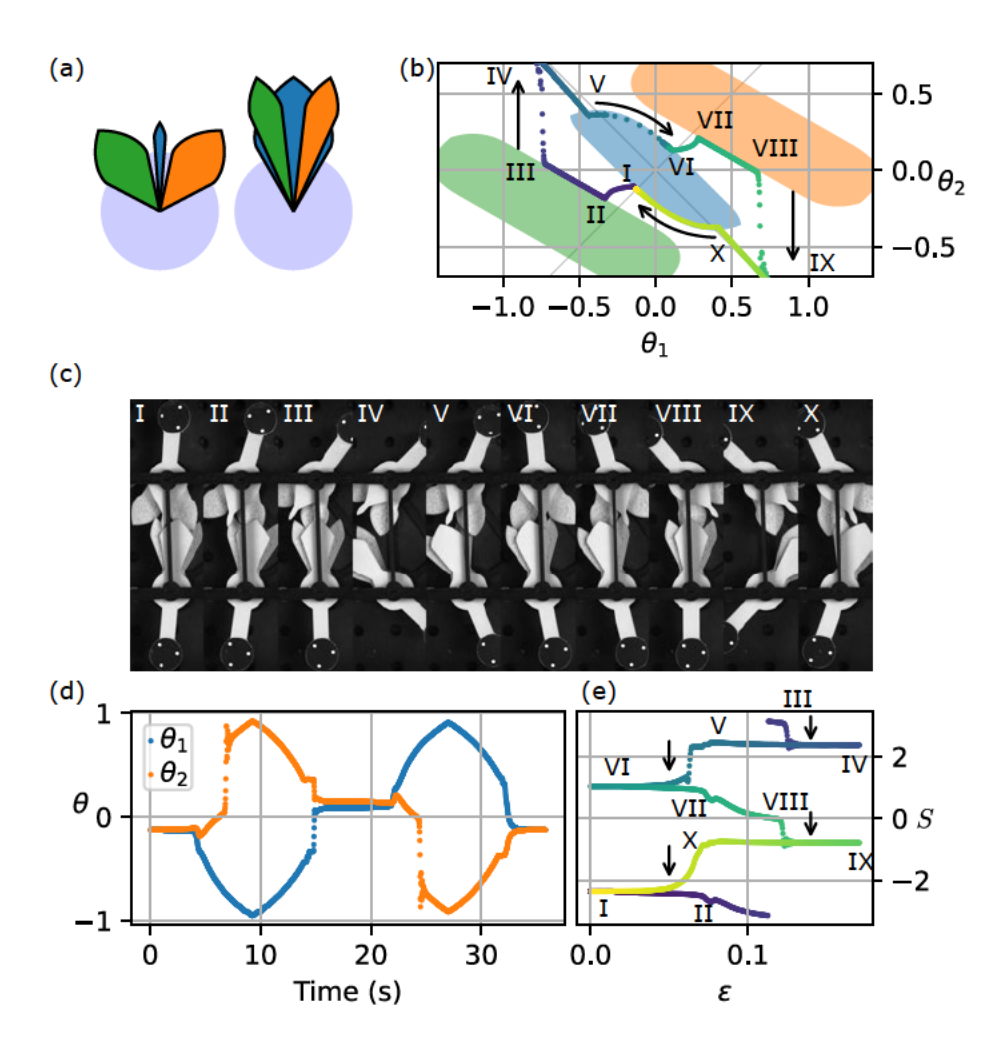


Figure 5.12: The behavior of the two-twistbuckler parity machine. (a) The geometry and parameters of the twistbuckler caps. (b) The phase space blockades and the measured (θ_1, θ_2) response to two driving cycles in ε (between $\varepsilon = 0$ and $\varepsilon = 0.172$). (c) Snapshots of the two twistbucklers at six specific configurations illustrating the phenomenology of the system: the starting configuration in a state where $\theta_1 < 0$ and $\theta_2 < 0$ at $\varepsilon = 0$ (I), initial contact between the flippers (II), the configuration around $\theta_2 = 0$ before snapthrough (III), the $(\theta_1 < 0, \theta_2 > 0)$ state after snapthrough (IV), contact between the meshing teeth along the $(\theta_1 = -\theta_2 > 0)$ diagonal (V), after re-meshing in the new stable resting configuration at $\varepsilon = 0$ in the $(\theta_1 > 0, \theta_2 > 0)$ state (VI). From (VI) to (X) and back to (I), we follow a similar trajectory but where θ_1 and θ_2 are permuted. (d) THe angles θ_1 and θ_2 as a function of time. (e) A representation of the continuous state of the system $S = \arctan \theta_2/\theta_1$ as a function of ε .

5.4 Parity Machine

Combining our previous results, we construct a system of two twistbucklers that mimics a parity machine, i.e., a device which returns to its initial configuration after two compression cycles [26]. This striking behaviour requires a complicated bifurcation structure which we achieve using blockades. Without interactions, a system of two twistbucklers has four individual stable branches that move out and in at increasing and decreasing ε (Fig. 5.3d). By perturbing these stable branches with blockades, a complex pathway cyclic pathway is formed (similar to that shown in Fig. 5.1d), such that at every compression cycle of the system, the stable state of the system is flipped to the opposite stable resting configuration.

Parity Machine Design

Here we use two caps with three teeth stacked vertically (Fig. 5.12a). Due to this layering, the final formed blockade is a composite of the blockades of the individual layers. Each tooth is placed at an angle β with respect to the neutral axis between the centers of rotation of the two twistbucklers which translates the blockades in configuration space. Placing blockades near the neutral point $\theta_1 = \theta_2 = 0$, influences the trajectory of the system at small ε . Blockades further away influence the trajectory at large ε . By further tuning α and Γ for each tooth, the individual size and shape of each individual blockade can be controlled.

To obtain the parity machine behaviour, we use two types of teeth pairs. We use a single "mesher" pair with parameters $\Gamma_1^m/D=0.296$, $\Gamma_2^m/D=0.519$, $\alpha_1^m=50^\circ$, $\alpha_2^m=18^\circ$, $\beta_1^m=\beta_2^m=0$, and two pairs of "flippers" with parameters $\Gamma_1^f/D=0.296$, $\Gamma_2^f/D=0.519$, $\alpha_1^f=50^\circ$, $\alpha_2^f=18^\circ$, $\beta_1^f=\pm0.65$ (rad), $\beta_2^f=\pm0.27$ (rad). This results in the composite blockade shown in Fig. 5.12b. The parameters of each tooth are chosen to break the interaction symmetry (the exchange symmetry between twistbucklers) sufficiently strong to overcome the imperfections of the twistbuckler shells. Note that blockades do not overlap, so that the contacts are mutually exclusive, i.e., there is contact between at most a single pair of teeth. To enforce a constant D and align the β angles, the twistbucklers are constrained with a bracket. As $\beta_1^m=\beta_2^m=0$, we require that the mesher teeth overlap at a rotation angle of $\theta_1=\theta_2=0$. To accomplish this, and accurately build the system, the bracket features a repeatable 90° rotation adjustment for both twistbucklers. This allows us to first construct the system without contact, and then rotate both twistbucklers to correctly place the mesher blockade on the origin of the configuration space.

5

Parity Machine Results

We now discuss the choice of tooth parameters by going through a compression cycle in steps, starting in the initial configuration I (Fig. 5.12bc) where $\theta_1 = \theta_2 < 0$. As the system is compressed, the initial contact between the mesher pair is broken, and the magnitude of rotation of both twisters increases. Note that experimentally, the angles do not follow an ideal diagonal path in phase space due to imperfections of the samples (Fig. 5.3d). As ε is increased further, contact is formed between co-handed flanks of one pair of flipper teeth at II (Fig. 5.12cII). Next, while still increasing ε , the flipper teeth are pushed together which couples the rotation of the two twistbucklers. As $\Gamma_1 < \Gamma_2$, and because the teeth are in regular gear contact, θ_1 decreases and θ_2 increases while following the edge of the blockade until $\theta_2 \approx 0$ at III. Here, the snapthrough instability of twisterbuckler two is triggered, contact is lost, and the system snaps to configuration IV. While the twistbucklers are no longer in contact, further compression does not diverge the stable configuration of the system away from the $-\theta_1 = \theta_2 > 0$ diagonal.

As we start decompressing, the system traverses along the $-\theta_1 = \theta_2 > 0$ diagonal until contact is formed between the mesher teeth (Fig. 5.12cV). Now, because $\hat{\Gamma_1} \neq \hat{\Gamma_2}$, the teeth form a tip-flank contact. As this type of contact relies on sliding and the friction between the caps is not negligible, the teeth stick together for a while until at some critical strain $\varepsilon^{\downarrow} \approx 0.06$ the teeth make a flank-flank contact. The $-\theta_1 = \theta_2 > 0$ diagonal state that was stable at high ε is thus flipped to a $\theta_1 = \theta_2 > 0$ state at low ε , opposite to the starting configuration (Fig. 5.12cVI).

During the second compression cycle, we observe the same phenomenology, with the snapping directions reversed. We note that the two cycles differ slightly due to experimental imperfections. In particular, during the second decompression cycle, the formation of flank-flank contact appears more smooth than in the first cycle (Fig. 5.12de), and the snapping during compression occurs at different ε .

As we continue compressing and decompressing, we observe the same repeated behavior (Fig. 5.12d). Hence, a single compression cycle transitions the system from $\theta_1 = \theta_2 < 0$ to $\theta_1 = \theta_2 > 0$ (or vice versa), and a two cycles takes us back to the starting configuration. Thus, the system keeps track of the parity of the number of compression cycles; the state depends only on the initial starting configuration, and whether an odd or even number of compressive cycles have been applied.

Finally, by representing the state of the system with a single parameter $S = \arctan_2(\theta_2, \theta_1)$, the similarity of the parity machine to the ideal system shown in Fig. 5.1d becomes apparent as shown in Fig. 5.12e.

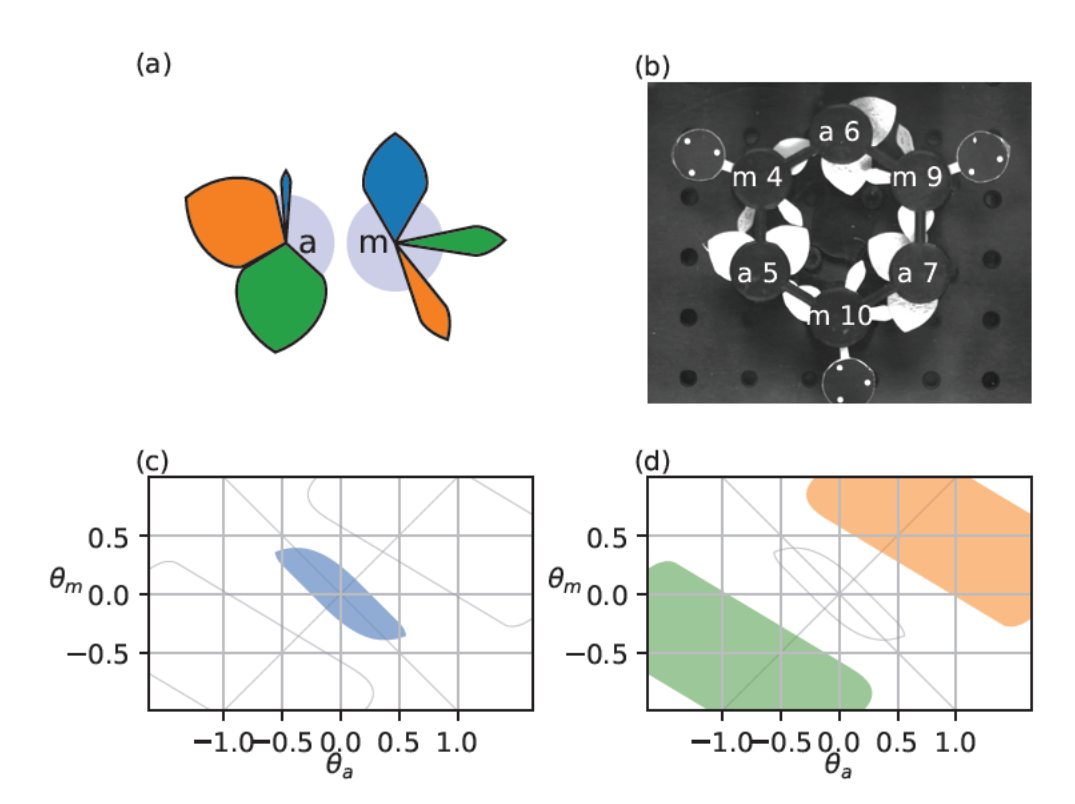


Figure 5.13: Design of the hexcycle. (a) The design of the two caps. (b) Spatial layout of the twitbucklers as built. (c) Blockade within a unit cell indicated in blue. (d) The composite blockade that determines the interaction between unit cells. The two colors correspond to the different layers of the flipper teeth. The gray outlines indicate the shape of the blockades that are not present in that interaction.

Thus we have successfully built a parity machine which successfully tracks the parity of the number of input compression cycles. This demonstrates the fundamental working principle of using contact interactions with twistbucklers to construct a mechanical metamaterial with memory. The parity machine features two irreversible transitions at each compression cycle; one transition during compression as twistbuckler two is flipped and the twistbucklers anti-align, and one during decompression as the mesher pair meshes together and the twistbucklers align.

5.5 Rule 15 and the Hexcycle Machine

We construct a machine with a longer multiperiodic response. Specifically we built a Hexcycle machine – a system that requires six compressive cycles to return to any one of its initial configurations.

Hexcycle Design

The hexcycle design uses the same base interactions as the general interactions as the parity machine, but instead of coupling to a single neighbor, the hexcycle uses six twistbucklers in a loop. Here the mesher and flipper teeth are oriented such that their interactions are either with their clockwise or anti-clockwise neighbour.

Specifically, we utilize two types of twistbuckler caps (Fig. 5.13a), and fix the positions all six twistbucklers along a regular hexagon with side lengths D using brackets (Fig. 5.13b). The teeth of the twistbucklers are similar to those used before, but they are now oriented such that the twistbucklers interacts with one neighbor through a mesher blockade, and the other neighbor through a flipper blockade. We will refer to the two different twistbucklers as an a-buckler and an m-buckler. An m-buckler (a-buckler) interacts with its clockwise neighbor through a mesher (flipper) blockade (Fig. 5.13d), and its anti-clockwise neighbor through a flipper (mesher) blockade (Fig. 5.13d). The Hexcycle uses the same mesher parameters as for the parity machine: $\Gamma_a^m/D = 0.296$, $\Gamma_m^m/D = 0.519$, $\alpha_a^m = 50^\circ$, $\alpha_m^m = 18^\circ$, $\beta_a^m = \beta_m^m = 0$. The parameters of the flipper teeth are slightly modified: $\Gamma_a^f/D = 0.295$, $\Gamma_m^f/D = 0.492$, $\alpha_a^f = 106^\circ$, $\alpha_m^f = 21^\circ$, $\beta_a^f = \pm 0.95$, $\beta_m^f = \pm 0.55$. These teeth result in blockades that are similar to those used before, but proved to be more robust in response to sample defects and unfavorable loading conditions.

As the variations in $|\theta_i|(\varepsilon)$ at higher ε are less ensitive to imperfections, we choose to design our flipper teeth such that they make contact at large ε . This comes at a trade off, as the maximal rotation of the twistbucklers is limited, and at high ε the twistbucklers become tristable. Moreover, the angle at which contact is formed, limits the range of κ . Specifically, in comparison to the parity machine, contact is made at a higher strain and at a κ closer to 1.

Due to the sensitivity of the system to imperfections and heterogeneous compression, we individually shimmed each twistbuckler such that their buckling strains are better aligned (See appendix C). For these experiments we chose the twistbuckler samples in the configuration indicated in Fig. 5.13b: in clockwise order: m4 & a6, m9 & a7 and m10 & a5.

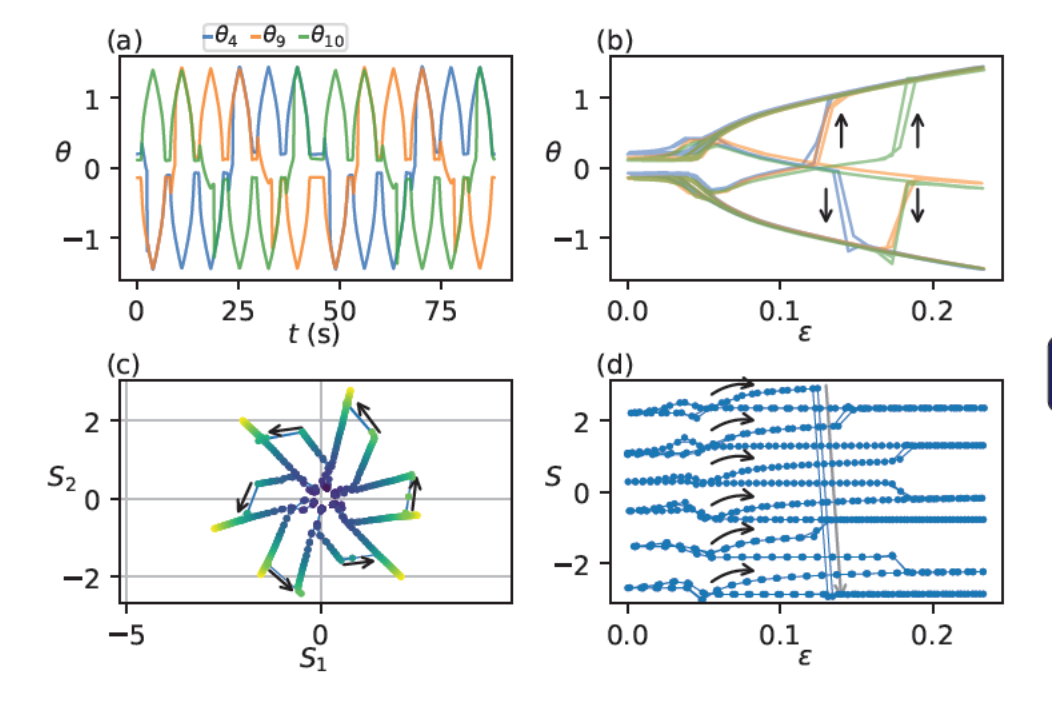


Figure 5.14: Design and working of the tricycle (a) The states of the m-bucklers as a function of time, over 12 compression cycles. (b) The states of the m-bucklers as a function of ε . (c) A sixfold representation of the state of the state of the system. The color represents the strain ε of each point. (d) The single field state representation of the system as a function of ε .

Hexcycle Results

We tracked the rotation of the m-bucklers as a function of driving θ , for 12 driving cycles (Fig. 5.14a). We observe that at each compression cycle, one of the three tracked twistbucklers is flipped. In order, we observe a flip of twistbuckler 4, then 9 and then 10. As the state of the system is binary, six compression cycles are required to return to the initial state; through which all stables resting states of the system are observed. When considering the pairwise interactions of twistbucklers, the phenomenological behaviour of the Hexcycle machine is similar to that of the parity machine. The Mesher pairs determine the stable states at $\varepsilon = 0$ and govern the irreversible transition at decreasing ε , and the flipper pairs govern the irreversible transitions at increasing ε . The distinction being, that the Hexcycle machine has a cellular design. Each cell has a state determined by the mesher pairs, and these cells interact through the flipper blockades. The Hexcycle system has three cells, each with two stable states at $\varepsilon = 0$. Starting in the state $|\vec{S}| = sgn(\theta_4, \theta_9, \theta_{10}) = (1, -1, 1)$, we follow the cycle: $(1,-1,1) \rightarrow (-1,-1,1) \rightarrow (-1,1,1) \rightarrow (-1,1,-1) \rightarrow (-1,1,1) \rightarrow (-1,1) \rightarrow (-1,1)$ $(1, 1, -1) \rightarrow (1, -1, -1) \rightarrow (1, -1, 1)$. Thus, at each compression cycle, if a cell is in the same configuration as its anti-clockwise neighbor, it gets flipped. Otherwise it stays in the same configuration.

To better illustrate the six-fold nature of the system states, we projected the state of the system from a triagonal basis onto two state axes: $S_1 = \theta_4 \cos(\pi/12) + \theta_{10} \cos(\pi$

The Hexcycle machine successfully demonstrates the working principle of the cellular strategy to increase the cycle length of twistbuckler systems. We achieved a system consisting of three cells (two twistbucklers each) that traverses through a cycle of six stable states through a pattern that matches rule 15 (and 85) of the elementary cellular automata with periodic boundary conditions [88]. At every compression cycle, every cell that is in the same configuration as its anti-clockwise neighbor is flipped. This behavior is, in principle, scalable to arbitrary even length cycles, or arbitrary length transient responses when the cells are not connected in a loop.

However, the system operates near the edge of what is experimentally possible using the current samples and manufacturing accuracy. The strains at which the twistbucklers snaps is scattered, with some snaps occurring during decompression rather than compression. We note that the variation in time seems to be smaller than the variation between individual samples, indicating that here the viscous properties of the rubber are not the leading factor in the variations. The system is highly sensitive to defects and manufacturing errors and it required individual shims for each twistbuckler to better align their buckling strains.

5.6 Conclusion and Outlook

In this chapter, we showed a novel platform that allows for controllable interactions between neighboring bistable elements, and the creation of arbitrarily long multiperiodic pathways. We unstable buckling elements that twist under compression and couple through rigid contacts. We demonstrated the emergence of bistability in these twistbucklers and demonstrated how the blocked configuration space, due to the contacts lead to an elegant method of achieving asymmetric bifurcations. We demonstrated systems of twistbucklers that have a cyclic response to driving length two and six, and argue that arbitrary even lengths are possible in longer systems.

The framework discussed in this chapter is very promising and there are a number of possible further developments for this platform that we will discuss here.

First, the development of other simple cellular automata. Currently the flipping interactions use regular gear contact and thus anti-align when flipping. The use of Mercier-contacts could be used to align twistbucklers when flipping. This would allow for the creation of rule 252; the system equivalent of the beam counter [88] (chapter 2). Such interactions would potentially benefit from the use of stacked blockades forming helical teeth. Using these, the Mercier regime can be increased in size without increasing the regular gear regime.

Second, the development of a "Turing complete" cellular automata. Thus far only cellular automata that consider the state of one neighbor have been developed. A different system topology that interacts to both neighbors could allow for more complex interactions, such as the development of a system that mimics the rule 110 automaton which is known to be Turing complete at infinite systems sizes [106]. This would require at least three twistbucklers in contact at one point in time.

Third, increasing the robustness of the system, by improving the manufacturing of the samples and improving the accuracy of the setup. Further development of the twist-buckler geometry could improve the bi-stable regime of the twistbucklers. Currently, the system relies on what we could consider geometric defects. Differences in the teeth result in the determinism and breaking of the interaction symmetry (Fig. 5.1ab). This asymmetry however is not completely local. Breaking symmetry in part of the sys-

tems trajectory can inadvertently cause a problem in another part. This results in limits of how 'far' symmetry can be broken and thus the robustness of the system. An ideal system would be able to affect specific parts of the system trajectory without interfering in other parts. One method to achieve this might be to use topological defects instead of geometric defects [107], such as through using coupled 4-bar linkages which have been successfully used in the development of other mechanical computing systems [108]. Finally, the memory properties of heterogeneous parallel cyclic systems could be explored. As discussed in chapter 2, using multiple heterogeneous transient systems in parallel allows us to extract specific information from past driving cycles. The addition of detecting repeated cycles could greatly improve the ability of these systems to infer information about repeated cycles and long cycles of inputs. Multiple cyclic counters of pairwise co-prime cycle length for example, would be able to count sequence lengths much larger than their own length; a result of the Chinese remainder theorem [109].

Appendix A

Counting Beams Details

Sample Fabrication, Setup, Protocol, Design

Samples are made by pouring degassed and refrigerated Zhermack Double Elite 32 VPS mixture into open face molds that are 3D printed on UltiMaker S3 and S5 printers. The samples are cured at room temperature. After curing, the samples are removed by breaking the molds. The slits in the s-beams are cut using a scalpel after which the samples are covered with talcum powder to reduce stiction. Before measurements the samples are allowed to rest for a week to allow their mechanical properties to settle.

The measurements are performed with a setup consisting of a homebuilt single-axis compression setup, where the samples are compressed between two plates, one static and one driven by a linear translation stage. The plates remain parallel within a slope of < 0.6 mm/m and move at a rate of < 0.1 mm/s with an accuracy of $\pm 0.01 \text{mm}$. A ccd camera captures images at a rate of 60Hz.

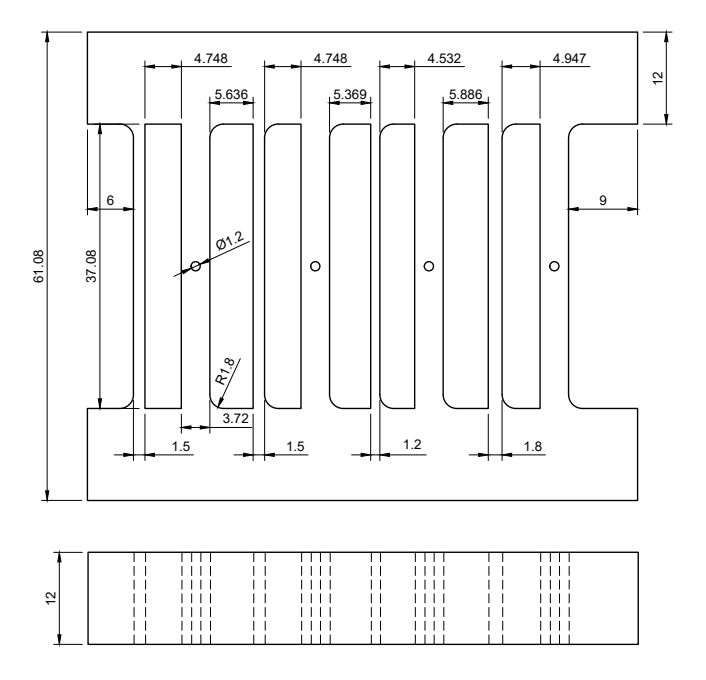


Figure A.1: Geometry of the *bac* counter (distances in mm).

Robustness and Alternative Design

To demonstrate that our design for homogeneous counters is robust, we produced scaled down versions that we place in a simple hand-held device (see Fig. A.2). The device consists of a 3D printed flexure which guarantees a finite compression ε_m , and reasonably accurate parallel top and bottom plates. After setting the initial state to $\{1000\}$, repeated manual compression advances this counter towards its absorbing state $\{1111\}$.

To demonstrate that beam counting can be realized in a wide variety of designs,



Figure A.2: A hand-operated flexure based device (dark green) containing a smaller n=4 beam counter illustrates the robustness of our design.

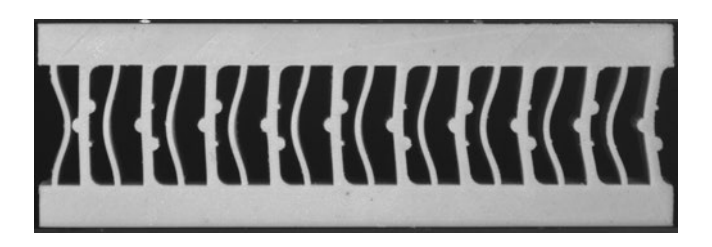


Figure A.3: Alternative design for beam counting using symmetry broken beams.

we have explored an alternative design where the s-beams do not feature slits (see Fig. A.3). Here, the symmetry breaking for counting is realized by pre-curvature of the m-beams, and the addition of symmetry breaking bumps on the 's-beams'. The latter control the higher order buckling modes of the m-beams and guides their movement under cyclic compression.

Design parameters

All sample geometries have L=37.1 mm, T=3.7 mm, and a fixed radius of curvature of the symmetry breaking bases of R=1.80 mm (Fig. A.1). We fix T and vary t_i , d_i and D_i to modify ε^{\dagger} (Table. A.1). We measured ε^{\dagger} by determining the rightward snapping of the relevant beams from the difference in subsequent images for each unit cell in our aaa, bbb, ccc and bac samples (Table. A.2). We note that there is scatter in the values of ε^{\dagger} , and in particular that in the homogenous samples (aaa, bbb and ccc), ε^{\dagger}_1 is lower than ε^{\dagger}_2 and ε^{\dagger}_3 . We believe this to be due to the right-ward symmetry breaking of the left (0-th) m-beam in these samples. Not withstanding the scatter, our driving amplitudes bracket all the measured values for ε^{\dagger}_a , ε^{\dagger}_b and ε^{\dagger}_c .

Table A.1: Dimensions of homogeneous and heterogeneous samples

Parameter	Dimension (mm) ± 0.05 (mm)
m-beam thickness $t[a]$	1.2
m-beam thickness $t[b]$	1.5
m-beam thickness $t[c]$	1.8
Beam length L	37.1
m -beam \rightarrow s-beam distance $d[a, \ldots]$	7.6
m -beam \rightarrow s-beam distance $d[b, \ldots]$	7.9
m -beam \rightarrow s-beam distance $d[c, \ldots]$	8.2
s-beam \rightarrow m-beam distance $D[\ldots, a]$	8.9
s-beam \rightarrow m-beam distance $D[\dots, b]$	9.4
s-beam \rightarrow m-beam distance $D[\ldots,c]$	9.8
Radius of slit-ending hole	0.6
Radius of rounded corners R	1.8

Table A.2: Sample design and thresholds ε^{\dagger} .

Sample	$t_1 \pm $	$5 \times 10^{-4} \ (-)$	t ₂ ±5	$\times 10^{-4} (-)$	$t_3 \pm 5 \times 1$	$10^{-4} (-)$	$t_4 \pm 5 \times 10^{-4} \ (-)$
aaa		0.032	0	.032	0.0	32	0.032
bbb		0.040	0	.040	0.0	40	0.040
ccc		0.049	0	.049	0.0	49	0.049
bac		0.040	0	.040	0.032		0.049
Sa	mple	$\varepsilon_1^{\dagger} \pm 0.5 \times 1$		$\varepsilon_2^{\dagger} \pm 0.5 \times$			$\times 10^{-3} (-)$
	aaa	6.96×1	0^{-2}	7.58 ×	10^{-2}	7.71	$\times 10^{-2}$
	bbb	8.17×10^{-1}	0^{-2}	8.47 ×	10^{-2}	8.76	$\times 10^{-2}$
	ccc	9.28×10^{-1}	0^{-2}	9.44 ×	10^{-2}	9.30	$\times 10^{-2}$
	bac	7.85×10^{-1}	0^{-2}	7.58 ×	10^{-2}	9.03	$\times 10^{-2}$

Details of bit-copy operation

Here we discuss in more detail the right copying of a '1' bit, as shown in Fig. 3 of the main paper — see also movie 4. During this process, the rightward buckled state of m₁ is copied to s₁, and subsequently, the rightward buckled state of s₁ is copied to m₂. A detailed inspection of this dynamics further illustrates our design choices. (i) First, upon increasing the compression from the initial state at ε_m (main Fig. 3aI), beam m_1 makes contact with the interaction beam s_1 before m_2 : this is guaranteed by our choice of spacings d < D, and by s_1 buckling left due the rounded corners at its ends (main Fig. 3aII). Increased compression beyond the critical strain ε^{\dagger} results in the rightward snapping of s_1 — this is why we take $d < D^*$ (see main Fig. 1c). (ii) After s_1 has snapped, m_2 is sandwiched between s_1 and s_2 , and takes on a complex shape (main Fig. 3aIII). Further compression does not lead to significant evolution. In this state, s₁ has a much larger deflection to the right than s₂ has to the left due to the presence of the slit, thus overcoming the difference between D and d. This pushes m₂ to the right, and when the strain is lowered, m₂ loses contact with s₁ and leans to the right (main Fig. 3aIV). We stress that the slits in the s-beams are crucial, as they enhance the rightward motion of s₁ — without slits, the s-beams would push m₂ to the left as d < D (see main Fig. 3b). Upon further lowering of the strain to ε_m , the m-beam reaches a purely rightward buckled configuration and the system reaches state $\{11\}$ (main Fig. 3aV). We have verified that all other initial conditions ($\{00\}$, {01}, {11}) remain invariant under the same cyclic driving — as seen in main Fig. 1c. Hence, a judicious choice of geometry allows our unit cells to perform the irreversible rightwards advancing of 1-bits.

Table A.3: Examples of aggregate metamaterials consisting of two heterogeneous counters that reach a unique state for a given input string (key) of length two.

key	metamaterial	unique state
AA	ba	[2]
AB	ac ba	[1 1]
AC	ac ba	[0 1]
BB	bb ca	[0 2]
BC	ba ca	[0 1]
CA	ab ca	[1 0]
CB	ac cb	[1 0]
CC	cc	[0]

Heterogeneous machines

In the main text we presented a general strategy to uniquely detect an input string of length $l_s = 3$, featuring m = 3 characters, using m homogeneous counters of length $l_s + 1(+2)$ and one heterogeneous counter of length $l_s + 1$. This strategy can be extended to recognize strings of arbitrary length, where m homogeneous counters determine the multiplicity of each symbol, and a single heterogeneous counter uniquely reaches zero when its input matches its design.

However, often one can uniquely detect a given string with a aggregate metematerial that features more than one heterogeneous counters. To demonstrate this we performed an exhaustive search of the combinations of heterogeneous counters that uniquely detect input strings of length l_s two and three, using m=3 characters, $\{A,B,C\}$. For every target string we found a combination of q counters, with $q \leq l_s$ (Tables A.3-A.4). We note that some metamaterials can simplified even further, e.g., to detect AA the metamaterial aa|b suffices.

Transitions in complex aggregate metamaterials

To illustrate the complexity of metamaterials featuring multiple heterogeneous counters, we show the transition graph for the aggregate metamaterial aba|baa|caa, starting out at state $\{3,3,3\}$ (Fig. A.4). Clearly, the state that is reached encodes information on the driving sequence. First, restricting ourselves to input strings of length three, there are eight states that encode a unique driving sequence: $\{1,0,2\},\{1,2,2\},\{0,0,2\},\{1,2,3\},\{1,0,3\},\{2,3,3\},\{0,1,2\},\{2,0,0\}$ and $\{2,0,3\}$ —as can be readily verified from Fig. A.4, each of these is only reached in response to a unique three-character input sequence. Second, taking input strings of arbitrary

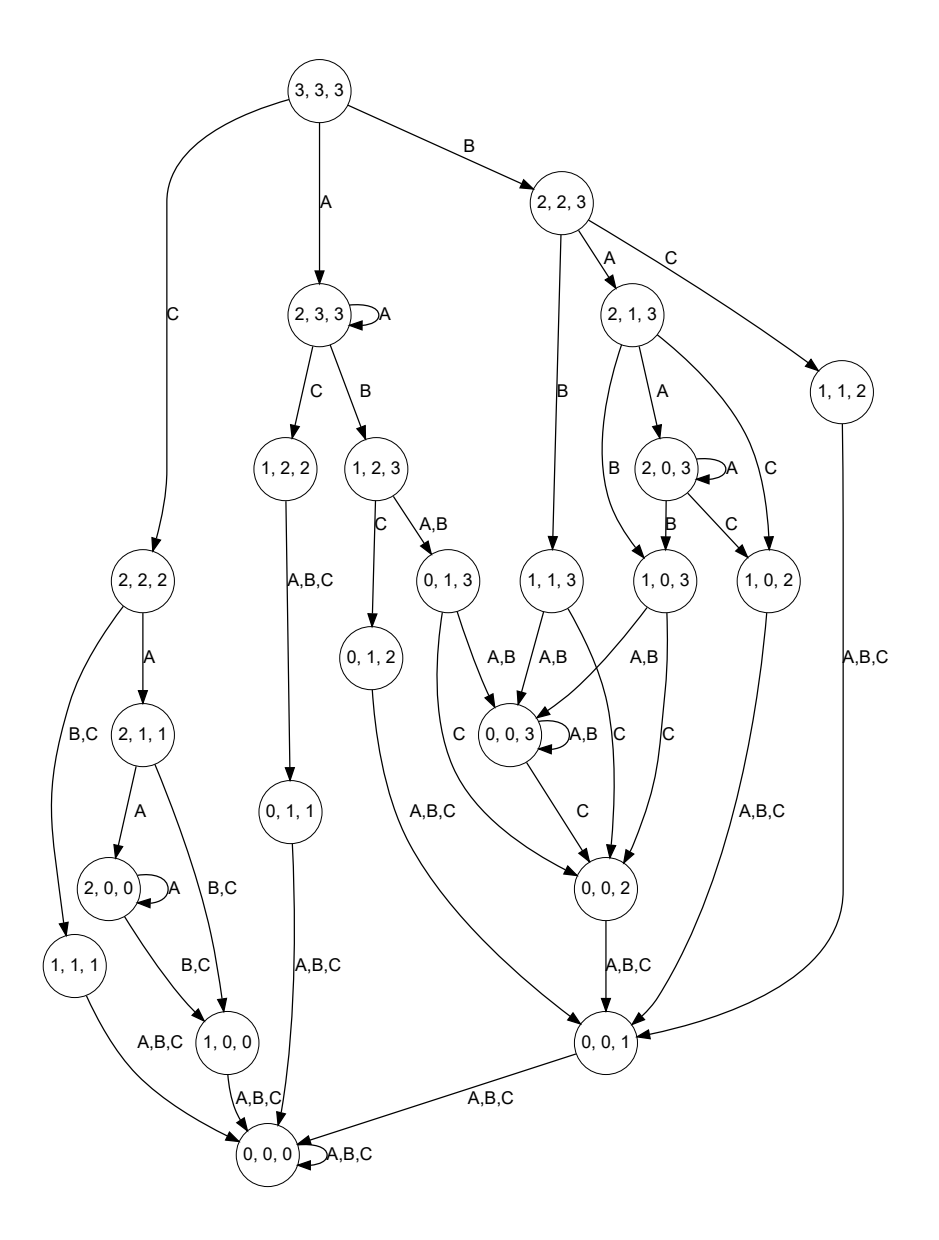


Figure A.4: The full transition-graph for the aggregate metamaterial aba|baa|caa (labels are always to the right of the transition arrow).

length into account, a different set of seven states is associated with a unique input sequence: $\{3,3,3\},\{2,1,1\},\{2,2,3\},\{1,1,2\},\{1,1,3\},\{2,1,3\}$ and $\{2,2,2\}$.

Table A.4: Examples of aggregate metamaterials consisting of two heterogeneous counters that reach a unique state for a given

input st	input string (key) of length three.	gth three.))			
key	key metamaterial	unique state	key	metamaterial	unique state	key	metamaterial	unique state
AAA	baa	[2]	AAB	aac baa	[1 2]	AAC	aac baa	[0 2]
ABA	aab aca baa	[121]	ABB	aab aca baa	$[0\ 2\ 1]$	ABC	aca baa	[1 1]
ACA	aaa aca bba	$[0\ 0\ 2]$	ACB	aaa acb bca	$[0\ 0\ 2]$	ACC	aca bca	$[0\ 1]$
BAA	aba baa caa	$[2\ 0\ 3]$	BAB	aba baa caa	$[1\ 0\ 3]$	BAC	aba baa caa	$[1\ 0\ 2]$
BBA	aab bba caa	$[1\ 0\ 3]$	BBB	bbb caa	[03]	BBC	bba caa	$[0\ 2]$
BCA	bca cba	$[0\ 2]$	BCB	bcb cca	$[0\ 2]$	BCC	bac caa	$[0\ 1]$
CAA	aba caa	[2 0]	CAB	aba cac	[11]	CAC	aba cac	$[1\ 0]$
CBA	aab aca cba	$[1\ 2\ 0]$	CBB	aca cbb	$[2\ 0]$	CBC	aca cba	$[1\ 0]$
CCA	aab cca	$[1\ 0]$	CCB	aac ccb	$[1\ 0]$	CCC	222	[0]

Appendix B

Bellini Truss

A compressible beam can be modelled by a collection of compressive trusses serially linked by torsional springs, as shown by Guerra et.al. [75]. For small angles θ_j we can write the potential of such a beam as (Fig. B.1):

$$U = \frac{1}{2}k\sum_{i}^{N}u_{i}^{2} + \frac{1}{2}b\sum_{j}^{N+1}\theta_{j}^{2},$$
 (B.1)

where u_i is the compression of each spring and θ_j the change in angle from the resting configuration. The spring constants k and b are chosen to match the compressive stiffness and bending stiffness of beams with a rectangular cross section, so that $k \propto t$ and $b \propto t^3$.

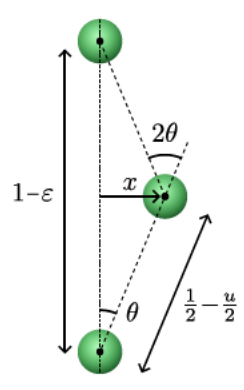


Figure B.1: The geometry of the top-down symmetric Bellini truss.

A Bellini truss corresponds to the N=2 case. Under imposed top-down symmetry $(u_1=u_2 \text{ and } \theta_2=2\theta_1=2\theta_3)$ the summation can be performed to obtain:

$$U = Ktu^2 + Bt^3\theta^2, (B.2)$$

where we absorbed the summation over the number of springs into the coefficients K and B.

To express the potential in x and ε , we express $u=1-\sqrt{x^2+\left(\frac{1}{2}-\frac{\varepsilon}{2}\right)^2}$, $\theta=\arctan\frac{2x}{1-\varepsilon}$ to obtain:

$$U = Kt \left(1 - \sqrt{x^2 + \left(\frac{1}{2} - \frac{\varepsilon}{2}\right)^2} \right)^2 + Bt^3 \left(\arctan \frac{2x}{1 - \varepsilon} \right)^2.$$
 (B.3)

Instead of attempting to minimize the full energy Eq. (B.3), we expand it to fourth order in x and first order in ε around $(x, \varepsilon) = (0, 0)$, and obtain:

$$U \approx (Kt - \frac{32Bt^3}{3})x^4 + (4Bt^3 + 8Bt^3\varepsilon - Kt\varepsilon)x^2,$$
 (B.4)

As x, ε , and t are all small, we discard the highest order terms $\mathcal{O}(t^3x^4)$ and $\mathcal{O}(t\varepsilon x^2)$, and obtain the leading order potential:

$$U \approx Ktx^4 + (4Bt^2 - K\varepsilon)tx^2.$$
 (B.5)

This potential transitions from a monostable to a bistable form when the x^2 term switches sign at $\varepsilon = \frac{4B}{K}$. Diving by K produces the rescaled potential that makes this transition explicit:

$$U = tx^4 + (\xi t^2 - \varepsilon)tx^2, \tag{B.6}$$

where the transition from a monostable to bistable potential occurs at $\varepsilon = \xi t^2$.

Appendix C

Twistbuckler Details

Tracking images

To determine the configurations of the twistbucklers from the images, we track the fiducials movement using Trackmate [110]. Trackmate tracks markers, by first finding all markers in each frame and subsequently linking these frames together by solving the linear assignment problem with a cost-function that minimizes the movement of the dots between frames [110]. We then calculate the rotation of each frame, by fitting the affine transformation matrix that best matches the movement between the target and reference image using scikit-image [111]. This allows us to calculate the rotation θ of the fiducial and therefore the cap of each twistbuckler with respect to a reference frame.

Circle Involute Curve Construction

The involute of a circle, otherwise known as the anti-clothoid, and often referred to as the evolute, is a curve that is defined by the involute [112]. An involute of a plane curve is defined by the curve that is formed by tracing the end of a taut wire, as it is wound around the plane curve. It is the curve for which all normals are tangent to the base circle. Thus, each point can be constructed geometrically. For a circle of radius b, every line of length t that is tangent to the base circle, touches an involute curve at an angle that is normal to that curve. This curve is rooted at the cusp, the point at which opposite handed evolutes meet, at an angle of $\alpha = \frac{t}{2\pi}$ (Fig. C.2a). All equal

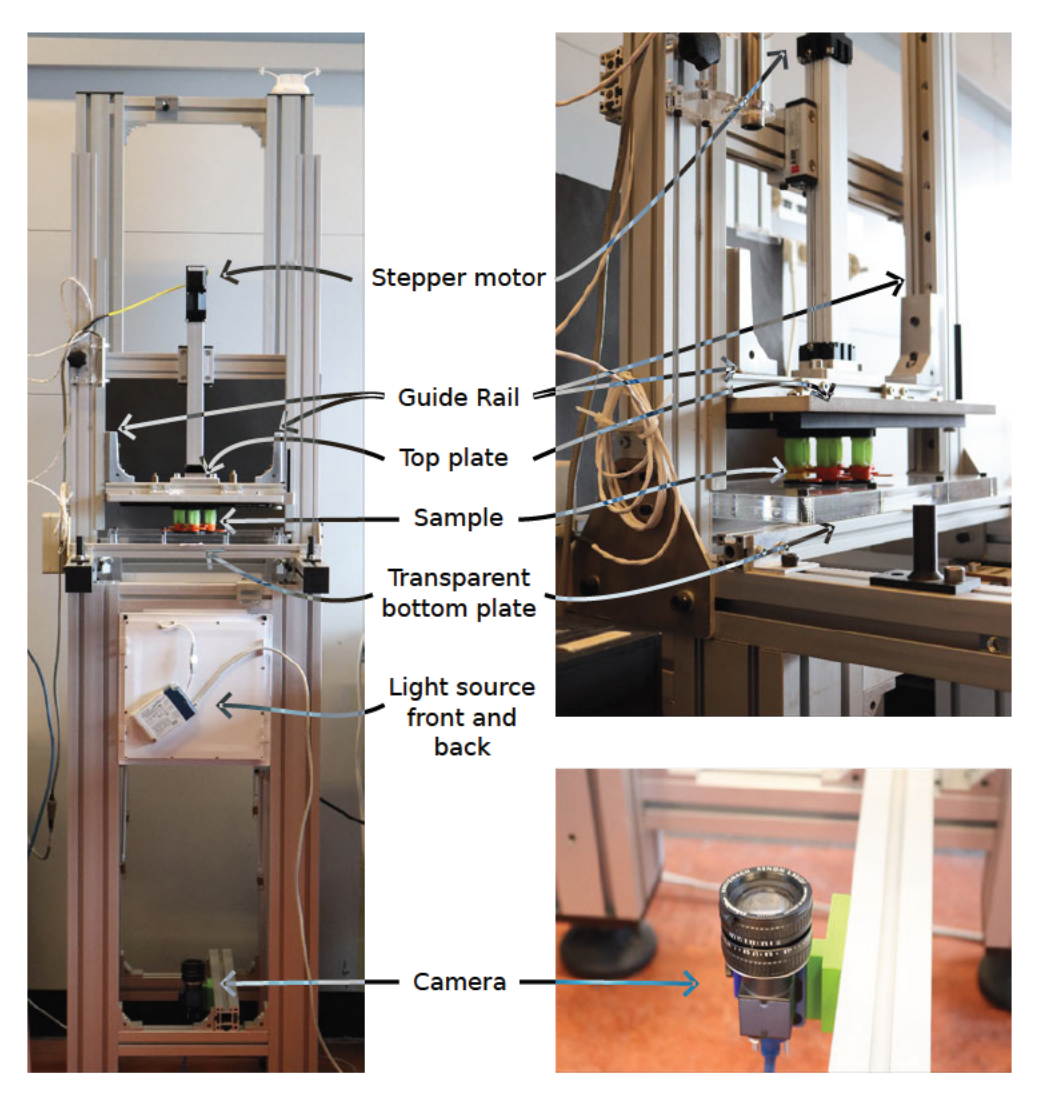


Figure C.1: The Crushinator setup with the acrylic transparent bottom plate used for the camera tracking of Twistbuckler experiments.

handed involute curves constructed from a circle are parallel (Fig. C.2b). The image that is formed by rotating a circular involute by an angle α around the center of the base circle, is at a distance of αb along the entire curve. Therefore it is also parallel to an opposite handed evolute at a distance $2\pi b$ (Fig. C.2c)[112], and an equal handed evolute at a distance $2\sqrt{\pi^2 + b^2}$ (Fig. C.2d). These properties allow us to construct a projection of two dimensional space onto rotation angles of auto-parallel evolutes [112].

Deriving Blockade Shapes

The involute can be parameterized with the following equation:

$$z = b \cdot (1 - it)e^{it},\tag{C.1}$$

where b is the radius of the base circle, and t is the length of unwrapped string length.

When we define the curve to start at a specific angle α with respect to the real axis, we can reach any point outside of the base circle:

$$z = b \cdot (1 - it)e^{i(\alpha + t)}, \tag{C.2}$$

The cusp of the curve occurs at t=0. For t>0, this corresponds to a right-handed curve, and when t<0 the curve is left-handed. This mapping can be inverted such that any point in space z to an angle α and unwrapping t, or equivalently a distance to the center r.

As discussed in the main text, contact between involute teeth occurs along straight lines tangent to the curves base circles, or circular arcs perpendicular to the origin of one of the base circles. To transform this real-space contact shape, we transform each point using the inverse of Eq. C.2.

Performing these transformations, we have to account for the offsets of the starting angle of the specific surfaces that are in contact.

To find the domain of inaccessible angles in phase space θ_1, θ_2 , we have to transform the real space coordinate space to phase space, taking into account the resting angles of the flanks of both teeth. Teeth are defined by two flanks, and either: an implied maximal radius at the flank's intersection, or an explicit maximal radius when the caps are terminated in a circular arc. This is computed in the aforementioned program for the different sections.

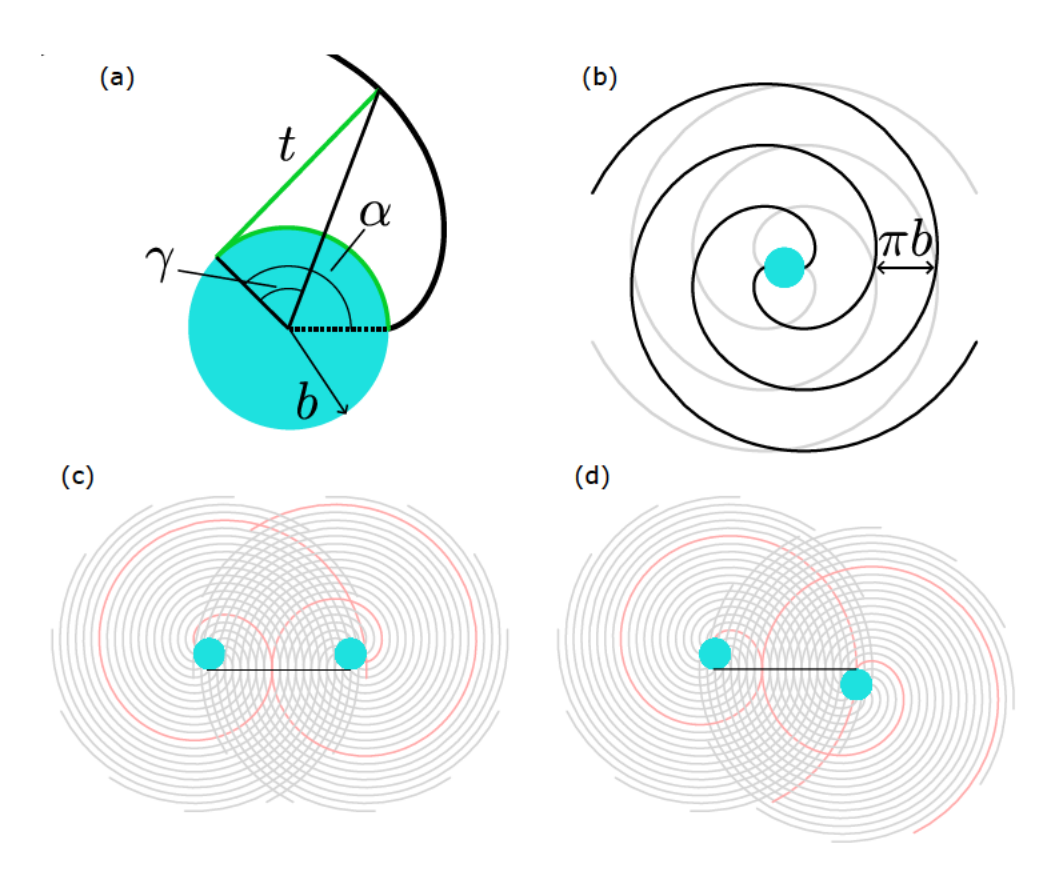


Figure C.2: Construction of an involute curve. (a) Involute curve unwrapped from a circle of radius b. Every point along the curve can be constructed with a right-angled triangle. The length t indicated in green is tangent to the base circle and of equal length as the arc defined by θ and the base radius b. Thus the length of t is αb . The internal angle γ is trivially related: $\tan \gamma = \alpha$. (b) Involutes of a circle are parallel to each other. (c) Involutes are auto-parallel. At a distance of $2\pi b$, all points of contact occur on a line (the Mercier contact line [101]) indicated in black. (d) Similarly for regular gear contact, all contact occurs along a line that crosses the mid-line between both circles.

Contacts lines along: τt , $\tau \ell$, $t \ell$, $\ell \ell$, ℓt , $\ell \tau$, $t \tau$, $\tau \tau$, and the two specific tip-tip points: $t t^+$, $t t^-$.

Qualitatively, the normal-gear tooth flanks ($\tau\tau$ and $\ell\ell$) are longer edges with negative slope in phase space. These edges exist as long as $|D| < |R_1| + |R_2|$ The Mercier edges ($\tau\ell$ and $\ell\tau$) are always shorter than normal contact edges, and possibly do not occur.

By making the teeth of contact helical (facing down or up), the blocked domain in space can be increased. This is equivalent to having multiple teeth on different layers.

Criterion for different types of contact

We can geometrically work out the requirements for the various types of contact to occur.

Having any form of contact between teeth trivially requires:

$$D < \hat{\Gamma_1} + \hat{\Gamma_2}. \tag{C.3}$$

To further determine the type of contact that is formed, we can geometrically construct the contact space and determine the conditions for each type of contact.

Flank contact occurs along straight lines tangent to both base circles with radii Γ_1 , Γ_2 . Ordinary gear contact occurs on the intersecting lines and Mercier contact occurs along the non-intersecting lines. These lines correspond to potential contact spaces, whether contact occurs is determined by the finite size of the teeth. To determine the criteria of contact, we construct the intersection of these potential contact spaces with the lens that is formed by intersecting the outer circles with radii $\hat{\Gamma_1}$ and $\hat{\Gamma_2}$.

As the ordinary contact space crosses the line that connects the centers of rotation of both teeth, any contact will immediately correspond to ordinary gear contact. The existence of Mercier contact is more complicated. Mercier contact only occurs when the rl and lr lines cross through the lens. We can geometrically construct the criterion:

$$\Gamma_1 + \frac{\Gamma_2 - \Gamma_1}{D} \cdot D_1 > \sqrt{\hat{\Gamma_1}^2 - D_1^2} ,$$
 (C.4)

where

$$D_1 = \frac{\hat{\Gamma_1}^2 - \hat{\Gamma_2}^2 + D^2}{2D} \ . \tag{C.5}$$

When Mercier contact can occur, there can be no tip-tip contact and vice versa.

Symmetric

For the symmetric case when $\Gamma_1 = \Gamma_2$, the existence of the Mercier regime corresponds to the following inequality:

 $D \ge \sqrt{\hat{\Gamma}^2 - \Gamma^2} \ . \tag{C.6}$

Thus, the minimal distance D_{min} occurs when $D_{min} = \sqrt{\hat{\Gamma}^2 - \Gamma^2}$. Scaling up $D \to \phi D$, is equivalent to scaling up both $\hat{\Gamma} \to \phi \hat{\Gamma}$ and $\Gamma \to \phi \Gamma$, whereas scaling up $\alpha \to \phi \alpha$ increases $\hat{\Gamma}/\Gamma \to \phi \hat{\Gamma}/\Gamma$ for $\hat{\Gamma}/\Gamma >> 1$. Expanding to first order $\sqrt{\hat{\Gamma}/\Gamma^2 - 1}$ near $\hat{\Gamma}/\Gamma = 1$, we get $\sqrt{2}\sqrt{\hat{\Gamma}/\Gamma}$. Thus, assuming $\hat{\Gamma}/\Gamma > 1$, and that the regime grows linearly with $\sqrt{\hat{\Gamma}^2 - \Gamma^2}$, we expect a $\sqrt{2}$ increase of the Mercier regime when scaling up in α as opposed to scaling up the dimensions ($\hat{\Gamma}^2$ and Γ) of both teeth.

Cap design

The interaction between the twistbucklers is mediated through rigid contact interfaces. The shape of the contact is determined by rigid 'caps' that are pressed in to the twistbuckler shells (replaceable/adjustable). The contact surfaces are circularly involute in the plane perpendicular to the rotation axis.

In the main paper, we discussed the creation of blockades due to pairs of teeth. We also discussed the creation of composite blockades by combining teeth from multiple layers. This combination would allow us to create a wide array of possible composite blockades.

Here we offer the interested reader some insight into the achievable functionality obtained by blockades. Although the form of the blockades can vary wildly in function, there is only a finite number of observable phenomenological behaviors, both due to the deterministic behavior of system and due the physical limitations imposed by the shells. First, the actual twistbucklers have a limited amount of twist before the twistbucklers lock up. At large enough driving the snapping angle will become observably hysteretic as the higher order deformation modes of the twister come at play. At some large enough driving, the twistbucklers will not be able to snap until they are forced well past $\theta = 0$. Second, the (visco)plasticity of the twister material will skew the stable resting configuration of the twistbucklers away from the ideal. The twistbucklers preferentially buckle in the 'previous' (depending on the

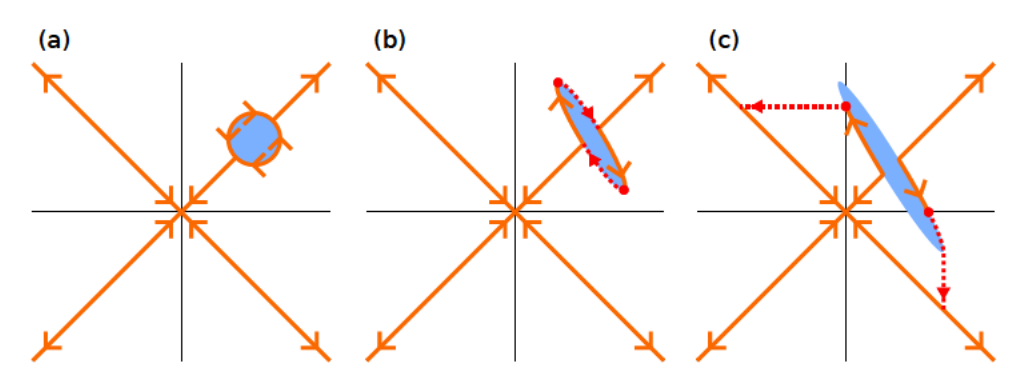


Figure C.3: Blockades splits stable state of system. As a blockade is stretched, snaps along the surface will occur. When a blockade crosses from the stable to the unstable path of the twister element, a snap to an other state occurs. (a) A symmetric blockade leading to either left-handed or richthandel traversal around the blockade. This corresponds to two pitchfork bifurcations opening and closing. (b) An asymmetric blockade resulting in two broken pitchfork bifurcations leading to two snaps. (c) A blockade that causes the stable state of the system to reach a saddle point of one of the stable elements.

magnitude of recent events) twisting direction. But also due to the limitations in the caps. Both due to friction, as near the critical points of the twisting shell potential, the normal force between contacts becomes large with respect to the force induced by the shells. As well as due the manufacturing errors of the caps that influence the shape of the blockades strongly. Thus, all interaction through blockades needs to occur close enough the origin $\theta_i = 0 \forall i$ to induce a snap-through, but the blockades must also be big enough so that the contact is formed by design.

We will group the functions of the blockades into two: "meshing" which determines the stable state as ε decreases, and "flipping" which determines the stable state on increasing ε .

Hexcycle Details

Shimming individual Twistbucklers

Using PLA shims of 0.06 mm \pm 0.01 mm thickness, we corrected for some of the heterogeneity in the buckling strain. We a second set of caps with markers on all caps, such that we could record the free buckling branch of all six twistbucklers in parallel. We set up a compression cycle where we labelead all twistbucklers fixed

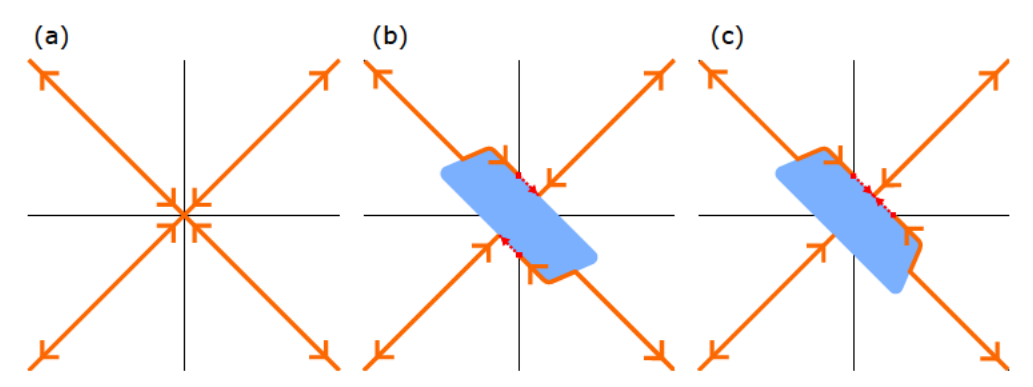


Figure C.4: Meshing blockade variants. (a) When decompressing into a blockade, the teeth mesh together. Asymmetries in the teeth determine the observed final configuration. (b)Apart from symmetry these are the three types of meshing rules we can observe. The dots indicate a "snap". Rotating the diagrams by $\pi/4$, or mirroring along a vertical or horizontal axes provides the other diagrams. From left to right: non-meshing (·1), chiral (·4), preferential (·4). Pictured here are the aligning ("ferromagnetic") meshing effects that result in a stable state in the ++ or -- quadrant.

them in individual locations in the compression machine. We measured the rotation response as a function of driving, and by intersecting the strain at $|\theta| = 0.5$ rad, we found values that we used to correct for the heterogeneity. We chose to adjust for the rotation near 0.5 rad, as this approximates the angle at which the twistbucklers make contact in the systems used.

After applying the shims to all twistbucklers, we found a reduction in the standard deviation from 0.13 mm to 0.05 mm at 0.5 rad (Fig. C.6). As the assembled height of the caps varies by the same order of magnitude, and we can't track the angles of all measurement caps, we measured the height both the measurement caps used here, and the caps used in the Hexcycle experiments, and matched these to accommodate further differences.

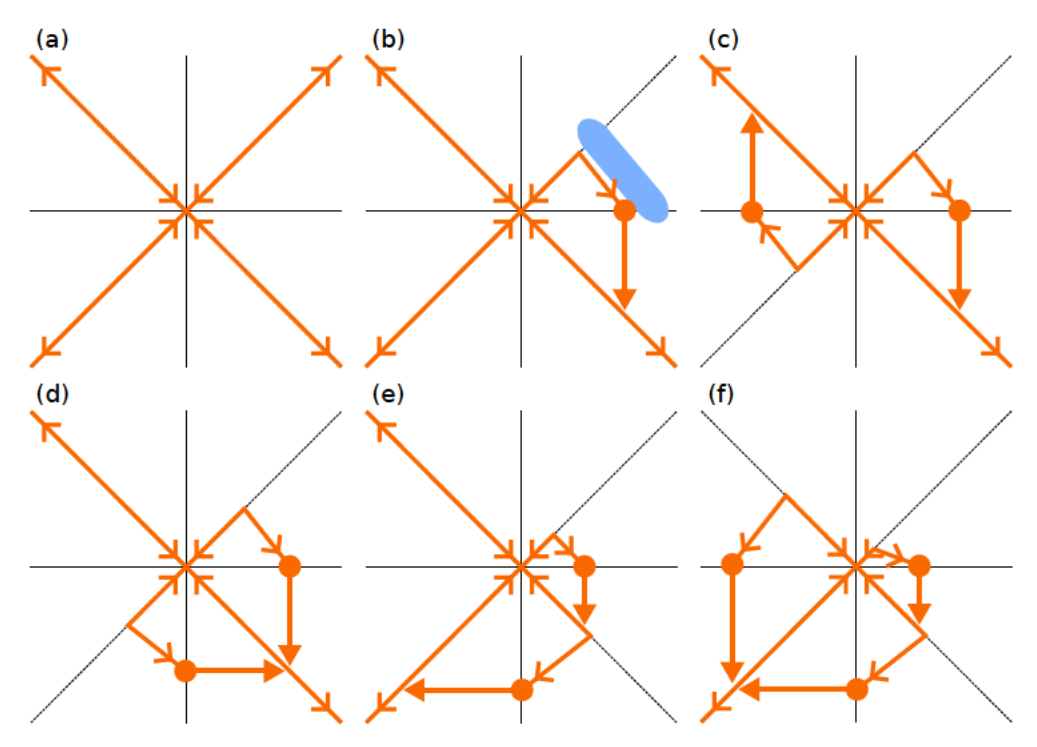


Figure C.5: Various identified hypothetical flipper blockade phenomenologies that arise from the interactions of multiple teeth pairs. Apart from symmetry $(\cdot n)$, these are the 6 identifiable ways of flipping. From left to right and top to bottom: (a) The no flipping blockade $(\cdot 1 \text{ variant})$. (b) The single flip blockade $(\cdot 8 \text{ variants})$. A blockade is illustrated, and the trajectory followed is indicated with the orange arrows. Dots represent unstable states at which point one of the twistbucklers snaps. (c) A chiral flipper blockade $(\cdot 4)$ in which the state of one twistbuckler is always copied to the other twistbuckler. (d) A biased blockade $(\cdot 4)$. (e) A two-step blockade $(\cdot 8)$, (f) A converging blockade $(\cdot 8)$ in which each state can be brought to a single identifiable state.

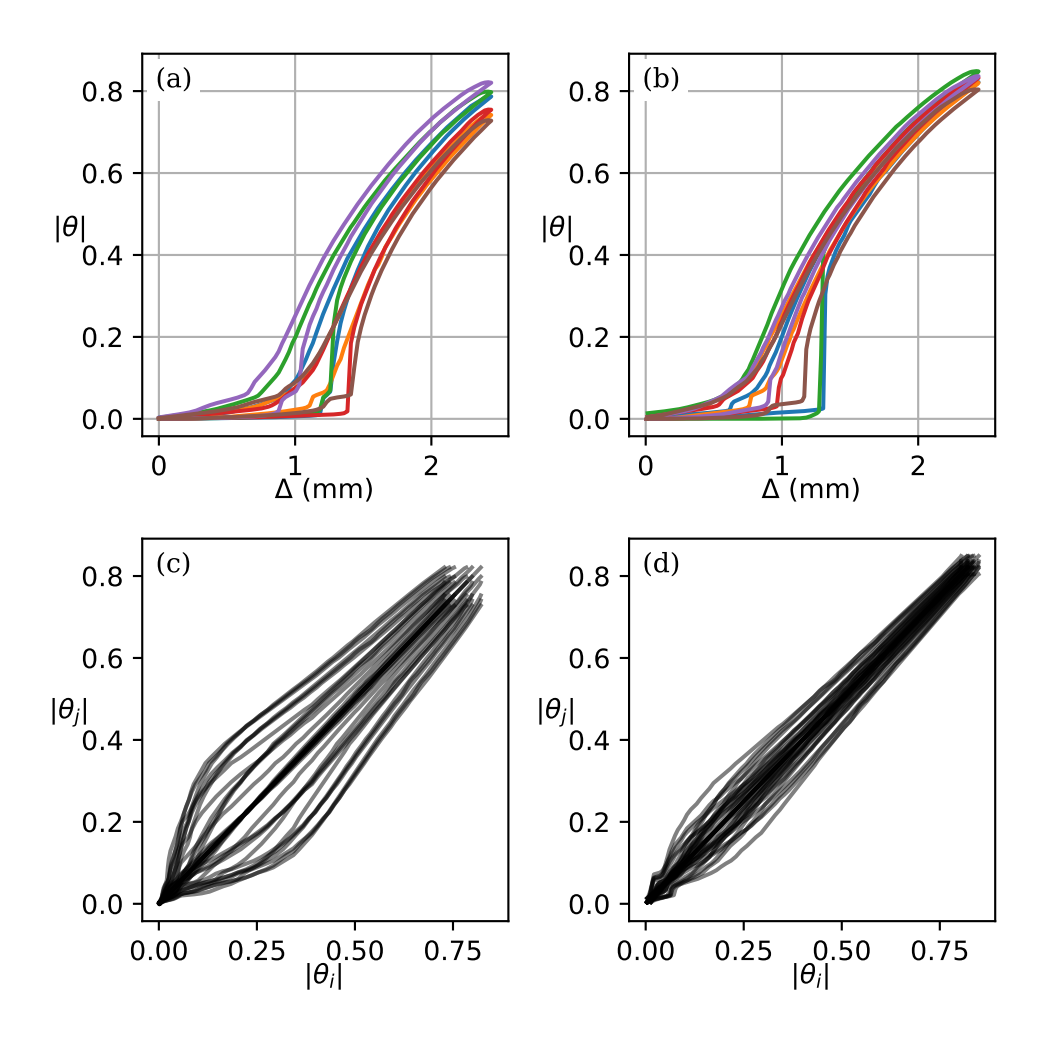


Figure C.6: Before (a) and after (b) correcting for the variation in buckling strains of the individual twistbucklers for the Hexcycle experiments. These curves are measured at once with all twistbucklers attached to the bracket in the same locations between the before and after experiments. Figures (c) and (d) show the comparison of $|\theta|$ for all combinations of twistbucklers without and with shims for decreasing ε .

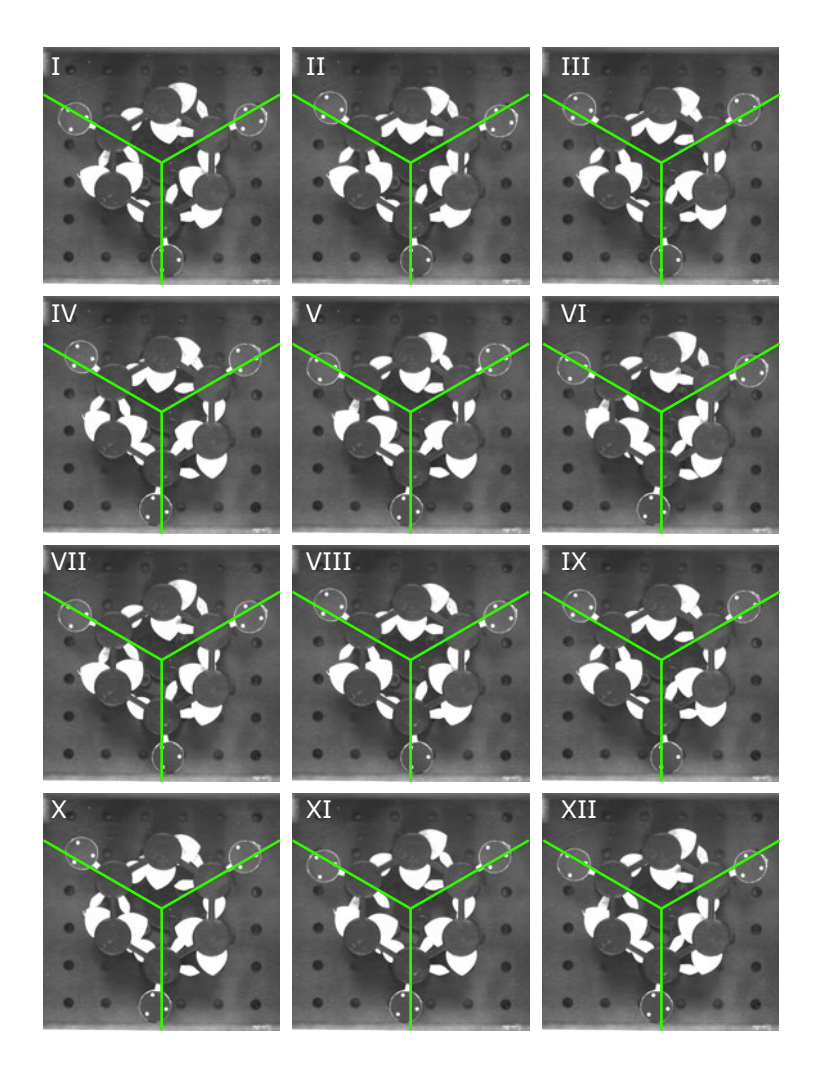


Figure C.7: Isolated frames near $\Delta=1$ of two cycles of the hexcycle machine. The differences between the frames are subtle, so a green reticle indicating the approximate neutral lines is added. Between every frame, a single twistbuckler cell is flipped. Between I and II, the top left cap is flipped, after that the top right, and bottom.

Bibliography

- [1] F. Parrenin, V. Masson-Delmotte, P. Köhler, D. Raynaud, D. Paillard, et al. Synchronous Change of Atmospheric CO₂ and Antarctic Temperature During the Last Deglacial Warming. Science, 339, 1060 (2013). ISSN 0036-8075, 1095-9203. doi:10.1126/science.1226368.
- [2] M. Toiya, J. Stambaugh, and W. Losert. Transient and Oscillatory Granular Shear Flow. Phys. Rev. Lett., 93, 088001 (2004). ISSN 0031-9007, 1079-7114. doi:10.1103/PhysRevLett.93.088001.
- [3] J. Böhm, S. Scherzer, E. Krol, I. Kreuzer, K. von Meyer, et al. The Venus Flytrap Dionaea Muscipula Counts Prey-Induced Action Potentials to Induce Sodium Uptake. Current Biology, 26, 286 (2016). ISSN 09609822. doi: 10.1016/j.cub.2015.11.057.
- [4] N. C. Keim, J. D. Paulsen, Z. Zeravcic, S. Sastry, and S. R. Nagel. *Memory Formation in Matter*. Rev. Mod. Phys., 91, 035002 (2019). ISSN 0034-6861, 1539-0756. doi:10.1103/RevModPhys.91.035002.
- [5] F. Preisach. Über Die Magnetische Nachwirkung. Zeitschrift für physik, 94, 277 (1935).
- [6] J. P. Sethna, K. Dahmen, S. Kartha, J. A. Krumhansl, B. W. Roberts, et al. Hysteresis and Hierarchies: Dynamics of Disorder-Driven First-Order Phase Transformations. Phys. Rev. Lett., 70, 3347 (1993). ISSN 0031-9007. doi: 10.1103/PhysRevLett.70.3347.
- [7] M. Mungan and M. M. Terzi. The Structure of State Transition Graphs in Systems with Return Point Memory: I. General Theory. Ann. Henri Poincaré, 20, 2819 (2019). ISSN 1424-0637, 1424-0661. doi:10.1007/s00023-019-00807-1.
- [8] O. Perković and J. P. Sethna. Improved Magnetic Information Storage Using Return-Point Memory. Journal of Applied Physics, 81, 1590 (1997). ISSN 0021-8979, 1089-7550. doi:10.1063/1.364088.

- [9] D. Shohat, D. Hexner, and Y. Lahini. Memory from Coupled Instabilities in Unfolded Crumpled Sheets. Proc. Natl. Acad. Sci. U.S.A., 119, e2200028119 (2022). ISSN 0027-8424, 1091-6490. doi:10.1073/pnas.2200028119.
- [10] S. N. Coppersmith, T. C. Jones, L. P. Kadanoff, A. Levine, J. P. McCarten, et al. Self-Organized Short-Term Memories. Phys. Rev. Lett., 78, 3983 (1997). ISSN 0031-9007, 1079-7114. doi:10.1103/PhysRevLett.78.3983.
- [11] N. C. Keim and S. R. Nagel. Generic Transient Memory Formation in Disordered Systems with Noise. Phys. Rev. Lett., 107, 010603 (2011). ISSN 0031-9007, 1079-7114. doi:10.1103/PhysRevLett.107.010603.
- [12] J. D. Paulsen and N. C. Keim. Minimal Descriptions of Cyclic Memories. Proc. R. Soc. A., 475, 20180874 (2019). ISSN 1364-5021, 1471-2946. doi: 10.1098/rspa.2018.0874.
- [13] M. Adhikari and S. Sastry. Memory Formation in Cyclically Deformed Amorphous Solids and Sphere Assemblies. Eur. Phys. J. E, 41, 105 (2018). ISSN 1292-8941, 1292-895X. doi:10.1140/epje/i2018-11717-5.
- [14] H. Bense and M. van Hecke. Complex Pathways and Memory in Compressed Corrugated Sheets. Proc. Natl. Acad. Sci. U.S.A., 118, e2111436118 (2021). ISSN 0027-8424, 1091-6490. doi:10.1073/pnas.2111436118.
- [15] D. R. Hofstadter. Gödel, Escher, Bach: An Eternal Golden Braid. Basic Books, New York, 20th anniversary ed edition (1999). ISBN 978-0-394-75682-0 978-0-465-02656-2.
- [16] R. A. Shelby, D. R. Smith, and S. Schultz. Experimental Verification of a Negative Index of Refraction. Science, 292, 77 (2001). ISSN 0036-8075, 1095-9203. doi:10.1126/science.1058847.
- [17] M. Kadic, T. Bückmann, R. Schittny, and M. Wegener. Metamaterials beyond Electromagnetism. Rep. Prog. Phys., 76, 126501 (2013). ISSN 0034-4885, 1361-6633. doi:10.1088/0034-4885/76/12/126501.
- [18] J. Christensen, M. Kadic, M. Wegener, O. Kraft, and M. Wegener. Vibrant Times for Mechanical Metamaterials. MRS Communications, 5, 453 (2015). ISSN 2159-6859, 2159-6867. doi:10.1557/mrc.2015.51.
- [19] R. Lakes. Foam Structures with a Negative Poisson's Ratio. Science, 235, 1038 (1987). ISSN 0036-8075, 1095-9203. doi:10.1126/science.235.4792.1038.
- [20] G. W. Milton. Composite Materials with Poisson's Ratios Close to 1. Journal of the Mechanics and Physics of Solids, 40, 1105 (1992). ISSN 0022-5096. doi:10.1016/0022-5096(92)90063-8.

- [21] G. W. Milton and A. V. Cherkaev. Which Elasticity Tensors Are Realizable? Journal of Engineering Materials and Technology, 117, 483 (1995). ISSN 0094-4289, 1528-8889. doi:10.1115/1.2804743.
- [22] J. Liu, M. Teunisse, G. Korovin, I. R. Vermaire, L. Jin, et al. Controlled Pathways and Sequential Information Processing in Serially Coupled Mechanical Hysterons. Proc. Natl. Acad. Sci. U.S.A., 121, e2308414121 (2024). ISSN 0027-8424, 1091-6490. doi:10.1073/pnas.2308414121.
- [23] A. Rafsanjani and D. Pasini. Bistable Auxetic Mechanical Metamaterials Inspired by Ancient Geometric Motifs. Extreme Mechanics Letters, 9 (2016). ISSN 23524316. doi:10.1016/j.eml.2016.09.001.
- [24] A. Rafsanjani, A. Akbarzadeh, and D. Pasini. Snapping Mechanical Metamaterials under Tension. Advanced Materials, 27, 5931 (2015). ISSN 0935-9648, 1521-4095. doi:10.1002/adma.201502809.
- [25] N. Nadkarni, A. F. Arrieta, C. Chong, D. M. Kochmann, and C. Daraio. Unidirectional Transition Waves in Bistable Lattices. Physical Review Letters, 116, 1 (2016). ISSN 10797114. doi:10.1103/PhysRevLett.116.244501.
- [26] M. Minsky. Computation: Finite and Infinite Machines. Prentice-Hall, Englewood Cliffs, NJ, rev. ed edition (1967). ISBN 978-0-13-165563-8.
- [27] C. El Helou, P. R. Buskohl, C. E. Tabor, and R. L. Harne. Digital Logic Gates in Soft, Conductive Mechanical Metamaterials. Nat Commun, 12, 1633 (2021). ISSN 2041-1723. doi:10.1038/s41467-021-21920-y.
- [28] C. El Helou, B. Grossmann, C. E. Tabor, P. R. Buskohl, and R. L. Harne. Mechanical Integrated Circuit Materials. Nature, 608, 699 (2022). ISSN 0028-0836, 1476-4687. doi:10.1038/s41586-022-05004-5.
- [29] T. Mei, Z. Meng, K. Zhao, and C. Q. Chen. A Mechanical Metamaterial with Reprogrammable Logical Functions. Nat Commun, 12, 7234 (2021). ISSN 2041-1723. doi:10.1038/s41467-021-27608-7.
- [30] C. E. Shannon. A Universal Turing Machine with Two Internal States. In C. E. Shannon and J. McCarthy, editors, Automata Studies. (AM-34), (pages 157–166). Princeton University Press (1956). ISBN 978-1-4008-8261-8. doi: 10.1515/9781400882618-007.
- [31] I. D. Mayergoyz. Hysteresis Models from the Mathematical and Control Theory Points of View. Journal of Applied Physics, 57, 3803 (1985). ISSN 0021-8979, 1089-7550. doi:10.1063/1.334925.

- [32] L. J. Kwakernaak and M. van Hecke. Counting and Sequential Information Processing in Mechanical Metamaterials. Phys. Rev. Lett., 130, 268204 (2023). ISSN 0031-9007, 1079-7114. doi:10.1103/PhysRevLett.130.268204.
- [33] D. J. Amit. Neural Networks Counting Chimes. Proceedings of the National Academy of Sciences of the United States of America, 85, 2141 (1988). ISSN 00278424. doi:10.1073/pnas.85.7.2141.
- [34] M. Mungan, S. Sastry, K. Dahmen, and I. Regev. Networks and Hierarchies: How Amorphous Materials Learn to Remember. Physical review letters, 123, 178002 (2019).
- [35] I. Regev, T. Lookman, and C. Reichhardt. Onset of Irreversibility and Chaos in Amorphous Solids under Periodic Shear. Physical Review E, 88, 062401 (2013).
- [36] C. F. Schreck, R. S. Hoy, M. D. Shattuck, and C. S. O'Hern. Particle-Scale Reversibility in Athermal Particulate Media below Jamming. Physical Review E, 88, 052205 (2013).
- [37] J. R. Royer and P. M. Chaikin. Precisely Cyclic Sand: Self-organization of Periodically Sheared Frictional Grains. Proceedings of the National Academy of Sciences, 112, 49 (2015).
- [38] T. Kawasaki and L. Berthier. Macroscopic Yielding in Jammed Solids Is Accompanied by a Nonequilibrium First-Order Transition in Particle Trajectories. Physical Review E, 94, 022615 (2016).
- [39] M. O. Lavrentovich, A. J. Liu, and S. R. Nagel. Period Proliferation in Periodic States in Cyclically Sheared Jammed Solids. Physical Review E, 96, 020101 (2017).
- [40] K. Nagasawa, K. Miyazaki, and T. Kawasaki. Classification of the Reversible— Irreversible Transitions in Particle Trajectories across the Jamming Transition Point. Soft matter, 15, 7557 (2019).
- [41] W.-T. Yeh, M. Ozawa, K. Miyazaki, T. Kawasaki, and L. Berthier. Glass Stability Changes the Nature of Yielding under Oscillatory Shear. Physical review letters, 124, 225502 (2020).
- [42] N. C. Keim and J. D. Paulsen. Multiperiodic Orbits from Interacting Soft Spots in Cyclically Sheared Amorphous Solids. Sci. Adv., 7, eabg7685 (2021). ISSN 2375-2548. doi:10.1126/sciadv.abg7685.
- [43] C. W. Lindeman and S. R. Nagel. Multiple Memory Formation in Glassy Landscapes. Sci. Adv., 7, eabg7133 (2021). ISSN 2375-2548. doi:10.1126/ sciadv.abg7133.

- [44] K. Bertoldi, V. Vitelli, J. Christensen, and M. Van Hecke. Flexible Mechanical Metamaterials. Nat Rev Mater, 2 (2017). ISSN 2058-8437. doi:10.1038/ natrevmats.2017.66.
- [45] T. Chen, M. Pauly, and P. M. Reis. A Reprogrammable Mechanical Metamaterial with Stable Memory. Nature, 589, 386 (2021). ISSN 0028-0836, 1476-4687. doi:10.1038/s41586-020-03123-5.
- [46] S. Wolfram. Cellular Automata and Complexity: Collected Papers. crc Press (2018).
- [47] C. Kaspar, B. J. Ravoo, W. G. van der Wiel, S. V. Wegner, and W. H. Pernice. The Rise of Intelligent Matter. Nature, 594, 345 (2021).
- [48] H. Yasuda, P. R. Buskohl, A. Gillman, T. D. Murphey, S. Stepney, et al. Mechanical Computing. Nature, 598, 39 (2021). ISSN 0028-0836, 1476-4687. doi:10.1038/s41586-021-03623-y.
- [49] J. T. B. Overvelde, T. Kloek, J. J. A. D'haen, and K. Bertoldi. Amplifying the Response of Soft Actuators by Harnessing Snap-through Instabilities. Proc. Natl. Acad. Sci. U.S.A., 112, 10863 (2015). ISSN 0027-8424, 1091-6490. doi:10.1073/pnas.1504947112.
- [50] C. Coulais, A. Sabbadini, F. Vink, and M. Van Hecke. Multi-Step Self-Guided Pathways for Shape-Changing Metamaterials. Nature, 561, 512 (2018). ISSN 0028-0836, 1476-4687. doi:10.1038/s41586-018-0541-0.
- [51] M. Stern, V. Jayaram, and A. Murugan. Shaping the Topology of Folding Pathways in Mechanical Systems. Nature communications, 9, 4303 (2018).
- [52] T. Jules, A. Reid, K. E. Daniels, M. Mungan, and F. Lechenault. Delicate Memory Structure of Origami Switches. Phys. Rev. Research, 4, 013128 (2022). ISSN 2643-1564. doi:10.1103/PhysRevResearch.4.013128.
- [53] D. Melancon, A. E. Forte, L. M. Kamp, B. Gorissen, and K. Bertoldi. Inflatable Origami: Multimodal Deformation via Multistability. Adv Funct Materials, 32, 2201891 (2022). ISSN 1616-301X, 1616-3028. doi:10.1002/adfm.202201891.
- [54] J. D. Paulsen, N. C. Keim, and S. R. Nagel. Multiple Transient Memories in Experiments on Sheared Non-Brownian Suspensions. Physical Review Letters, 113, 068301 (2014).
- [55] M. Gardner. Mathematical Games: The Fantastic Combinations of John Conway's New Solitaire Game'life'Scientific American (1970).
- [56] L. J. Kwakernaak, A. Guerra, D. P. Holmes, and M. Van Hecke. The Collective Snapping of a Pair of Bumping Buckled Beams. Extreme Mechanics Letters, 69, 102160 (2024). ISSN 23524316. doi:10.1016/j.eml.2024.102160.

- [57] L. A. Lubbers, M. van Hecke, and C. Coulais. A Nonlinear Beam Model to Describe the Postbuckling of Wide Neo-Hookean Beams. Journal of the Mechanics and Physics of Solids, 106, 191 (2017). ISSN 00225096. doi: 10.1016/j.jmps.2017.06.001.
- [58] H. Yang and L. Ma. Multi-Stable Mechanical Metamaterials by Elastic Buckling Instability. J Mater Sci, 54, 3509 (2019). ISSN 0022-2461, 1573-4803. doi: 10.1007/s10853-018-3065-y.
- [59] D. Yang, L. Jin, R. V. Martinez, K. Bertoldi, G. M. Whitesides, et al. *Phase-Transforming and Switchable Metamaterials*. Extreme Mechanics Letters, 6, 1 (2016). ISSN 23524316. doi:10.1016/j.eml.2015.11.004.
- [60] C. Coulais, A. Sabbadini, F. Vink, and M. van Hecke. Multi-Step Self-Guided Pathways for Shape-Changing Metamaterials. Nature, 561, 512 (2018). ISSN 0028-0836, 1476-4687. doi:10.1038/s41586-018-0541-0.
- [61] J. Ding and M. Van Hecke. Sequential Snapping and Pathways in a Mechanical Metamaterial. The Journal of Chemical Physics, 156, 204902 (2022). ISSN 0021-9606, 1089-7690. doi:10.1063/5.0087863.
- [62] R. Khajehtourian and D. M. Kochmann. Phase Transformations in Substrate-Free Dissipative Multistable Metamaterials. Extreme Mechanics Letters, 37, 100700 (2020). ISSN 23524316. doi:10.1016/j.eml.2020.100700.
- [63] P. Holmes, G. Domokos, and G. Hek. Euler Buckling in a Potential Field. J. Nonlinear Sci., 10, 477 (2000). ISSN 0938-8974, 1432-1467. doi:10.1007/s003320010002.
- [64] P. Holmes, G. Domokos, J. Schmitt, and I. Szeberényi. Constrained Euler Buckling: An Interplay of Computation and Analysis. Computer Methods in Applied Mechanics and Engineering, 170, 175 (1999). ISSN 00457825. doi:10.1016/S0045-7825(98)00194-7.
- [65] J.-S. Chen and S.-Y. Hung. Deformation and Stability of an Elastica Constrained by Curved Surfaces. International Journal of Mechanical Sciences, 82, 1 (2014). ISSN 00207403. doi:10.1016/j.ijmecsci.2014.03.001.
- [66] S. Katz and S. Givli. The Postbuckling Behavior of Planar Elastica Constrained by a Deformable Wall. Journal of Applied Mechanics, 84, 051001 (2017). ISSN 0021-8936, 1528-9036. doi:10.1115/1.4036018.
- [67] R. S. Manning and G. B. Bulman. Stability of an Elastic Rod Buckling into a Soft Wall. Proc. R. Soc. A., 461, 2423 (2005). ISSN 1364-5021, 1471-2946. doi:10.1098/rspa.2005.1458.

- [68] J.-S. Chen and L.-C. Wang. Contact between Two Planar Buckled Beams Pushed Together Transversely. International Journal of Solids and Structures, 199, 181 (2020). ISSN 00207683. doi:10.1016/j.ijsolstr.2020.04.029.
- [69] J.-S. Chen and Z.-H. Yang. On the Asymmetric Line-Contact Deformation between Two Planar Elasticae. International Journal of Solids and Structures, 256, 111991 (2022). ISSN 00207683. doi:10.1016/j.ijsolstr.2022.111991.
- [70] Z. P. Bažant and L. Cedolin. Stability of Structures: Elastic, Inelastic, Fracture and Damage Theories. WORLD SCIENTIFIC (2010). ISBN 978-981-4317-02-3 978-981-4317-04-7. doi:10.1142/7828.
- [71] A. Magnusson, M. Ristinmaa, and C. Ljung. Behaviour of the Extensible Elastica Solution. International Journal of Solids and Structures, 38, 8441 (2001). ISSN 00207683. doi:10.1016/S0020-7683(01)00089-0.
- [72] A. Pandey, D. E. Moulton, D. Vella, and D. P. Holmes. *Dynamics of Snapping Beams and Jumping Poppers*. **Europhysics Letters**, **105**, 24001 (2014).
- [73] A. Guerra, A. Slim, D. P. Holmes, and O. Kodio. Self-Ordering of Buckling, Bending, Bumping Beams. Phys. Rev. Lett., 130, 148201 (2023). ISSN 0031-9007, 1079-7114. doi:10.1103/PhysRevLett.130.148201.
- [74] P. X. Bellini. The Concept of Snap-Buckling Illustrated by a Simple Model. International Journal of Non-Linear Mechanics, 7, 643 (1972). ISSN 00207462. doi:10.1016/0020-7462(72)90004-2.
- [75] A. Guerra and D. P. Holmes. Emergence of Structure in Columns of Grains and Elastic Loops. Soft Matter, 17, 7662 (2021). ISSN 1744-683X, 1744-6848. doi:10.1039/D1SM00787D.
- [76] A. P. Thompson, H. M. Aktulga, R. Berger, D. S. Bolintineanu, W. M. Brown, et al. LAMMPS a Flexible Simulation Tool for Particle-Based Materials Modeling at the Atomic, Meso, and Continuum Scales. Computer Physics Communications, 271, 108171 (2022). ISSN 00104655. doi: 10.1016/j.cpc.2021.108171.
- [77] R. Sachse, A. Westermeier, M. Mylo, J. Nadasdi, M. Bischoff, et al. Snapping Mechanics of the Venus Flytrap (Dionaea Muscipula). Proc. Natl. Acad. Sci. U.S.A., 117, 16035 (2020). ISSN 0027-8424, 1091-6490. doi:10.1073/pnas.2002707117.
- [78] D. P. Holmes and A. J. Crosby. Snapping Surfaces. Adv. Mater., 19, 3589 (2007). ISSN 09359648, 15214095. doi:10.1002/adma.200700584.

- [79] H. C. Bennet-Clark. The Energetics of the Jump of the Locust Schistocerca Gregaria. Journal of Experimental Biology, 63, 53 (1975). ISSN 0022-0949, 1477-9145. doi:10.1242/jeb.63.1.53.
- [80] E. Queathem. The Ontogeny of Grasshopper Jumping Performance. Journal of Insect Physiology, 37, 129 (1991). ISSN 00221910. doi:10.1016/0022-1910(91)90098-K.
- [81] L. Jin, Y. Yang, B. O. T. Maldonado, S. D. Lee, N. Figueroa, et al. Ultrafast, Programmable, and Electronics-Free Soft Robots Enabled by Snapping Metacaps. Advanced Intelligent Systems, 5, 2300039 (2023). ISSN 2640-4567, 2640-4567. doi:10.1002/aisy.202300039.
- [82] A. Rafsanjani and K. Bertoldi. Buckling-Induced Kirigami. Phys. Rev. Lett., 118, 084301 (2017). ISSN 0031-9007, 1079-7114. doi:10.1103/PhysRevLett.118.084301.
- [83] S. Shan, S. H. Kang, J. R. Raney, P. Wang, L. Fang, et al. Multistable Architected Materials for Trapping Elastic Strain Energy. Adv. Mater., 27, 4296 (2015). ISSN 09359648. doi:10.1002/adma.201501708.
- [84] J. Zehnder, E. Knoop, M. Bächer, and B. Thomaszewski. Metasilicone: Design and Fabrication of Composite Silicone with Desired Mechanical Properties. ACM Trans. Graph., 36, 1 (2017). ISSN 0730-0301, 1557-7368. doi: 10.1145/3130800.3130881.
- [85] G. Bradski. The OpenCV Library. Dr. Dobb's Journal of Software Tools (2000).
- [86] M. Smith. ABAQUS/Standard User's Manual, Version 6.9. Dassault Systèmes Simulia Corp, United States (2009).
- [87] J. D. Paulsen and N. C. Keim. Mechanical Memories in Solids, from Disorder to Design. http://arxiv.org/abs/2405.08158 (2024).
- [88] S. Wolfram. Statistical Mechanics of Cellular Automata. Rev. Mod. Phys., 55, 601 (1983). ISSN 0034-6861. doi:10.1103/RevModPhys.55.601.
- [89] D. Melancon, B. Gorissen, C. J. García-Mora, C. Hoberman, and K. Bertoldi. Multistable Inflatable Origami Structures at the Metre Scale. Nature, 592, 545 (2021). ISSN 0028-0836, 1476-4687. doi:10.1038/s41586-021-03407-4.
- [90] J. W. Hutchinson and W. T. Koiter. Postbuckling Theory. Appl. Mech. Rev, 23, 1353 (1970).

- [91] J. Tian, C. Wang, and S. Swaddiwudhipong. Elastic Buckling Analysis of Ring-Stiffened Cylindrical Shells under General Pressure Loading via the Ritz Method. Thin-Walled Structures, 35, 1 (1999). ISSN 02638231. doi:10.1016/S0263-8231(99)00012-9.
- [92] D. A. Dow. Buckling and Postbuckling Tests of Ring-Stiffened Circular Cylinders Loaded by Uniform External Pressure. Technical Report No. NASA-TN-D-3111, NASA (1965).
- [93] N. Rathinam, B. Prabu, and N. Anbazhaghan. Buckling Analysis of Ring Stiffened Thin Cylindrical Shell under External Pressure. Journal of Ocean Engineering and Science, 6, 360 (2021). ISSN 24680133. doi:10.1016/ j.joes.2021.03.002.
- [94] T. Von Karman and H.-S. Tsien. The Buckling of Thin Cylindrical Shells Under Axial Compression. Journal of the Aeronautical Sciences, 8, 303 (1941). ISSN 1936-9956. doi:10.2514/8.10722.
- [95] Y. Yoshimura. On the Mechanism of Buckling of a Circular Cylindrical Shell under Axial Compression. Technical Report No. NACA-TM-139, NASA (1955).
- [96] E. Lancaster, C. Calladine, and S. Palmer. Paradoxical Buckling Behaviour of a Thin Cylindrical Shell under Axial Compression. International Journal of Mechanical Sciences, 42, 843 (2000). ISSN 00207403. doi:10.1016/S0020-7403(99)00030-2.
- [97] A. Reid, F. Lechenault, S. Rica, and M. Adda-Bedia. Geometry and Design of Origami Bellows with Tunable Response. Phys. Rev. E, 95, 013002 (2017). ISSN 2470-0045, 2470-0053. doi:10.1103/PhysRevE.95.013002.
- [98] M. Aigner and G. M. Ziegler. Proofs from The Book. Springer, Berlin; New York, 2nd corr. print edition (1999). ISBN 978-3-540-63698-4.
- [99] L. Euler. Remarques Sur l'effet Du Frottement Dans l'equilibre. Memoires de l'academie des sciences de Berlin, (pages 265–278) (1769).
- [100] J. A. Eytelwein. Handbuch Der Statik Fester Körper: Mit Vorzüglicher Rücksicht Auf Ihre Anwendung in Der Architektur, volume 1. Reimer (1832).
- [101] J. Mercier. Dispositif De Transmission De Mouvement Par Un Engrenage Exterieur. Patent, France, 2609768 (1988).
- [102] D. Valentin and J. Mercier. Differential Device. Patent, United States of America, 4831890 (1989).
- [103] H. M. Cundy and A. P. Rollett. *Mathematical Models*. Tarquin Publications, St. Albans, 3. ed., repr edition (2007). ISBN 978-0-906212-20-2.

BIBLIOGRAPHY

- [104] R. C. Juvinall and K. M. Marshek. Fundamentals of Machine Component Design. John Wiley & Sons, Hoboken, NJ, 4th ed edition (2006). ISBN 978-0-471-66177-1.
- [105] N. Sclater. Mechanisms and Mechanical Devices Sourcebook. McGraw-Hill, New York, NY, 5. ed edition (2011). ISBN 978-0-07-170442-7 978-1-265-63178-9.
- [106] M. Cook. Universality in Elementary Cellular Automata. Complex Systems (2004).
- [107] A. S. Meeussen, E. C. Oğuz, Y. Shokef, and M. V. Hecke. Topological Defects Produce Exotic Mechanics in Complex Metamaterials. Nat. Phys., 16, 307 (2020). ISSN 1745-2473, 1745-2481. doi:10.1038/s41567-019-0763-6.
- [108] R. C. Merkle, R. A. Freitas Jr., T. Hogg, T. E. Moore, M. S. Moses, et al. Mechanical Computing Systems Using Only Links and Rotary Joints. Journal of Mechanisms and Robotics, 10, 061006 (2018). ISSN 1942-4302, 1942-4310. doi:10.1115/1.4041209.
- [109] V. J. Katz. A History of Mathematics: An Introduction. Addison-Wesley Longman, Reading, Mass. Harlow, 2. ed., repr. with corr edition (1998). ISBN 978-0-321-01618-8.
- [110] J.-Y. Tinevez, N. Perry, J. Schindelin, G. M. Hoopes, G. D. Reynolds, et al. TrackMate: An Open and Extensible Platform for Single-Particle Tracking. Methods, 115, 80 (2017). ISSN 10462023. doi:10.1016/j.ymeth.2016.09.016.
- [111] S. Van Der Walt, J. L. Schönberger, J. Nunez-Iglesias, F. Boulogne, J. D. Warner, et al. *Scikit-Image: Image Processing in Python.* **PeerJ**, **2**, e453 (2014). ISSN 2167-8359. doi:10.7717/peerj.453.
- [112] Robert Ferréol. *Involute of a Circle*. https://mathcurve.com/courbes2d.gb/developpantedecercle/developpantedecercle.shtml.

Summary

This dissertation covers the research I performed at the University of Leiden and the AMOLF research institute in Amsterdam. I investigated mechanical metamaterials; a relatively new field of science that studies material properties which go beyond the properties of ordinary materials.

In this dissertation, I ventured into one of the newest areas of metamaterials: *memory*. My research was initially started with the question: "can we make a block of rubber that can count?", which I set out to discover. Very quickly, I realized that counting not only requires a retention of information, but a simple form of computation as well. Thus, after developing an initial 'counting material,' I investigated the essential components required for such a material, its potential capabilities, and the limitations of various configurations of these minimal components. Would these ingredients allow us to learn more about memory, possibly even allow us to perform computations?

Chapter one serves as the introduction of this dissertation and it discusses the wide variety of memory observed in materials and devices. I start by discussing footprints in the sand and mechanical lap counters, two vastly different systems yet both featuring a form of memory. We narrow down our definition of memory, introduce mechanical metamaterials, and discuss the concept of materials as computers.

Chapter two discusses the beam counter metamaterial; a block of rubber with a specific structure such that allows it to count how often it is compressed.

The beam counter metamaterial consists of an array of parallel beams of two different thicknesses, separated by gaps of alternating size. Additionally, the thicker beams feature a slit such that they can 'fold open' in one direction. All beams have a small geometric asymmetry such that their buckling direction is predetermined. Similarly, all other features of the beam counter are chosen such that through a contact interaction, successive compression cycles are effectively recorded in the bistable state of the thinner beams. Effectively the block of rubber is able to count how often it is

compressed. In a practical sense, one could include such a block of rubber in a structure to register and log wear and tear. Under a bridge, for example, such a material could track how many overweight trucks drove across it without external sensors or power sources.

Finalizing the chapter, we demonstrate beam counters that are able to distinguish different compression intensities. Combining these, and by using counters that feature a sequence of different thresholds, we realize a metamaterial that detects a specific input sequence, similar to a lock: this metamaterial only reaches a well defined accepting (open) state given a specific sequence of thresholds (key).

Chapter three discusses the interaction that occurs between buckled beams in contact, which is fundamental for the working of the beam counter metamaterial. As two beams of equal length and unequal thickness are compressed, buckle and bump in to each other, they collectively snap in either the direction of the thinner or the thicker beam. We find that the direction is decided solely by the distance between these two beams. We find that for every pair of unequal beams there is a certain critical spacing: when the beams are closer together than this critical distance, the beams snap in the direction of the thicker beam, and when the beams are further apart, the beams snap in the direction of the thinner beam. This interaction is the crucial ingredient for the working of the beam counter metamaterial.

Using both experiments and simulations, we study the phenomenon and found a surprising linear relation between the observed critical distance and the combined thickness of the two beams. Finally we introduce a minimal model based on the truss structure introduced by Bellini et al., and the beam models of Guerra et al., which explains this linear scaling. With this simple model, we further learn that the direction of snapping is determined before contact is lost, and can be understood as the result of a pitchfork bifurcation.

Chapter four discusses the slitted beams used in the beam counter metamaterial. These beams feature a partial slit cut into the beam, forming a hinge that opens only towards one side. These elements play a crucial role in the function of the beam counter metamaterial, as these beams behave equivalent to an uncut beam at small compression, and a strongly asymmetric beam at large compression when the hinge opens up. In the beam counter these are beneficial as they extend further towards one side. This chapter however is concerned more with the hysteretic response that these beams have when compressed; as a slitted beam is compressed and it snaps open, it will remain open when decompressed below the compression where it initially opened. These slitted beams therefore have a memory of the past.

The chapter specifically delves into the observed phenomenology as a function of the

beam's geometry, and uncovers the mechanisms behind the hysteretic transitions of the opening and closing of the slit. Using both experiments and simulations, we find that the opening and closing strains can be individually tuned, and we find a fitting parameterization of the Bellini Truss which matches the observations.

Chapter five discusses twistbuckler metamaterials, which build on the beam counter metamaterial by extending to two dimensions and allowing for interactions to occur between two bistable elements in all four stable states. These metamaterials feature base elements that twist as they buckle and interact through rigid contact with precisely shaped interfaces.

The twistbucklers enable the creation of cyclical counters. While all beam counters eventually 'run out' due to their configuration in a line, the twisting motion of the twistbucklers allows for more diverse types of coupling and specifically the ability to connect the ends of the line and place elements in a loop such that after a number of cycles they return to their initial state.

In this chapter, we first discuss the individual twistbucklers and measure their torsional response. Next, we discuss the contact interaction and the design of the contact interfaces. These interfaces, which are based on the shape of gear teeth block parts of configuration space, and allow the rotation rates of twistbuckler to be coupled when in contact. We demonstrate how the blocked configuration space can be used to design when twistbucklers interact, and how the coupling can be used to determine which twistbuckler is forced to switch states in each interaction.

Finally, we demonstrate a counter consisting of two twistbucklers that cyclically goes through two states, and a counter consisting of six twistbucklers that goes through six states and could be scaled up to arbitrarily long length cycles.

Samenvatting

Deze dissertatie behandelt het onderzoek dat ik uitgevoerd heb bij de universiteit van Leiden en het onderzoeksinstituut AMOLF in Amsterdam. Ik heb onderzoek gedaan naar mechanische metamaterialen; een nieuw veld in de wetenschap waarin materiaaleigenschappen onderzocht worden die verder rijken dan dan eigenschappen van normale materialen.

In deze dissertatie behandel ik een nieuwe eigenschap binnen de studie van de metamaterialen: geheugen. Mijn onderzoek was oorspronkelijk begonnen met de vraag: "kan een blok rubber gemaakt worden dat kan tellen?". In een mum van tijd werd het mij duidelijk dat een blok tellend rubber niet alleen een vorm van geheugen nodig heeft, maar ook een vorm van berekening moet uitvoeren. Nadat ik het eerste tellende materiaal gemaakt had, onderzoch ik wat in algemene zin de benodigde ingredient voor zo'n materiaal zouden zijn en wat er nog meer gemaakt zou kunnen worden met deze ingrediënten. Zouden deze ingrediënten ons helpen verder te kunnen onderzoeken hoe geheugen ontstaat in materialen, en mogelijk zelfs berekening te kunnen laten doen?

Hoofdstuk één dient ter introductie van deze dissertatie en introduceert een aantal vormen van geheugen die gevonden worden in materialen en apparaten. Het hoofdstuk begint met een discussie over voetafdrukken in het zand en mechanische tellers, twee compleet verschillende systemen maar beide met een vorm van geheugen. Vervolgens maken we onze definitie van geheugen preciezer, introduceren we mechanische metamaterialen, en bespreken het concept van een materiaal als een computer.

Hoofdstuk twee behandelt het "balken-teller" metamateriaal; een blok rubber met een specifieke structuur zodat het kan tellen hoe vaak het ingedrukt is.

Het balken-teller metamateriaal bestaat uit een reeks parallelle balken van twee ver-

 $^{^1}Beam\ counter$ in het Engels. Een woordspeling gebaseerd op de term bean\ counter; een pejoratieve term voor een accountant.

schillende diktes, om en om met kleinere en grotere openingen ertussen. Bovendien bevatten de dikkere balken een spleet zodat ze in één richting kunnen 'openvouwen'. Alle balken hebben een kleine geometrische asymmetrie, zodat hun knikrichting vooraf is bepaald. Evenzo zijn alle andere kenmerken van de balken-teller zodanig gekozen dat door een contactinteractie opeenvolgende compressiecycli worden vastgelegd in de bistabiele toestand van de dunnere balken. Effectief kan het blok rubber tellen hoe vaak het wordt samengedrukt. Zo'n blok rubber zou in de praktijk verwerkt kunnen worden in een bouwstuk om slijtage bij te kunnen houden. Een balken-teller zou bijvoorbeeld onder een brug geplaatst kunnen worden om bij te houden hoe vaak deze overbelast wordt.

Ten slotte demonstreren we balken-tellers die verschillende belastingen kunnen herkennen. Door meerdere van deze tellers samen te gebruiken en tellers te gebruiken die voor een specifieke volgorde van kleine en grote belastingen gevoelig zijn, demonstreren we vervolgens een metamateriaal dat een specifieke volgorde van invoer herkent, net zoals een slot en sleutel. Het metamateriaal bereikt alleen een specifieke 'accepterende' (open) toestand als een specifieke sequentie van belastingen ingevoerd wordt (sleutel).

Hoofdstuk drie behandelt de interactie die voorkomt tussen geknikte balken welke ten grondslag ligt voor de werking van het balken-teller metamateriaal. Naarmate twee balken van gelijke lengte maar ongelijke dikte knikken en tegen elkaar tikken, klakken ze tezamen in de richting van de dunnere of dikkere balk. Die richting blijkt enkel bepaald te worden door de afstand tussen de balken. We vinden dat voor elk paar ongelijke balken er een kritieke afstand is: als de balken dichter bij elkaar staan dan deze kritieke afstand, dan klakken de balken in de richting van de dikke balk, als de balken verder weg staan dan dit criterium, dan klakken ze in de richting van de dunne balk. Deze interactie is het cruciale ingredient voor de werking van het balken-teller metamateriaal.

Gebruikmakend van zowel experimenten als simulaties bestuderen we het fenomeen en vinden we een verrassende lineaire relatie tussen de geobserveerde kritieke afstand en de som van de diktes van de balken. Ten slotte introduceren we een minimaal model gebaseerd op de "vakwerk" (truss) structuur geïntroduceerd door Bellini et al., en de balk-modellen van Guerra et al., welke deze relatie verklaard. Met dit simpele model ontdekken we verder dat de richting van klakken bepaald wordt voordat de balken los komen van elkaar en bepaald wordt door een hooivork-bifurcatie.

Hoofdstuk vier behandelt de half-gesneden balken welke in het balken-teller metamateriaal gebruikt worden. Deze balken bevatten een snede halverwege het midden van de balk zodat deze een scharnier vormt. Deze elementen spelen een cruciale rol in de werking van het balken-teller metamateriaal doordat deze balken zich in de dichte toestand nagenoeg identiek gedragen aan een niet-ingesneden balk, maar naar één kant drastisch verder uitbuigen wanneer deze ver ingedrukt wordt. In de teller worden deze balken gebruikt omdat ze naar één kant verder uitwijken, maar in dit hoofdstuk wordt een andere eigenschap van deze balken onderzocht; als de balken ingedrukt en losgelaten worden blijft het openen en dichtgaan van het scharnier achter (hysterese). Deze balken bevatten daarom een vorm van geheugen.

Dit behandelt de geobserveerde fenomenologie als functie van de geometrie van de balken, en onthult het onderliggende mechanisme van de achterblijvende transitie. Door het uitvoeren van zowel experimenten als simulaties vinden we dat de indrukking waarbij het scharnier opent en sluit onafhankelijk gekozen kan worden, en vinden we een mathematisch model gebaseerd op het vakwerk van Bellini welke overeen komt met onze observaties.

Hoofdstuk vijf behandelt de "draai-knikker" (*twistbuckler*) metamaterialen welke voortborduren op het balken-teller metamateriaal door deze uit te breiden naar twee dimensies en interacties tussen alle vier toestanden van twee bistabiele elementen mogelijk te maken. Deze metamaterialen bevatten basis-elementen welke draaien als ze knikken en welke interacteren door middel van hard contact met precies gevormde contactvlakken.

De draai-knikkers maken het mogelijke cyclische tellers te maken. Hoewel normale balken-teller metamaterialen uiteindelijk een 'eindtoestand' bereiken, maakt de draai-ende beweging van de draai-knikker het mogelijk om deze in een lus te zetten en de interactie zo te kiezen dat de toestand herhaaldelijk terug komt bij de begintoestand.

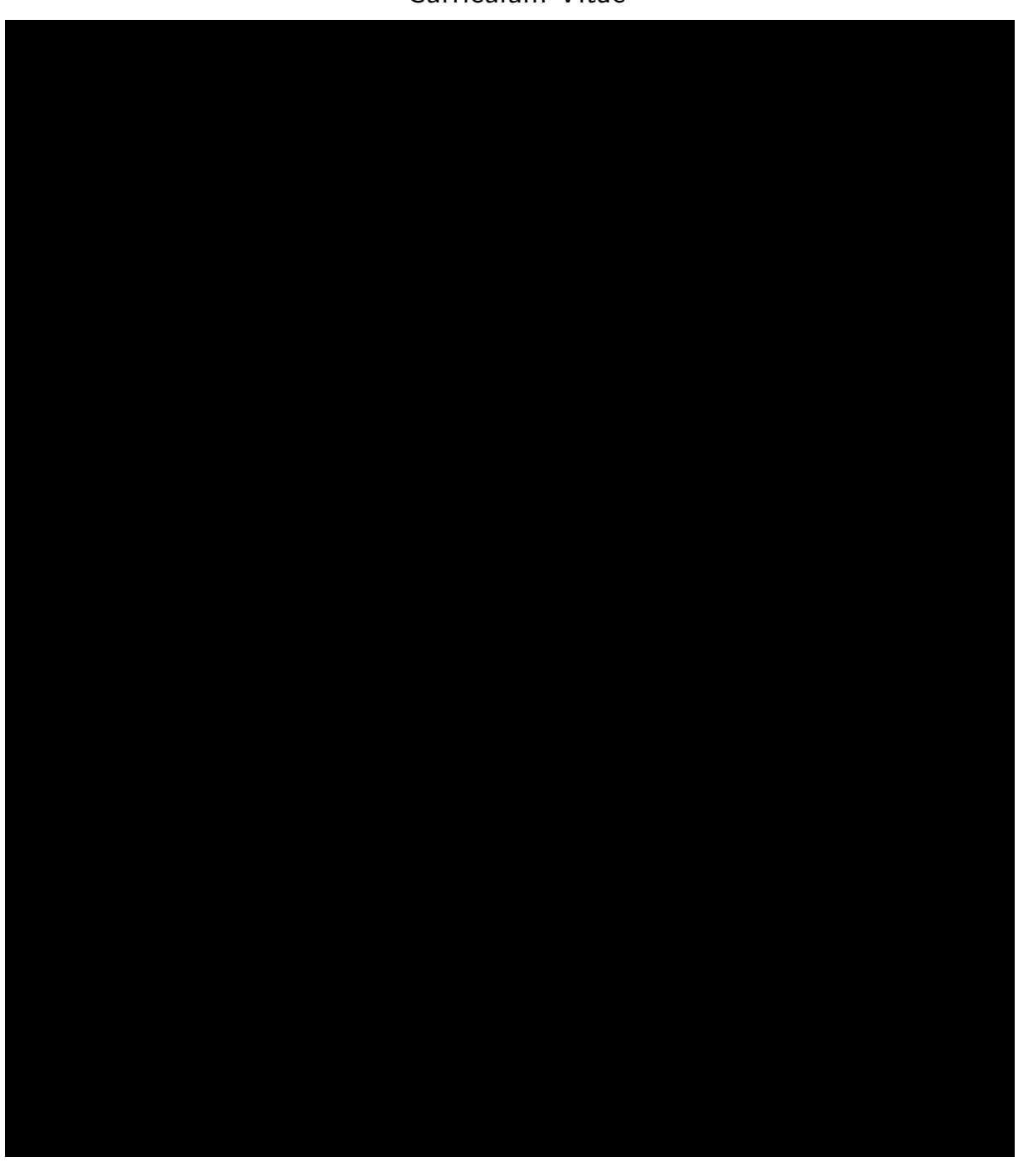
In dit hoofdstuk behandelen we eerst het gedrag van individuele draai-knikkers en meten we het moment welke deze uitoefenen onder verschillende indrukkingen en draaihoeken. Vervolgens behandelen we de interactie door middel van contact en het ontwerp van de contactvlakken. Het ontwerp van de contactvlakken is gebaseerd op de vorm van tandwieltanden, en net as bij tandwielen, blokkeren deze tanden combinaties van hoeken en zorgen deze voor een koppeling tussen de draaisnelheden van de draai-knikkers. We demonstreren hoe een geblokkeerde configuratieruimte gebruikt kan worden om te bepalen wanneer de draai-knikkers interacteren, en hoe de koppeling gebruikt kan worden om te bepalen welke draai-knikker van toestand wisselt in elke interactie.

Ten slotte behandelen we een teller bestaande uit twee draai-knikkers die cyclisch tussen twee toestanden wisselt, en een teller bestaande uit zes draai-knikkers die door zes toestanden wisselt en uitgebreid kan worden om tot willekeurig grote hoeveelheden te tellen.

Publications

- Kwakernaak, Lennard J., and Martin van Hecke. Counting and Sequential Information Processing in Mechanical Metamaterials. Phys. Rev. Lett. 130, no. 26 (2023). ISSN 0031-9007, 1079-7114. doi:10.1103/PhysRevLett.130.268204.
- Kwakernaak, Lennard J., Arman Guerra, Douglas P. Holmes, and Martin van Hecke. *The Collective Snapping of a Pair of Bumping Buckled Beams*. **Extreme Mechanics Letters 69** (2024). ISSN 23524316. doi:10.1016/j.eml.2024.102160.

Curriculum Vitae



Acknowledgements

I would like to express my gratitude to Leiden University and the AMOLF research institute for facilitating the research presented in this dissertation.

Special thanks go to Jeroen Mesman of the fine-mechanics department for assisting me in constructing my experimental setups in Leiden, and Dion Ursum for his assistance in experiments in Amsterdam. Their expertise was instrumental, and without it, this dissertation would not have been possible.

My sincere appreciation goes to my supervisor Martin van Hecke for his expertise and mentorship. Your critical thinking has helped shape my ideas, and your skillful writing has helped me communicate these effectively to the world.

I am fortunate to have worked alongside many incredible colleagues. I want to especially mention my fellow group members during my journey: Anne Meeussen, Amitesh Singh, Bernat Durà Faulí, Colin Meulblok, Hadrien Bense, Jerry Jingran, Lishuai Jin, Margot Teunisse, Paul Baconnier, Ryan van Mastrigt, and Yiangnan Ding, for providing a welcoming environment and sharing their intellect. To all my colleagues from the tenth floor, your company will be greatly missed.

I am also especially grateful to Douglas Holmes and Arman Guerra of Boston University for assisting me in the development of theoretical models and teaching me to perform crucial calculations.

I am grateful to my parents Marin and Mirjam and my brother Brennan for their unwavering support. Your belief in me has been the foundation upon which I have built my academic career.

To my love, Merit, thank you for your kindness, enthusiasm, interest, and patience. Your support has never ceased to motivate me and bring me joy.

Acknowledgements

Lastly, I want to express gratitude to everyone who, either voluntarily or involuntarily, listened to my ramblings about counting rubber, gave me new perspectives through interesting questions, or otherwise challenged my understanding of my own work. Your contributions have made my scientific journey ever more enjoyable.